The Dissertation Committee for Charles Dallas Amos Certifies that this is the approved version of the following dissertation:

Effect of Chemical Treatment and Trivalent Doping on the Surface Structure and Surface Chemistry of $Li_{1-x}Ni_{0.5-y}Mn_{1.5+y}O_4$ Spinel

Committee:

John B. Goodenough, Supervisor

Paulo J. Ferreira, Co-Supervisor

Charles B. Mullins

Guihua Yu

Maria Varela

Effect of Chemical Treatment and Trivalent Doping on the Surface Structure and Surface Chemistry of $Li_{1-x}Ni_{0.5-y}Mn_{1.5+y}O_4$ Spinel

by

Charles Dallas Amos

Dissertation

Presented to the Faculty of the Graduate School of

The University of Texas at Austin

in Partial Fulfillment

of the Requirements

for the Degree of

Doctor of Philosophy

The University of Texas at Austin

December 2017

Dedication

“We are the music-makers, and we are the dreamers of dreams” –Arthur O’Shaughnessy

Acknowledgements

I would first like to thank my family for their love and support. I want to thank all of my teachers whose collective effort has placed me into a position to succeed. I want to thank my labmates and Dr. Federico Cardenas for their wonderful discussion. I would like to thank Nick for working with me through the late nights. I would like to thank Jie Song for teaching me how to make my first battery. I would like to thank Manuel for being a great friend and mentor. I would like to thank my committee, which includes Dr. John B. Goodenough, Dr. Paulo J. Ferreira, Dr. Charles B. Mullins, Dr. Guihua Yu, and Dr. Maria Varela for all their helpful guidance and discussion. I would also like to thank NASA for awarding me the NASA Space Technology Research Fellowship (NSTRF). This work was supported by a NASA Office of the Chief Technologist's Space Technology Research Fellowship (NNX12AN25H).

Effect of Chemical Treatment and Trivalent Doping on the Surface Structure and Surface Chemistry of $Li_{1-x}Ni_{0.5-y}Mn_{1.5+y}O_4$ Spinel

Charles Dallas Amos, Ph.D.

The University of Texas at Austin, 2017

Supervisor: John B. Goodenough

Co-Supervisor: Paulo J. Ferreira

The surface structure and surface chemistry of $Li_{1-x}Ni_{0.5-y}Mn_{1.5+y}O_4$ was examined by first analyzing as-prepared $Li[Mn_2]O_4$, the basis cubic spinel structure without Ni or trivalent dopants. It was found that $Li[Mn_2]O_4$ undergoes a surface reconstruction, which results in the production of a thin, stable surface layer of Mn_3O_4, a subsurface region of $Li_{1+x}[Mn_2]O_4$ with retention of bulk $Li[Mn_2]O_4$. This observation is compatible with the surface disproportionation of Mn coupled with oxygen deficiency and a displacement of surface Li^+ from the Mn_3O_4 surface phase to a subsurface layer. $Li[Mn_2]O_4$ was then subjected to chemical treatments to further understand and isolate the role of Li and oxygen in the surface reconstruction. An aqueous acid treatment, a non-aqueous chemical delithiation, and an oxygen plasma treatment were applied to $Li[Mn_2]O_4$. It was found that Mn_3O_4 is a robust surface phase in the $Li_{1-x}[Mn_2]O_4$ system regardless of the chemical treatment and level of lithiation. The surface Mn_3O_4 phase is cubic whereas bulk Mn_3O_4 undergoes a cooperative Jahn-Teller distortion to tetragonal symmetry. Thicker Mn_3O_4 surface layers are tetragonal. Analysis of as-prepared $LiNi_{0.5}Mn_{1.5}O_4$ revealed a surface composed of mixed Mn_3O_4 and a well-known Ni-rich rock-salt phase that occurs in the $LiNi_{0.5}Mn_{1.5}O_4$ system. Trivalent doping of $LiNi_{0.5}Mn_{1.5}O_4$ with Cr

creates an ordered spinel/rock-salt phase that has not been previously observed in either the $LiNi_{0.5}Mn_{1.5}O_4$ or $LiMn_2O_4$ systems.

Table of Contents

List of Tables

List of Figures

Chapter 1: Introduction

There are as many as thirty different manganese oxide/hydroxide minerals that occur in nature; this diversity represents a rich and varied group of materials that have many useful applications including catalysis, additives in steelmaking, and batteries.[1] When considering only manganese oxides, manganese may take an oxidation state anywhere between two and seven, often as a mixture of states. The common manganese oxides that are encountered are MnO, Mn_3O_4, Mn_2O_3, MnO_2, MnO_4^{2-}, and Mn_2O_7, some of which can occur in multiple structures with varying degrees of oxygen nonstoichiometry. The surface structure and surface chemistry of these diverse manganese oxides are exploited for their favorable electrochemical properties for use in catalysis and batteries. The use of manganese oxides in batteries will be examined in greater detail.

Manganese oxide and batteries have a long history together beginning with the Leclanché cell invented and patented by Georges Leclanché in 1866, which was comprised of a zinc anode and a carbon/manganese dioxide cathode. A major improvement of the Leclanché cell was developed by Lewis Urry at Union Carbide in 1957[2] that utilizes the same anode and cathode as the Leclanché cell, but replaces the ammonium chloride electrolyte with potassium hydroxide. This cell is the common primary alkaline battery that is used in consumer electronics. Manganese oxide would later find use in another type of battery, the Li-ion battery, in 1983 when it was found that Li could intercalate into Mn_3O_4 and $Li[Mn_2]O_4$ by Thackeray et al.[3]. $LiM_xMn_{2-x}O_4$ (where M is Co, Cr, Ni, Fe, Ti, and Zn)[4,5] represents doped $Li[Mn_2]O_4$, which shows improved cyclability with a decrease in capacity of the 4.1 V plateau associated with the $Mn^{3+/4+}$ redox couple. As a consequence of this research, it was discovered that the high-

voltage redox couples of Cr (~4.9 V vs Li)[6] and Ni (~4.7 V vs Li)[7]could be accessed, improving energy density without sacrificing capacity.

$Li[Mn_2]O_4$ (LMO) and its Ni-doped derivative $LiNi_{0.5}Mn_{1.5}O_4$ (LNM) represent two of the most promising Li-ion cathode chemistries in terms of energy density and rate capability. The two cathodes are composed of a cubic spinel structure that allows for three-dimensional Li^+ diffusion, the only difference between the two being the higher voltage of the electrochemically active $Ni^{2+/3+}$ and $Ni^{3+/4+}$ redox couples of LNM, which are both located at approximately 4.7 V versus metallic lithium (Li^0) as compared to only 4.1 V for LMO. As promising as these cathodes are, both chemistries have a common problem; cyclability. As energy density increases with increasing Ni substitution in LMO, there is a dramatic shift in cycling degradation mechanisms. In the LMO system, soluble Mn^{2+} is created by the Mn disproportionation reaction ($2Mn^{3+} = Mn^{2+} + Mn^{4+}$), which is subsequently lost to the liquid organic electrolyte during cycling. In the LNM system, cycling degradation is attributed solely to the reactivity of the electrolyte with the electroactive Ni whose high redox potential is located outside of the electrochemical window of the electrolyte. Both degradation mechanisms occur at the interface between the cathode and the electrolyte, which has made it difficult to understand their exact nature. Complete characterization of the cathode's surface and composition is required in order to understand how degradation occurs in the spinel-related cathode systems because the surface structure dictates how the cathode will interact with the electrolyte.

To this end, the surface structure and chemistry of LMO and LNM were analyzed with advanced transmission electron microscopy (TEM) techniques, including aberration-corrected high-angle annular dark field (HAADF) scanning transmission electron microscopy (STEM) and electron energy loss spectroscopy (EELS). Low-dose HAADF STEM was also used to ensure the surface structures observed occurred naturally. XRD

was used to complement the TEM techniques in the identification of the bulk structure. EELS was used to identify composition and chemical environment including oxidation state information. The combined high-resolution data from EELS and HAADF STEM imaging has provided a means to understand the surface structure and surface chemistry of $Li_{1-x}Mn_2O_4$, $LiNi_{0.45}Mn_{1.55}O_4$, $LiNi_{0.5}Mn_{1.5}O_4$, and $LiNi_{0.45}Cr_{0.1}Mn_{1.45}O_4$.

Chapter 2: Experimental Methods

2.1 MATERIAL SYNTHESIS

Synthesis has a great influence on the structure and properties of a material. When focusing specifically on transition metal oxides, synthesis usually ranges from solid-state synthesis to solution-based or so called "wet chemistry" synthesis[8]. The latter includes any solution-based method of mixing, including co-precipitation, sol-gel[9,10], microemulsions, and hydrothermal[11]/solvothermal[12] synthesis techniques; only the techniques used in this research will be expounded upon. Whether a solid-state method or a solution-based technique is chosen for mixing the metal cations, the heating of the precursors is identical. Since the desired product in this case is an oxide, one only needs to heat the properly prepared precursors in atmosphere with the desired heating profile, which includes heating rate, heating time at a desired temperature, and cooling rate, all of which are dependent on the desired properties of the final product. If the sample is moisture sensitive or impurity sensitive, i.e. carbon dioxide, extra steps must be taken, such as heating in a sealed furnace under controlled atmospheric conditions. Additionally a pure oxygen atmosphere may be used if the sample has trouble achieving full oxidation of the precursor material given the limited oxidizing power of the atmosphere. Applying an overpressure of the desired atmosphere may also be employed. Even though solid-state synthesis and solution-based syntheses can produce a "pure phase" product, the properties of their products, including morphology, impurities, and particle size distribution, can vary greatly.

Solid-state synthesis represents the most widely used technique to produce bulk metal oxide powders on an industrial scale due to its cost-effective and straightforward nature. Transition metal compounds are mixed mechanically, typically by hand or in a ball mill, to obtain a degree of homogeneity before they are heated in a furnace. Usually

the first step after obtaining a well-mixed precursor powder is to decompose the precursors at some intermediate temperature, unless the powders are oxide precursors, which can be heated directly. The transition metals are usually paired with an easily decomposable anion such as carbonate, nitrate, oxalate, acetate, or hydroxide. which will yield an oxide powder under sufficient heating at an intermediate temperature. Once the precursor material is sufficiently prepared, it may be heated as a loose powder or pressed into a pellet and then heated. The advantage of the latter is that it minimizes void space and allows the shortest diffusion distances in order to achieve elemental homogeneity. The drawback to pressing a pellet is that it encourages crystal growth, which will increase particle size and sintering of the powder.

The pitfalls of solid-state synthesis may be overcome by solution-based methods, which are better at elemental mixing, but add more complexity and expense. Additionally, solution-based methods can produce smaller crystallite sizes and "pure phase" material at lower synthesis temperatures as compared with the solid-state method. This is especially useful when analyzing materials with transmission electron microscopy, which requires materials to be less than approximately 200 nm in thickness. Solution-based methods take advantage of the perfect mixing that occurs in solutions by "freezing" the randomness of the metal cations into a solid or gel precursor. The main methods explored in this research were the Pechini process[13] as adapted by Liu[14] with some modifications, a so-called modified Pechini process, and hydroxide coprecipitation.

The Pechini process is defined by the use of nitrate precursors of the metal cations, which are mixed with citric acid and ethylene glycol in a ratio of 1:1:4 to form a clear solution at 90°C. The citric acid acts as a chelating agent which coordinates with the metal cations and anchors them to a polymeric backbone composed of slowly-polymerizing, low-molecular-weight polyethylene glycol through an esterification

process that begins to occur once the solution is heated to 140°C. The viscosity of the solution increases during this step. After vacuum heating the solution at 180°C in order to remove excess ethylene glycol, the solution undergoes a polyesterification process that produces a foam or glasslike solid. At this point, the precursor may be fired at an intermediate temperature to burn off the organic material and then calcined with a desired heating profile. It was found during this study that ethylene glycol could be eliminated from the above process while maintaining the desired properties of the resulting powder; clean XRD spectra without impurities, nominal electrochemical performance, and ideal particle size (~50 nm) for TEM characterization. This modification also helped eliminate extraneous steps in the synthesis process. The modified Pechini process is outlined below.

$Li[Mn_2]O_4$ samples were prepared from lithium and manganese nitrate precursors mixed in solution with citric acid in a molar ratio of 1:1.05 cation to citric acid. The solution was then heated isothermally at 90°C until it converted into a dry foam. The foam was mixed in a mortar and pestle until homogeneous and calcined twice at 200°C for 24 h with intermediate grinding before a final heating to 600°C at a rate of 3°C/minute, held at that temperature for 24 h, and then cooled at a rate of 1°C/minute to room temperature. A synthesis temperature of 600°C was chosen to avoid the loss of oxygen from the surface[15] of the material in order to ensure the surface structure that is observed is intrinsic.

The other synthesis technique used in this study was hydroxide coprecipitation, which relies on the extremely-low solubility of transition metal hydroxides in aqueous solution. Typically, a strong base such as sodium or lithium hydroxide is added to a solution containing transition metal salts. The resulting reaction creates a cloudy solution of mixed transition metal hydroxides or oxyhydroxides. Since lithium hydroxide is

extremely soluble in water, it must be added as a solid after transition metal coprecipitation. In this way, hydroxide coprecipitation may be viewed as a hybrid solid-state/solution-based synthesis route. Dopants are easily added during the coprecipitation step of the transition metal hydroxides. This synthesis technique was used specifically for both stoichiometric, Mn-rich, and trivalently-doped $LiNi_{0.5}Mn_{1.5}O_4$. This technique was chosen over the modified Pechini process for the above samples because the modified Pechini process yielded inconsistent results when dealing with nickel nitrate; the resultant precursor powder consisted of a mixture of dry foam, similar to the LMO case, but with a viscous, green gel that segregated from the foam, which indicated poor mixing of the Ni and Mn precursors. A typical hydroxide coprecipitation synthesis is outlined below.

Mixed sodium and ammonium hydroxide was added to a 50 wt. % solution of nickel and manganese nitrate in a 3:1 stoichiometric ratio until no remaining precipitate was formed. The precipitate was then filtered and washed with distilled water and dried at 110°C. The dry, mixed hydroxides was then mixed with the stoichiometric amount of lithium hydroxide and pressed into pellets. The pellets were then preheated to 600°C for 6 hours to decompose the precursors. The resultant pellet was ground into a fine powder in a mortar and pestle, repressed into a pellet, and heated to 900°C for 12 hours followed by cooling to room temperature. Different cooling rates were used for these samples and are outlined in relevant sections.

An additional sample used in this study was not synthesized, but rather purchased commercially. This sample was purchased from the MTI Corporation P/N: EQ-Lib-LMO and is clearly labeled as a commercial sample.

2.2 MATERIAL TREATMENTS

Material treatments were applied only to LMO in order to better understand the nature of the surface reconstructions observed in that system. The three chemical treatments outlined below were applied to the sample synthesized in this study (synthesized sample). Only the acid-treatment was applied to the commercial LMO sample.

2.2.1 Acid Treatment

An acid treatment was applied to both the synthesized and commercial LMO samples based on the procedure outlined by Hunter.[16] A solution of dilute sulfuric acid was added dropwise, with stirring, to a solution containing LMO powder and deionized water. The pH of the solution was carefully monitored with a pH meter during the span of the treatment. A drop was added every 5-10 seconds over the course of several hours until the solution reached a pH value between 0.3 and 2.3, below the value of 2.5 indicated for complete conversion of LMO to λ-MnO_2 by Hunter. The solution was then covered and stirred overnight to ensure completion of the reaction. Afterwards, the sample was vacuum-filtrated and rinsed several times with deionized water. The final product was vacuum-dried at 90°C overnight.

2.2.2 Chemical Delithiation Treatment

A non-aqueous chemical delithiation treatment was applied to the synthesized LMO sample as described in a previous study[17]. LMO was added to 50 ml of dry acetonitrile in a flask purged with nitrogen. Nitronium tetrafluoroborate was added to the solution in a molar ratio of LMO to NO_2BF_4 of 1:2.63. The solution was stirred for two days to ensure complete reaction after which the solution was vacuum-filtered to remove the reacted LMO powder. The powder was rinsed several times with acetonitrile in order

to remove excess NO_2BF_4 and $LiBF_4$. The resultant powder was then dried under vacuum at room temperature.

2.2.3 Oxygen Plasma Treatment

An oxygen plasma treatment was applied to the synthesized LMO sample with microwave-generated oxygen plasma within a Microwave Plasmatic Systems Inc. Plasma Preen II 862. LMO powder was dispersed on a glass slide and placed in the oxygen plasma chamber under a flow of ~1 standard cubic feet per hour (SCFH) of 99.999% oxygen to achieve ~1 Torr dynamic pressure. A continuous power of 750 W was applied to the gas flow in order to create the oxygen plasma. The plasma was applied to LMO in 15-minute intervals, stopping periodically to cool the reactor cover, for a total of 1 hour. The temperature of the reactor cover was measured after each 15-minute period; it never exceeded 195°C and the maximum substrate temperature was conservatively estimated to be < 300°C.

2.3 MATERIALS CHARACTERIZATION

2.3.1 Powder X-Ray Diffraction

Powder XRD spectra were obtained with either a Philips XPERT Theta-Theta Diffractometer or a Rigaku MiniFlex diffractometer with Cu Kα radiation over a 2θ range between 10 and 90° with a step size of 0.02°. XRD spectra were analyzed with Rietveld refinement using PDXL-2 software.

2.3.2 Scanning Transmission Electron Microscopy

Transmission electron microscopy is a characterization technique that can resolve structural and chemical properties of materials with an electron beam. There are many different ways that an electron beam may interact with a sample, so before choosing an

appropriate TEM technique, the type of information that is desired must be considered. Since the goal of this research was to completely characterize the surface structure and surface chemistry of the LMO-related systems, aberration-corrected high-angle annular dark-field scanning transmission electron microscopy, which includes electron energy loss spectroscopy, was chosen as the preferred TEM technique.

2.3.2.1 High-Angle Annular Dark-Field STEM

HAADF STEM scans a sufficiently-thin sample (< 200 nm thickness) with a convergent electron probe and detects the interactions with different types of detectors, which are discussed in further detail below. A schematic of the imaging mode of HAADF STEM is shown in Figure 2-1. An electron probe is rastered across a sample that is oriented so as to have like atoms aligned in columns parallel to the beam direction. Electrons interact with the atomic columns and are scattered through a particular angle based on its atomic number; heavier elements scatter electrons at higher angles. That is why HAADF STEM is considered "z-contrast" imaging. An annular electron detector counts the electrons scattered from a particular position, and an image is recreated from the collected information. Better spatial resolution is obtained with finer probes, which has been possible due to aberration correctors. Aberration correction enables electron probes to be smaller than 1 Å.[18]

The HAADF STEM images presented in this work are taken on either an aberration-corrected JEOL ARM200F TEM or an aberration-corrected FEI Titan TEM at 200 kV acceleration voltage with a convergence angle between 21.0 and 30.0 mrad. Each STEM image indicates the microscope used, the dose rate, the total dose for the image, and a geometric factor (GF). The geometric factor is an approximation of electron probe overlap when scanning at high magnifications. It is included as a multiple in the dose

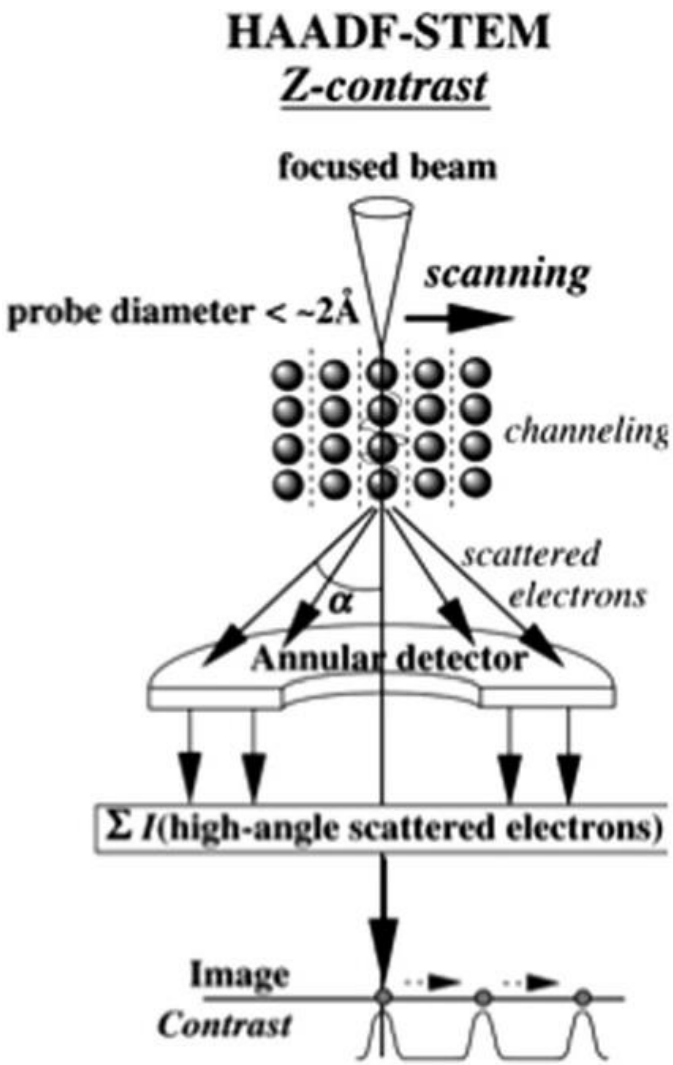

Figure 2-1: Schematic representation of HAADF STEM[19] scanning a crystal composed of atomic columns of a particular element. Electrons that interact with the atomic columns are scattered through a particular angle based on its atomic number; heavier elements scatter electrons at higher angles. An annular detector counts the electrons scattered from a particular position, and an image is recreated from the collected information.

calculation. If no such probe overlap exists, the geometric factor is 1. A probe diameter of ~1.0 Å is assumed in all calculations for dose rate and dose. All STEM images were collected under high-vacuum conditions (< 1 x 10^{-7} Torr).

2.3.2.2 STEM Simulations

Before HAADF STEM images may be interpreted, it is important to first simulate the crystal structure of interest and find the relevant zone axes that allow like atoms to be aligned into individual columns. Once the relevant zone axes are found and the material is simulated, phases may be identified directly from HAADF STEM images. For LMO and all related structures, the most interpretable zone axes are ⟨110⟩, which are shown in Figure 2-2. LMO, cubic Mn_3O_4, and rock-salt phases all contain the $[Mn_2]O_4$ cubic spinel framework with the only differences being how the transition metals are ordered on the 8a and 16c sites. LNM and related phases contain a $[Ni_{0.5}Mn_{1.5}]O_4$ cubic spinel framework that is isostructural with $[Mn_2]O_4$.

For this work, atomic models for STEM simulations were created in VESTA[20] and transferred to the HREM Simulation Suite having a TEM/STEM simulation software package based on the FFT multislice technique[21]. The HREM Simulation Suite evaluates, based on the approximation of Weickenmeier and Kohl[22], both the wave function and its Fourier transform at each slice to calculate the elastic scattering amplitude. This approximation is appropriate for electrons scattered at high angles, which is the geometry for recording HAADF images[23,24]. The HAADF intensity is then calculated by adding the thermal diffuse scattering factor to the elastic scattering amplitude. This term is important as atomic vibrations dampen the intensity of the electron waves as they pass through the specimen. The microscopy parameters used for the simulations include an acceleration voltage of 200 kV, a condenser aperture of 20 μm, a convergence angle of 16-18 mrad, HAADF collection angles between 50-180 mrad, a sample thickness of 50 nm and a probe diameter of 0.8 Å. These parameters correspond to the settings used in the operation of the JEOL ARM200F and FEI Titan microscopes. For each structure, the multislice simulations were carried out by assuming a step scanning size of 0.2 Å (less

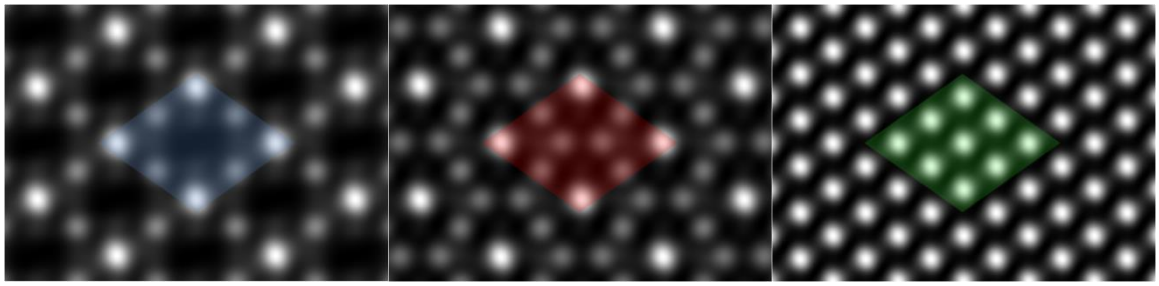

Figure 2-2: STEM simulations used for phase identification. The left figure represents $LiMn_2O_4$ and $LiNi_{0.5}Mn_{1.5}O_4$ (blue diamond). The substitution of Ni for Mn does not lead to a perceptible difference in the image. The center figure is cubic Mn_3O_4 (red diamond). The right figure is a rock-salt phase (green diamond). All of the simulations are viewed along the [110] zone axis.

than the distance to be resolved) and a minimum slice thickness of 1.0 Å.

Mn_3O_4 phases were identified as cubic or tetragonal by comparing direct measurements of the STEM images with ideal structures.

2.3.2.3 Low Dose Scanning Transmission Electron Microscopy

Oxide materials can be sensitive to electron-beam-induced phase changes[25] so it is important to lower the electron dose and dose rate sufficiently so that a determination can be made whether any impurity phases observed are an effect of the material or an effect of the electron beam. This research answers that question for the LMO system with low-dose STEM by reducing the electron beam to pseudo non-destructive levels. This work serves as an example of the importance of low-dose STEM as a critical technique for correctly identifying transformations and reconstructions in oxide or related materials.

Typical low-dose (2.6×10^3 $e^-/Å^2$) and medium-dose (1.3×10^5 $e^-/Å^2$) HAADF STEM imaging conditions as well as high-dose (4.8×10^7 $e^-/Å^2$) EELS collection conditions are shown in Table 1. Dose conditions are generalized as low-dose, medium-dose, or high-dose for every HAADF STEM/EELS image unless otherwise specified.

Low-Dose STEM Conditions	
Probe Current	4.3 pA
Probe Diameter	~1.0 Å
Dose Rate	$\left(3.4\ x\ 10^{7}\ \frac{e^{-}}{Å^{2}\cdot s}\right)$
Pixel Dwell Time	10.0 µs
Geometric Factor	7.8
Dose	$\left(2.6\ x\ 10^{3}\ \frac{e^{-}}{Å^{2}}\right)$
Medium-Dose STEM Conditions	
Probe Current	12.7 pA
Probe Diameter	~1.0 Å
Dose Rate	$\left(1.0\ x\ 10^{8}\ \frac{e^{-}}{Å^{2}\cdot s}\right)$
Pixel Dwell Time	31.8 µs
Geometric Factor	40
Dose	$\left(1.3\ x\ 10^{5}\ \frac{e^{-}}{Å^{2}}\right)$
High-Dose EELS Conditions	
Probe Current	30 pA
Probe Diameter	~1.0 Å
Dose Rate	$\left(2.4\ x\ 10^{8}\ \frac{e^{-}}{Å^{2}\cdot s}\right)$
Pixel Dwell Time	200 ms
Geometric Factor	1
Dose	$\left(4.8\ x\ 10^{7}\ \frac{e^{-}}{Å^{2}}\right)$

Table 2-1: Typical HAADF STEM/EELS imaging conditions.

Low-dose, medium-dose, and high-dose are relative terms used to express increasingly higher doses, each term separated by many orders of magnitude. The low-dose STEM

imaging in this work is within an order of magnitude of the low-dose STEM imaging conditions established by Buban et al.[26] and represents the lowest dose practicable. The acceleration voltage was held to 200 kV unless otherwise specified.

Whenever probe currents were not provided by the TEM system, they were measured with a picoammeter at the large phosphorus viewing screen, the small phosphorus viewing screen, and at the sample with a faraday cup holder. The currents measured at the faraday cup were the currents used for dose calculations.

2.3.3 Electron Energy Loss Spectroscopy

Electron energy loss spectroscopy (EELS) is able to provide chemical information such as oxidation states of transition metals and relative oxygen content with high spatial resolution. Because of these advantages, EELS was used to characterize the surface chemistry of LMO-related systems. A schematic of how EELS works is provided in Figure 2-3. HAADF STEM relies on elastic scattering of electrons at high angles while EELS relies on the inelastic scattering of electrons at low angles. Inelastic interactions include phonon excitations, inter-band and intra-band transitions, plasmon excitations, and inner shell ionizations. The spectrum of inelastic electrons gives a unique fingerprint of the material that is studied. High energy resolutions, as high as 0.1eV[27] with 10meV on the horizon[28], provide a means to correctly identify individual oxidation states of transition metal oxides.

EELS spectra were collected on a FEI Titan TEM at 200 kV acceleration voltage and a NION UltraSTEM100 at 100 kV acceleration voltage. EELS collection represents the highest dose rate and dose applied to the samples so it is typically labelled a high-dose condition unless the actual dose and dose rates are provided. A typical convergence angle of 21 mrad was used unless otherwise specified. EELS data were collected under

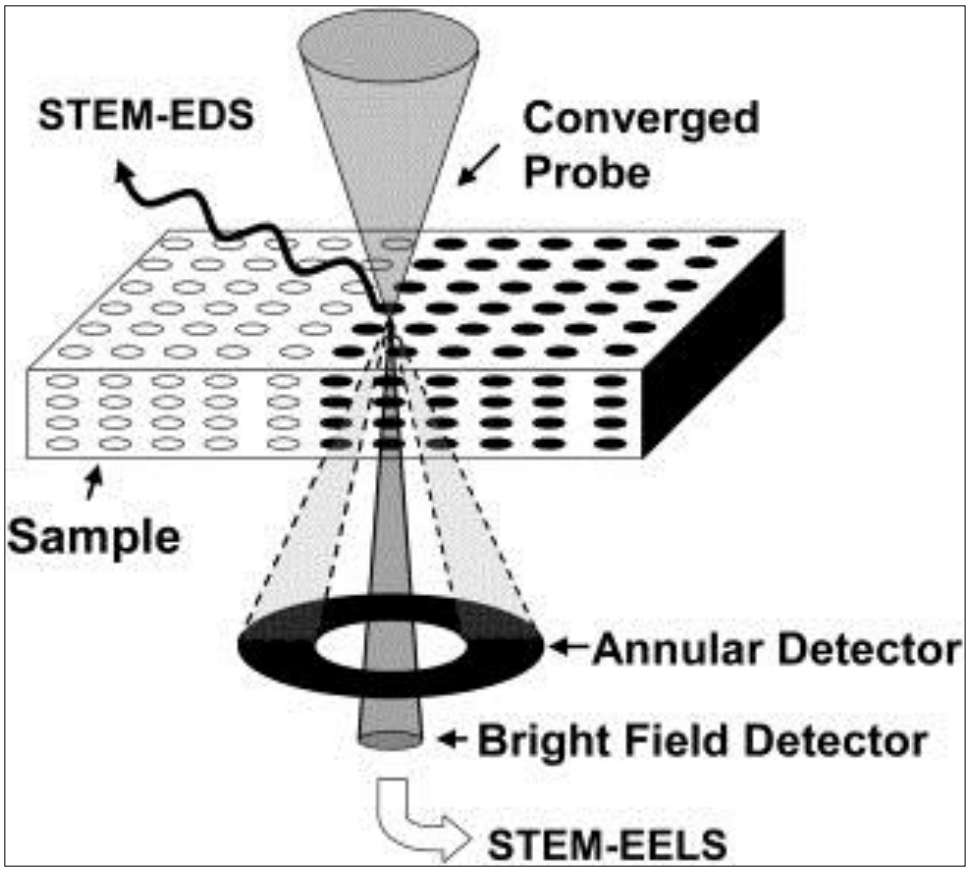

Figure 2-3: Schematic of EELS collection[29]. Inelastically scattered electrons are scattered at low angles and guided into the EELS system, which uses a magnetic prism to create a dispersion of the different inelastically-scattered electrons. The resulting spectrum is collected with a high-resolution camera. There are three different types of spectra that may be collected; a single spectrum, a line scan, which represents a one-dimensional array of spectra, or a spectrum image, which represents a two-dimensional array of spectra.

high-vacuum conditions (< 1 x 10^{-7} Torr). Usually during EELS collection, the low-loss region including the zero loss peak (ZLP) was collected. This is referred to as dual EELS, and it is important for data analysis, which is detailed in the next section.

2.3.4 EELS Data Analysis

After an EEL spectrum image is obtained, it must be processed correctly in order to obtain useful information. The first thing that usually happens is a high-quality dark

reference correction, which reduces noise in the spectrum image. The next item to correct is beam shift, which can be fixed with the low-loss spectrum obtained with dual EELS. Tracking the shift of the ZLP creates an offset map with which to correct the core-loss spectrum image. The result is a spectrum image that can be used for proper multiple linear least squares (MLLS) fitting and that displays the correct eV values with which to compare with other studies.

2.3.4.1 Multiple Linear Least Squares

Multiple linear least squares (MLLS) fitting is a way to fit a particular spectrum or spectrum image with spectra that represent different chemical species. The fitting components may be taken from the original spectrum image or they may be used from other sources, but it must be ensured that the sources are properly prepared such as correcting for energy shift. MLLS fitting uses a linear combination of the fitting spectra in order to minimize the difference between the original spectrum and the fitted spectrum. This fitting represents a straightforward approach for analyzing EELS spectrum images for chemical content.

2.3.4.2 Principal Component Analysis

A complementary technique that may be used to clean noisy spectrum images is to apply principal component analysis (PCA) to EELS[30]. PCA uses matrix mathematics to decompose a line scan or spectrum image into orthogonal components, not necessarily physically interpretable ones, in order to increase the signal-to-noise ratio (SNR). PCA works because of inherent oversampling in EELS collection, and therefore signal redundancy in the spectrum image, but it also makes it less sensitive to local chemical changes. In this way PCA may throw out important data or introduce artifacts in the "cleaned" spectrum image.

2.3.4.3 Independent Component Analysis

A drawback to MLLS fitting is that it uses known spectra to fit a spectrum of interest. In the case of complex systems or systems that contain unknown chemical species, it is useful to use blind source separation, otherwise known as independent component analysis (ICA) to analyze EELS spectra[31]. ICA builds on PCA by looking for mutually orthogonal components of the spectrum image, which if analyzed correctly represent physically interpretable spectra. There are many useful ways to apply ICA to EELS[32], but Hyperspy[33] using the CuBICA algorithm was chosen for this work due to its ease of use and computing efficiency.

2.4 ELECTROCHEMICAL CHARACTERIZATION

Additional to materials characterization, electrochemical characterization was performed on cathode powders in order to verify that the correct material properties were achieved.

2.4.1 Coin Cell Fabrication

LMO electrodes were prepared by mixing 78.0 wt% active material in a mortar and pestle with 10.4 wt% carbon and 11.6 wt% polyvinylidene fluoride (PVDF) that was dissolved to 5 wt% in N-Methyl-2-pyrrolidone (NMP) and added from solution. The resulting slurry was cast on aluminum foil and heated at 110°C overnight to dry it. The dried electrode composite was passed through a rolling press to condense it; 5/8”-diameter discs were cut from the sheets. These discs included both electrodes and bare aluminum current-collector discs. The final weight of the electrodes was determined by subtracting the average weight of the bare aluminum discs, 0.0117g, from the disc-electrode weight. Typical active material masses were ~ 4 mg. CR2032 coin cells with LMO cathodes were assembled in an argon-filled glove box with metallic lithium (Li^0) as

the anode, 1 M $LiPF_6$ in 1:1 ethylene carbonate: diethyl carbonate as the electrolyte and Celgard polypropylene separators.

2.4.2 Galvanostatic Cycling

The cells rested for 6 h before they were galvanostatically cycled at room temperature at a C/10 rate for both charge and discharge between 3.2 and 4.4 V versus Li^0; the cells were first charged.

Chapter 3: Surface Reconstruction in $LiMn_2O_4$

The spinel $Li[Mn_2]O_4$ is a candidate cathode for a Li-ion battery, but its capacity fades over a charge/discharge cycle of $Li_{1-x}[Mn_2]O_4$ ($0 < x < 1$) that is associated with a loss of Mn to the organic-liquid electrolyte. It is known that the disproportionation reaction $2Mn^{3+} = Mn^{2+} + Mn^{4+}$ occurs at the surface of a Mn spinel, and it is important to understand the atomic structure and composition of the surface of $Li[Mn_2]O_4$ in order to understand how Mn loss occurs. We report a study of the surface reconstruction of $Li[Mn_2]O_4$ by aberration-corrected scanning transmission electron microscopy[1]. The atomic structure coupled with Mn-valence and the distribution of the atomic ratio of oxygen obtained by electron energy loss spectroscopy reveals a thin, stable surface layer of Mn_3O_4, a subsurface region of $Li_{1+x}[Mn_2]O_4$ with retention of bulk $Li[Mn_2]O_4$. This observation is compatible with the disproportionation reaction coupled with oxygen deficiency and a displacement of surface Li^+ from the Mn_3O_4 surface phase to a subsurface $Li_{1+x}[Mn_2]O_4$ layer. These results provide a critical step toward understanding how Mn is lost from $Li[Mn_2]O_4$, once inside a battery.

3.1 INTRODUCTION

The spinel $Li[Mn_2]O_4$ (LMO), a candidate cathode for lithium-ion batteries, is known to undergo the disproportionation reaction $2Mn^{3+} = Mn^{2+} + Mn^{4+}$ at its surface. In addition, $Li[Mn_2]O_4$ has been shown by Hunter[16] to convert to λ-MnO_2 by the extraction of Li^+ and Mn^{2+} in a strong acid to leave Mn^{4+} in the spinel octahedral-site framework $[Mn_2]O_4$. Electrochemical extraction of Li from $Li_{1-x}[Mn_2]O_4$ is reversible over $0 < x < 1$

[1] C. D. Amos, M. A. Roldan, M. Varela, J. B. Goodenough, P. J. Ferreira, "Revealing the Reconstructed Surface of $Li[Mn_2]O_4$," *Nano Letters*, Vol. 16, Issue 5, pp. 2899-2906 (2016). All of the research performed in the above work except EELS collection and analysis were performed by Charles D. Amos.

at ~ 4.0 V versus a metallic-lithium (Li^0) anode[34], which is well-matched to the highest occupied molecular orbital (HOMO) of the conventional organic liquid-carbonate electrolytes used in a Li-ion battery. This match makes the $Li_{1-x}[Mn_2]O_4$ spinel system of interest for a low-cost cathode of a Li-ion battery. However, problems with loss of Mn^{2+} from the surface on cycling causes a capacity fade. Additionally, the spinel $Li[Ni_{0.5}Mn_{1.5}]O_4$ provides a high-voltage cathode having a Ni^{4+}/Ni^{2+} redox energy pinned at the top of the O-2p bands at about 4.7 - 4.8 V versus Li^0; the electrolyte is oxidized at a V > 4.3 V. This latter spinel is also of fundamental interest because there is a loss of oxygen above 700°C that induces a segregation of a Ni-rich rock-salt phase that is reabsorbed into the spinel phase on cooling through 700°C[35]. Moreover, $Li_{1+x}[Mn_2]O_4$ ($0 \leq x < 1$) also retains the spinel framework $[Mn_2]O_4$ with the Li being cooperatively displaced from the spinel tetrahedral sites to interstitial octahedral sites of the $[Mn_2]O_4$ framework[3]. These observations show that $Mn^{2+}[Mn_2^{3+}]O_4$, $Li_{1+x}[Mn_2]O_4$, and rock-salt MnO have in common a close-packed-cubic oxide-ion array with the possibility of a facile redistribution of their cations to promote the disproportionation reaction in a surface reconstruction. We have investigated the surface structure of as-prepared $Li[Mn_2]O_4$ and show the existence of a thin $Mn^{2+}[Mn_2^{3+}]O_4$ surface phase and a subsurface $Li_{1+x}[Mn_2]O_4$ phase with bulk $Li[Mn_2]O_4$ retained; all three phases have the spinel $[Mn_2O_4]$ framework with a redistribution of the interstitial cations.

3.2 EXPERIMENTAL METHODS

3.2.1 Material Synthesis

See section 2.1 Material Synthesis for $LiMn_2O_4$ synthesis procedure. X-ray powder diffraction (XRD) spectra of the final products were obtained with a Philips

XPERT Theta-Theta Diffractometer and Cu Kα radiation with a step size of 0.02° over the 2θ range 10 to 90°.

3.2.2 Electrochemical Cycling

See section 2.4 Electrochemical Characterization for $LiMn_2O_4$ coin cell fabrication and electrochemical cycling.

3.2.3 STEM/EELS

Low-dose (2.6 x 10^3 $e^-/Å^2$) and medium-dose (1.3 x 10^5 $e^-/Å^2$) HAADF STEM images were taken on a JEOL ARM200F with a 200 kV acceleration voltage and a probe diameter of ~1.0 Å. In the gun-lens system, an A1 anode voltage of 3.14 kV and an A2 anode voltage of 7.05 kV were used. Probe currents were measured with a picoammeter at the large phosphorus viewing screen, the small phosphorus viewing screen, and at the sample with a faraday cup holder. The currents measured at the faraday cup were the currents used for dose calculations. For low-dose STEM imaging, the probe current was 4.3 pA with a pixel dwell time of 10 µs. For medium-dose STEM imaging, the probe current was 12.7 pA with a pixel dwell time of 31.8 µs. High-dose (4.8 x 10^7 $e^-/Å^2$) EELS collection was performed on a NION UltraSTEM100 at 100 kV with a collection angle of 48 mrad, a probe current of 30 pA, a probe diameter of ~1.0 Å and a pixel dwell time of 200 ms. Low-dose, medium-dose and high-dose are relative terms used to express increasingly higher doses, each term separated by many orders of magnitude. The low-dose STEM imaging in this work is within an order of magnitude of the low-dose STEM imaging conditions established by Buban et al.[26] and represents the lowest dose practicable. All STEM images and EELS data were collected under high vacuum conditions (< 1 x 10^{-7} Torr) on as-prepared, uncycled LMO particles.

3.2.4 STEM Simulations

See section 2.3.2.2 STEM Simulations.

3.3 RESULTS

The Li:Mn ratio of our LMO sample was determined by inductively coupled plasma optical emission spectrometry (ICP-OES) to be 1.05:2.00 compared to the ideal 1.00:2.00. Electrochemical cycling (Figure 3-1) gave the characteristic voltage profile and capacity of LMO in good agreement with literature data[36]. XRD of the as-prepared LMO powder confirmed the spinel structure (space group $Fd\bar{3}$m) without any visible impurities (Figure 3-2). The lattice parameter was 8.222 Å.

For STEM imaging, the sample was tilted to be viewed along the [110] cubic axis of the spinel structure where like-atom columns are parallel to the electron beam. In order to facilitate interpretation of the HAADF STEM images, a structural model of LMO was built and rotated along the [110] cubic-spinel axis, as shown in Figure 3-3A. A diamond unit (shaded-blue area) is characteristic of the spinel structure and is referred to as the LMO diamond. The periphery of the diamond consists of octahedral-site Mn atoms (shown in purple); the tetrahedral sites occupied by Li in LMO are shown in green and the oxygen atoms are shown in red. Due to the mass-thickness contrast of the atomic columns in the HAADF STEM images of Figure 3-3B, only the Mn atoms of the diamond periphery are visible.

Figure 3-4 shows a medium-dose (1.3×10^5 $e^-/Å^2$) STEM image of an LMO sample where both the bulk and the surface are visible. The bulk of the sample shows the LMO diamonds indicative of the $[Mn_2]O_4$ spinel framework; however, the surface shows quite clearly LMO diamonds containing Mn in the tetrahedral sites, which is indicative of a surface reconstruction where Mn ions displace the surface Li to a subsurface

$Li_{1+x}[Mn_2]O_4$ phase. The surface phase (Figure 3-5) can be characterized by two columns of Mn occupying the Li tetrahedral sites within the LMO diamond, or equivalently, as a

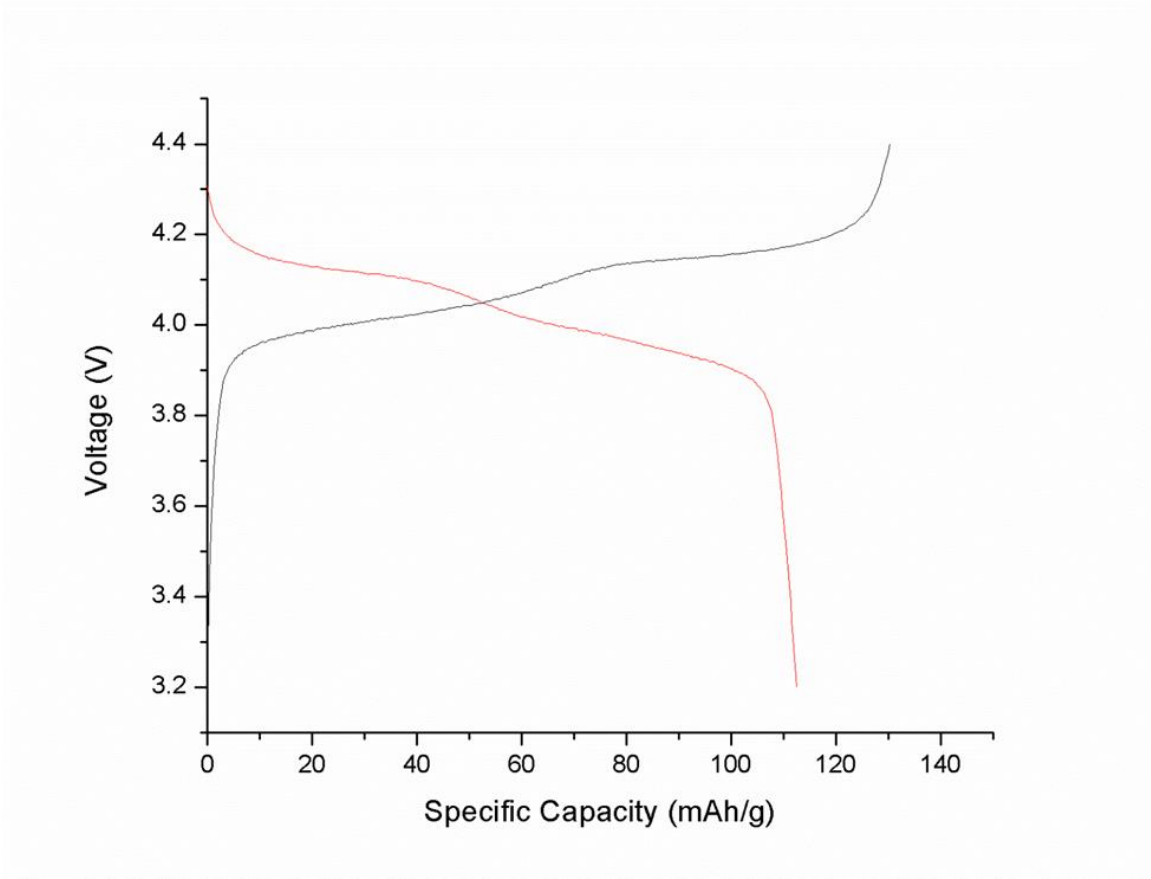

Figure 3-1: First galvanostatic cycle of LMO, charging first (black line) to 4.4V and then discharging (red line) to 3.2V. Observed in the profile are the two intrinsic plateaus characteristic of $LiMn_2O_4$.

hexagonal ring of Mn columns with a brighter column of Mn in the center; we refer to this surface-phase as the "ring-phase". There is no room for the Li in the ring phase, and only oxygen can be displaced to the vacuum. The stable $Li_{1+x}[Mn_2]O_4$ phase is known to have an $x > 0.8$ with the Li displaced to the octahedral sites of the interstitial space of the $[Mn_2]O_4$ framework[3]. However, the contrast of a HAADF STEM image of the

$Li_{1+x}[Mn_2]O_4$ phase is indistinguishable from the LMO diamond image. Instead, due to the occupancy of excess Li in the $Li_{1+x}[Mn_2]O_4$ phase, the LMO and $Li_{1+x}[Mn_2]O_4$ can be distinguished by their unique Mn oxidation states.

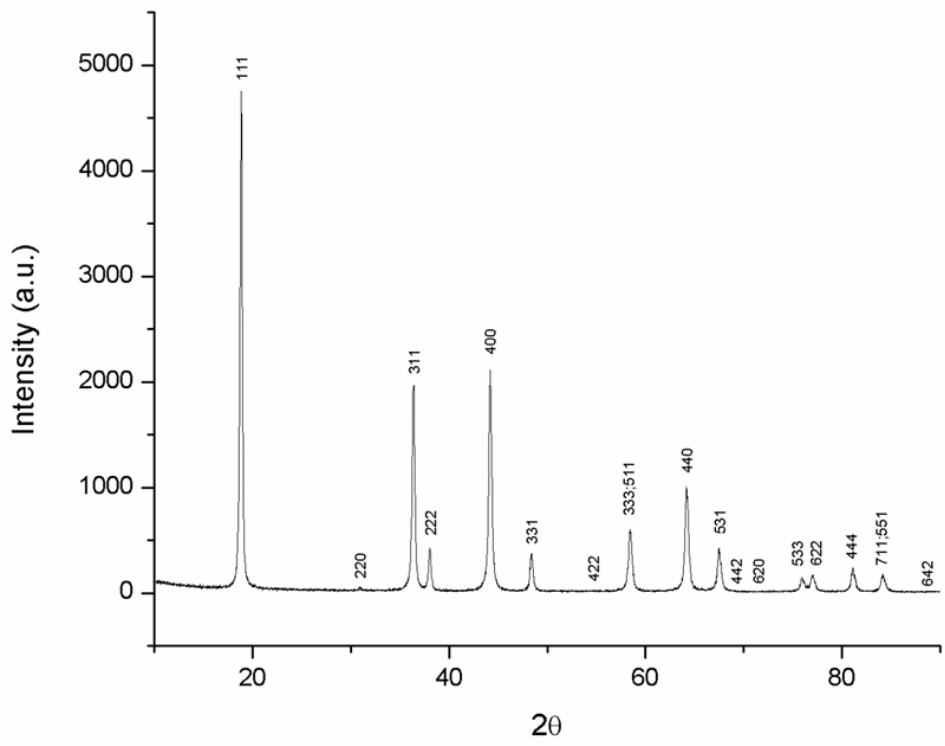

Figure 3-2: XRD pattern of LMO confirming the spinel phase and the absence of impurities.

In order to determine the distribution of Mn valence states in LMO, the tip of a particle was analyzed along the cubic spinel [110] axis with a 100 keV NION UltraSTEM in high-dose (4.8×10^7 $e^-/Å^2$) EELS mode; the images were taken after the bulk LMO diamonds and surface ring phases had been confirmed. The results are presented in Figure 3-6. Three distinct compositional ranges were identified by their unique EELS

signatures[37]. The surface layer of the particle to a depth equal to that of the observed ring-phase layer was found to contain a mixture of Mn^{3+} and Mn^{2+} ions as in $Mn^{2+}[Mn_2^{3+}]O_4$; the bulk contained a mixture of Mn^{4+} and Mn^{3+} as expected for $Li[Mn^{4+}Mn^{3+}]O_4$; and

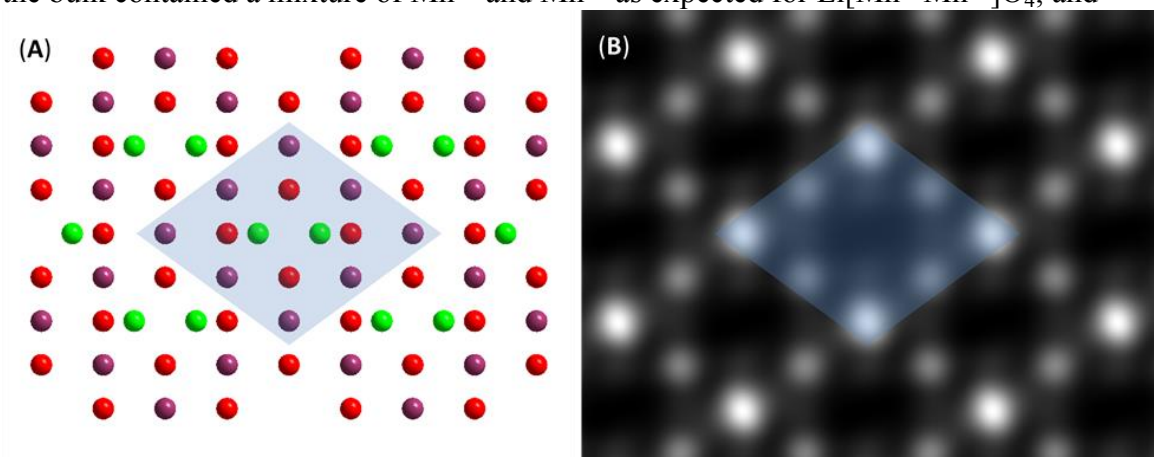

Figure 3-3: (A) Atomic structural model of LMO viewed along the cubic [110] axis. Li atoms (green) occupy tetrahedral sites and Mn atoms (purple) occupy octahedral sites within a face-centered-cubic array of oxygen atoms (red). Indicated in the model is a blue-colored diamond having on its periphery the Mn atoms of the $[Mn_2]O_4$ framework. (B) Corresponding simulated HAADF STEM image in which bright spots correspond to columns of Mn. Among these, the brighter spots are associated with Mn columns containing a higher number of atoms.

a region intermediate to the bulk and surface phases consisted almost exclusively of Mn^{3+} ions as expected for $Li_{1+x}[Mn_2]O_4$ ($x > 0.8$), but the layer is cubic and not tetragonal. Further analysis of the EELS data of Figure 3-6 shows an oxygen deficiency near the surface. Although there may be some loss of surface oxygen during the high-dose EELS experiments, the shift in Mn valence from Mn^{3+} and Mn^{2+} at the surface to an all-Mn^{3+} subsurface to Mn^{4+} and Mn^{3+} in the bulk is qualitatively indicative of the shift observed during low-dose and medium-dose STEM imaging. Upon further refinement of the electron energy loss spectra in Figure 3-6, the atomic percent oxygen is found to be approximately 57% for the near-surface region and 66% for both the intermediate and

bulk regions; these values are very close to the ideal full oxygen-coordination values of 57.1% for $Mn^{2+}[Mn_2^{3+}]O_4$ and 66.7% for $Li[Mn^{4+}Mn^{3+}]O_4$ and $Li_{1+x}[Mn_2]O_4$ ($x > 0.8$).

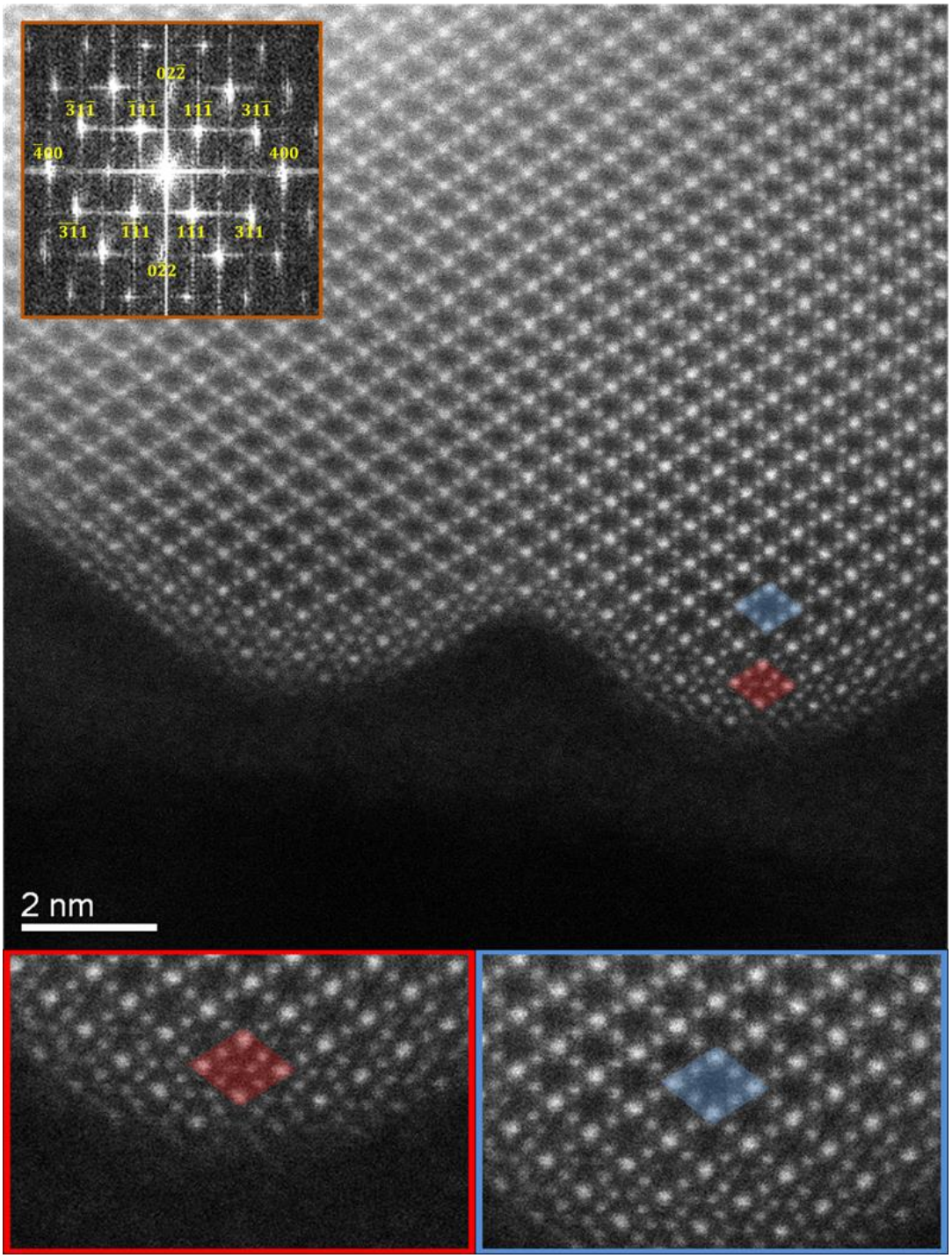

Figure 3-4: HAADF STEM image of LMO viewed along the [110] zone axis (top). LMO diamonds (blue) are found in the bulk while a new phase (red diamond) is visible at the surface. A fast Fourier transform (FFT) of the original full image is included to indicate the crystal orientation (top inset). Magnified images of the new phase and the LMO diamond are included on the bottom left and right, respectively.

3.4 DISCUSSION

Benedek and Thackeray[38] have argued that all three {100}, {110}, and {111} spinel surface planes of LMO are unstable and would undergo a reconstruction. They also indicated that all surfaces of LMO contain, on average, a lower Mn oxidation state than their bulk counterparts, which would necessitate a deficiency of oxygen in order to balance charge. However, it has been unknown what surface reconstruction should take place and what phases should form at the surface of LMO. Richard et al.[39] investigated with XRD the reduction of LMO under a flow of ammonia and proposed the following reaction:

$$18LiMn_2O_4 + 8NH_3 = 9Li_2Mn_2O_4 + 6Mn_3O_4 + 12H_2O + 4N_2$$

which corresponds to the creation of both a Li-rich ($Li_2Mn_2O_4$) and a Mn-rich (Mn_3O_4) spinel phase upon the loss of oxygen from the surface of LMO.

In our experiments, a surface layer of the spinel ring phase (Mn_3O_4) is stabilized on every surface including the low index surfaces mentioned specifically by Benedek and Thackeray. There is also a Li-rich subsurface layer as indicated with the spectra acquired with EELS. These observations are consistent with the mechanism shown by Richard et al. and with the assertions proposed by Benedek and Thackeray.

$Li[Mn_2]O_4$ contains 50:50 Mn^{4+}:Mn^{3+}, so its surface can undergo the Mn disproportionation reaction ($2Mn^{3+} = Mn^{2+} + Mn^{4+}$) with corresponding oxygen deficiency to create a stable surface layer of $Mn^{2+}[Mn_2^{3+}]O_4$. Mn^{2+} can be expected to induce a surface restructuring in which the Mn^{2+} displace Li^+ from the tetrahedral sites to a subsurface phase to maintain stoichiometry. Mn^{2+} has a strong tetrahedral-site preference and $Li_{1+x}[Mn_2]O_4$ with $x > 0.8$ is a stable phase with all the Li in the interstitial octahedral sites of the spinel framework; the surface Mn_3O_4 spinel phase is essentially 2D. This surface reconstruction creates a more stable, cation-dense surface

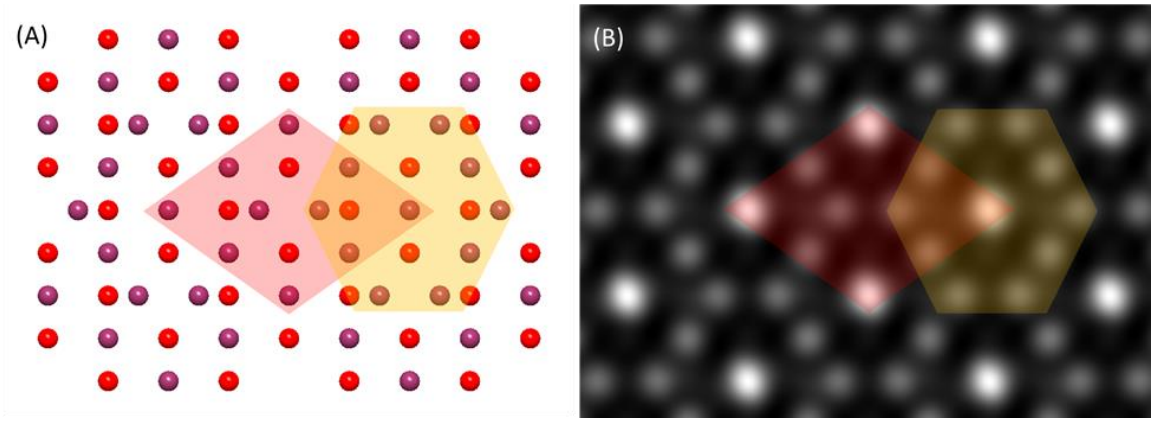

Figure 3-5: (A) Atomic structural model of the Mn_3O_4 along the [110] zone axis. Mn atoms (purple) occupy both octahedral and tetrahedral sites. The oxygen atoms are depicted in red. The orange-colored hexagon is an alternative unit to recognize the formation of Mn_3O_4. In this case the periphery contains Mn columns of similar mass, forming a ring-type structure, while the center is composed of a higher density Mn column. This is the origin of the name "ring phase." (B) Corresponding simulated HAADF STEM image.

layer that is oxygen deficient as compared to stoichiometric LMO in order to achieve local charge neutrality.

Benedek and Thackeray suggest that pristine LMO surfaces are unstable and therefore have to undergo a reconstruction. Either the surface will always reconstruct in the manner discussed above and is stable during STEM observation or the act of STEM observation causes the reconstruction of LMO's pristine yet unstable surfaces. Both scenarios would result in the surface reconstruction shown in this work. The only way to determine if the surface reconstruction of LMO is electron-beam-induced and not native is to minimize the effect of the electron beam and observe an unreconstructed LMO surface. An effort was made to minimize the electron dose delivered during HAADF STEM imaging in accordance with established low-dose STEM conditions[26]. Figure 3-7B shows a Fourier-filtered image of LMO in which the surface Mn_3O_4 phase is observed, even under low-dose STEM conditions (2.6×10^3 $e^-/Å^2$). Figure 3-7C shows a higher

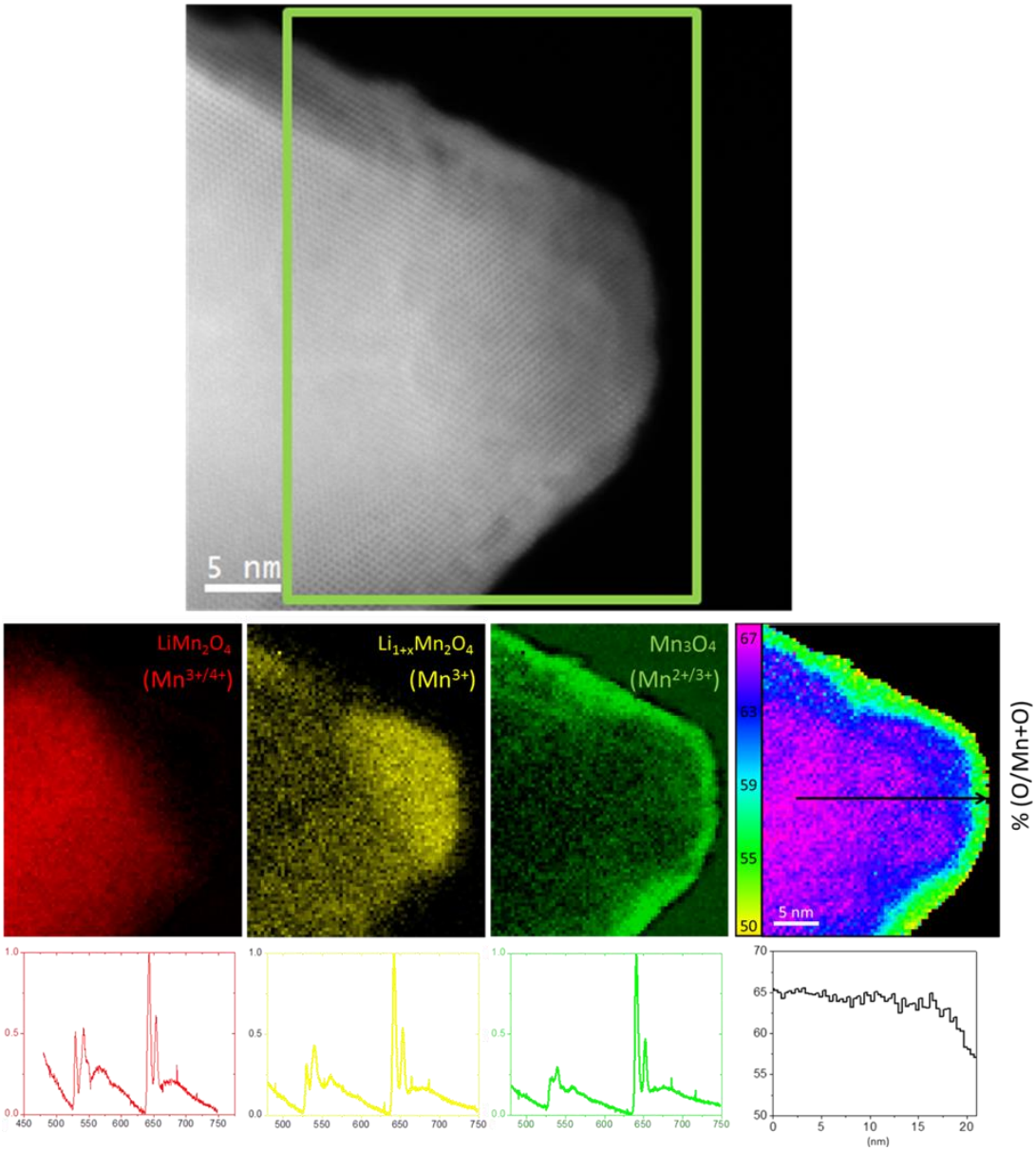

Figure 3-6: HAADF STEM image of an LMO particle (top). The green rectangle in the STEM image shows the area from where an EEL spectrum image was acquired. The colored maps (red, yellow, and green) and corresponding colored spectra below each image, represent the location of different Mn valence states within the nanoparticle. The atomic ratio of oxygen extracted from the O-K and Mn-$L_{2,3}$ edges is shown (middle right). The black arrow shows where the atomic ratio of oxygen (bottom right) was extracted. The ratio is determined by the number of oxygen atoms to the total number of atoms in the sample.

magnification image of the same surface in Figure 3-7A, which illustrates the stability of the surface even under higher-dose conditions (5.3 x 10^4 $e^-/Å^2$). When LMO is damaged purposefully with a very high electron dose (1.5 x 10^9 $e^-/Å^2$) from an EELS probe, the LMO spinel structure converts into a completely different structure – the rock-salt structure (Figure 3-8) – which is not otherwise observed. From this result, we conclude that if the Mn_3O_4 ring phase was indeed caused by the electron beam, it would be expected that LMO would convert into the ring phase under very-high-dose conditions rather than the rock-salt phase that is observed.

The atomic structure of LMO, revealed during low-dose and medium-dose STEM imaging, and the Mn-valence and the distribution of the atomic ratio of oxygen obtained by high-dose EELS correlate well with a Mn_3O_4 surface phase, a $Li_{1+x}[Mn_2]O_4$ subsurface region and bulk $Li[Mn_2]O_4$. These results, coupled with the deliberate damaging of LMO, which led to a rock-salt phase, suggest that the Mn_3O_4 and $Li_{1+x}[Mn_2]O_4$ phases observed are a result of stabilized LMO surfaces and not a forced reconstruction due to an effect of the electron beam.

Research on surface structural changes in cathodes using advanced electron microscopy techniques has been performed previously[40,41], but that work was focused on the restructuring of layered cathodes after cycling. In fact, a surface Mn_3O_4 phase has been reported in LMO[42,43], but those works also indicate phase formation after cycling. In those cases the cathodes were cycled to above 4.1 V to as high as 5.1 V versus Li^0. Overcharging of LMO induces the evolution of O_2 from the particle's surface. Since Mn^{4+} cannot be oxidized to Mn^{5+} in LMO, holes are introduced into the O-2p bands. These surface peroxide ions condense and O_2 is evolved from the material. By electrochemically evolving oxygen, the amount of Mn_3O_4 phase observed at the surface of LMO would be much thicker than the surface layer observed in our uncycled material.

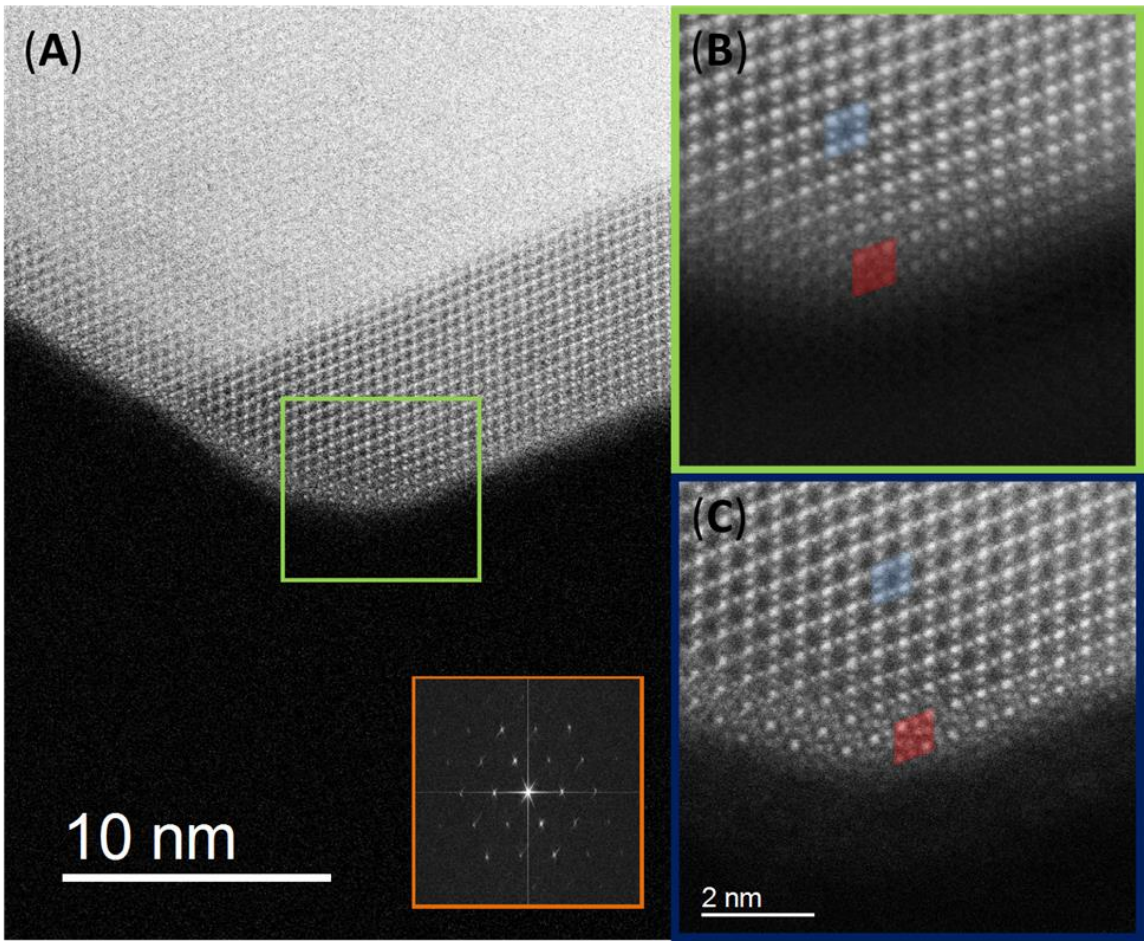

Figure 3-7: (A) Low-dose (2.6 x 10^3 $e^-/Å^2$) HAADF STEM image of LMO. Inset green square designates the area shown in 10B. Inset orange square borders a reduced FFT of 10A indicating crystallinity. (B) Fourier-filtered image taken from 10A and magnified showing the presence of both the LMO diamond (blue) and the Mn_3O_4 ring phase (red). (C) Higher magnification of the same surface indicated in 10A and 10B showing greater detail at the expense of a higher dose (5.3 x 10^4 $e^-/Å^2$). The structure is stable and does not change even under higher-dose conditions.

Indeed, Tang et al.[42,43] observed thick regions of Mn_3O_4 in their electrochemically cycled material.

Although both $Mn^{2+}[Mn_2^{3+}]O_4$ and $Li_2[Mn_2^{3+}]O_4$ have a sufficient concentration of Mn^{3+} to give a cooperative Jahn-Teller distortion to tetragonal c/a > 1 in the bulk

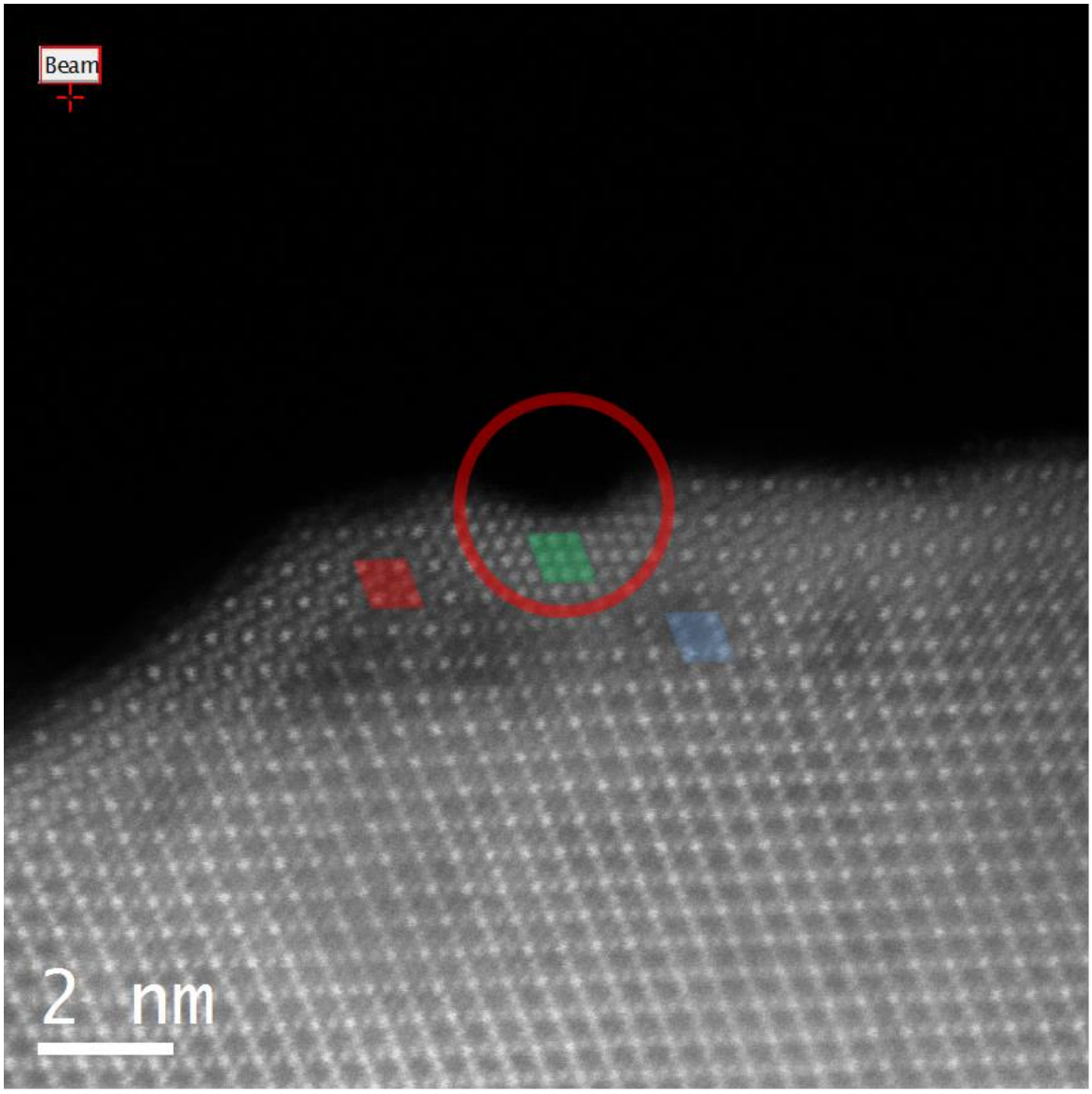

Figure 3-8: HAADF STEM image of LMO after irradiating the near surface with a very high electron dose (1.5×10^9 $e^-/Å^2$) from an EELS line scan. The red circle demarcates the area of the sample damaged by the electron beam. Both the Mn_3O_4 ring phase and LMO phase are transformed into a previously-unobserved rock-salt phase (green). This result suggests that the Mn_3O_4 and $Li_{1+x}[Mn_2]O_4$ phases observed are a result of stabilized LMO surfaces and not forced reconstruction due to an effect of the electron beam.

phases, our images provide no evidence of a distortion from cubic symmetry for either phase. We presume the 2D character of these phases bonded to a cubic bulk phase prevents a room-temperature cooperative Jahn-Teller distortion.

There is an interesting and significant implication that arises given this surface reconstruction in LMO. The Mn_3O_4 surface phase contains Mn in tetrahedral and octahedral sites, but the cathode is able to shuttle Li^+ into and out of the bulk during cycling despite the apparent Mn blockage. Perhaps Li is inserted into and out of Mn_3O_4 by a rock-salt conversion[3] that should increase the activation energy for Li transport between the bulk and the electrolyte.

3.5 CONCLUSIONS

We have studied the surface reconstruction of $Li[Mn_2]O_4$ by aberration-corrected scanning transmission electron microscopy. The atomic structure provided by HAADF STEM coupled with Mn-valence and the distribution of the atomic ratio of oxygen obtained by EELS reveals a thin, stable surface layer of Mn_3O_4, a subsurface region of $Li_{1+x}[Mn_2]O_4$ with retention of bulk $Li[Mn_2]O_4$. This observation is compatible with the disproportionation reaction of Mn coupled with oxygen deficiency and a displacement of surface Li^+ from the Mn_3O_4 surface phase to a subsurface layer.

Chapter 4: Effect of Chemical Treatment on the Surface Structure of $Li_{1-x}Mn_2O_4$

$Li[Mn_2]O_4$ (LMO) is a well-known cathode material for Li-ion batteries, but it is plagued with cyclability problems associated with the loss of Mn^{2+} to the organic liquid electrolyte during electrochemical cycling. The surface disproportionation of Mn ($2Mn^{3+} \rightarrow Mn^{2+} + Mn^{4+}$) creates the Mn^{2+} and leads to a stabilization of the surface of LMO through a surface reconstruction that creates a thin surface layer of Mn_3O_4 and a Li-rich subsurface layer of $Li_{1+x}[Mn_2]O_4$. We have applied an aqueous acid treatment, a non-aqueous chemical delithiation, and an oxygen plasma treatment to LMO in order to understand how this surface reconstruction is affected by chemical treatments. We find that Mn_3O_4 is a robust surface phase in the $Li_{1-x}[Mn_2]O_4$ system regardless of the chemical treatment and level of lithiation. The surface Mn_3O_4 phase is cubic whereas bulk Mn_3O_4 undergoes a cooperative Jahn-Teller distortion to tetragonal symmetry. Thicker Mn_3O_4 surface layers are tetragonal.

4.1 INTRODUCTION

$Li[Mn_2]O_4$ is a promising cathode material for Li-ion batteries due to its high rate capabilities and moderate capacity associated with its cubic spinel framework, which allows three dimensional Li^+ diffusion. However, it is also plagued with cyclability problems associated with dissolution of Mn^{2+} to the organic liquid electrolyte[44,45]; Mn^{2+} is created due to the surface disproportionation reaction $2Mn^{3+} \rightarrow Mn^{2+} + Mn^{4+}$. The disproportionation of Mn leads to a stabilization of LMO's surface, but how the surface stabilizes has been the topic of numerous studies[38,46,47]. Recently, we have revealed a surface reconstruction in LMO in which a thin Mn_3O_4 surface layer and a Li-rich subsurface layer is formed in a pre-cycled cathode material[48]. Mn_3O_4 is created by the

migration of Mn^{2+} to tetrahedral sites, which displaces the native Li^{+} to previously-unoccupied octahedral sites below the surface to maintain stoichiometry. The result is a surface reconstruction that creates both a Mn-rich surface spinel phase (Mn_3O_4) and a Li-rich subsurface spinel phase ($Li_{1+x}[Mn_2]O_4$) that share a common spinel framework with LMO. To understand the stability of the surface reconstruction of LMO with different chemical environments, we have applied an aqueous acid treatment[16], a non-aqueous chemical delithiation[17], and an oxygen plasma treatment to LMO. Subsequently, we have studied the effect of these treatments on the surface structure and surface chemistry.

4.2 EXPERIMENTAL METHODS

4.2.1 Material Synthesis

Two distinct LMO samples were used in this study; one was created with the synthesis procedure of a previous study[48] (synthesized sample) and the other was purchased from the MTI Corporation P/N: EQ-Lib-LMO (commercial sample). See section 2.1 Material Synthesis for the synthesis procedure.

4.2.2 Chemical Treatments

See section 2.2 Material Treatments for chemical treatments of $LiMn_2O_4$.

4.2.3 Materials Characterization

Samples were analyzed with a combination of scanning transmission electron microscopy (STEM) and powder X-ray diffraction (XRD). High-angle annular dark-field (HAADF) STEM images were taken on either a JEOL ARM200F TEM or a FEI Titan Themis TEM with 200 kV acceleration voltage and a convergence angle between 21 and 30 mrad. Electron energy loss spectroscopy (EELS) spectra were collected solely on the FEI Titan Themis TEM at 200 kV acceleration voltage with a convergence angle of 21

mrad. Each STEM image and EELS spectrum image indicates the microscope used, the dose rate, the total dose for the image, and a geometric factor (GF). The geometric factor is an approximation of the electron probe overlap when scanning at high magnifications. It is included as a multiple in the dose calculation. If no such probe overlap exists, the geometric factor is 1. A probe diameter of ~1.0 Å is assumed in all calculations for dose rate and total dose. All STEM images and EELS data were collected under high-vacuum conditions (< 1 x 10^{-7} Torr). Principal component analysis (PCA) and blind source separation (independent component analysis, ICA) using the CuBICA algorithm were applied to the EELS spectrum images with Hyperspy[33]. Mn oxidation states were determined by a comparison with established spectra[37,48] (Figure 4-1). STEM simulations (section 2.3.2.2 STEM Simulations) were used for phase identification. Mn_3O_4 phases were identified as cubic or tetragonal by comparing direct measurements of the STEM images with ideal structures. XRD spectra were obtained on a Rigaku MiniFlex diffractometer with Cu Kα radiation over a 2θ range between 10 and 90° with a step size of 0.02°. XRD spectra were analyzed with Rietveld refinement with PDXL-2 software.

4.3 RESULTS

4.3.1 Acid Treatment

Figure 4-2 compares typical morphologies, particle sizes, and surface structures of commercial and synthesized LMO samples before acid treatment. A thin layer of cubic Mn_3O_4 exists at the surface of both LMO samples (Figures 4-2B and 4-2D) despite the fact that the samples were made with different synthesis methods and that there is a particle size disparity between the samples (note the scale bars in Figures 4-2A and 4-2C). No porosity exists in the original samples. Initial elemental composition of

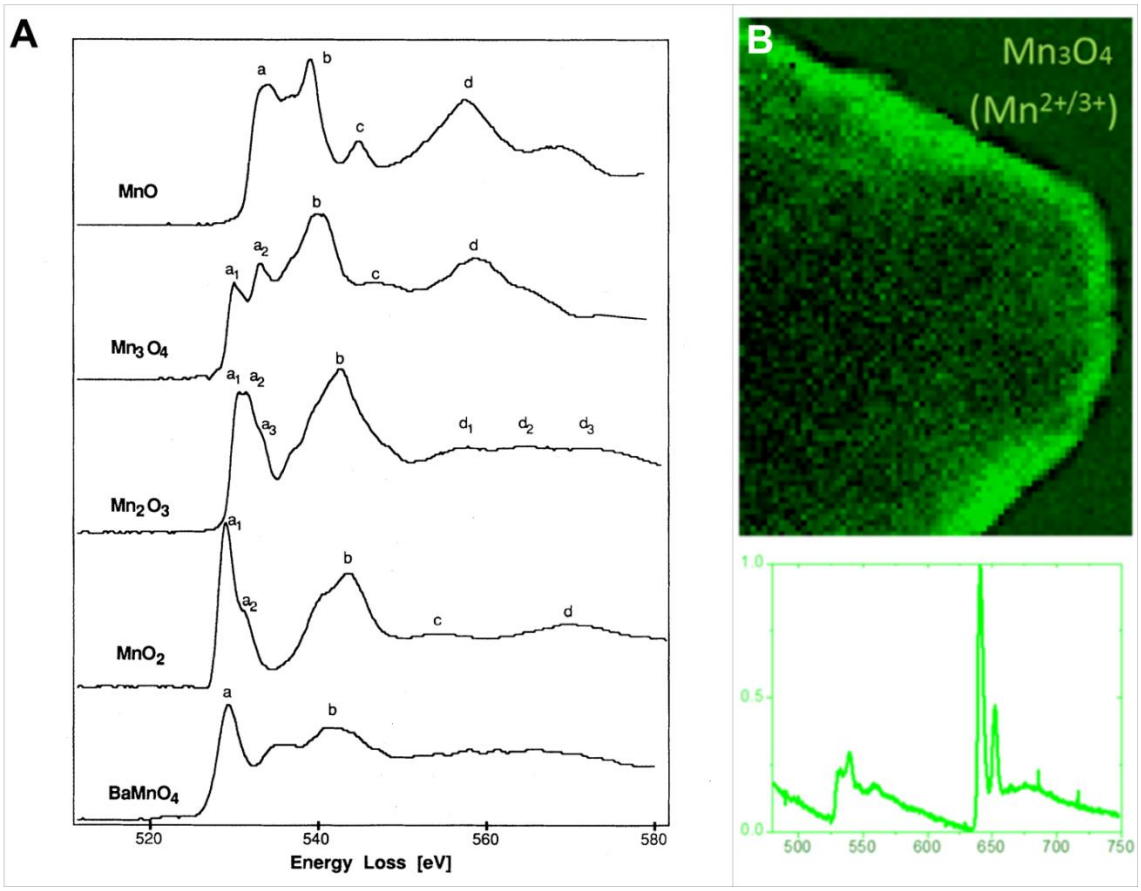

Figure 4-1: (A) Reprinted Figure 2 with permission from [Kurata, H., Colliex, C., *Phys. Rev. B. 48*, 2102-2108, **1993**] Copyright 2017 by the American Physical Society. http://dx.doi.org/10.1103/PhysRevB.48.2102. The figure shows oxygen k-edge spectra from different Mn oxides obtained by Kurata[37] (left). (B) Spectrum image map (right) taken from our previous work[48] indicating a surface composed of Mn_3O_4 and corresponding EEL spectrum (right, bottom) consistent with Kurata.

synthesized LMO ranges from 3.67 to 3.81 wt. % Li and 54.2 to 57.4 wt. % Mn as obtained with inductively coupled plasma optical emission spectrometry (ICP-OES). Commercial LMO contains 4.39 wt. % Li and 58.1 wt. % Mn. After acid treatment, synthesized LMO loses a significant amount of Li, the extent of which depends on the final pH of the solution. ICP-OES indicates acid-treated synthesized LMO contains 0.107 wt. % Li and 59.2 wt. % Mn at a final solution pH of 2.3 and < 0.065 wt. % Li and 58.6

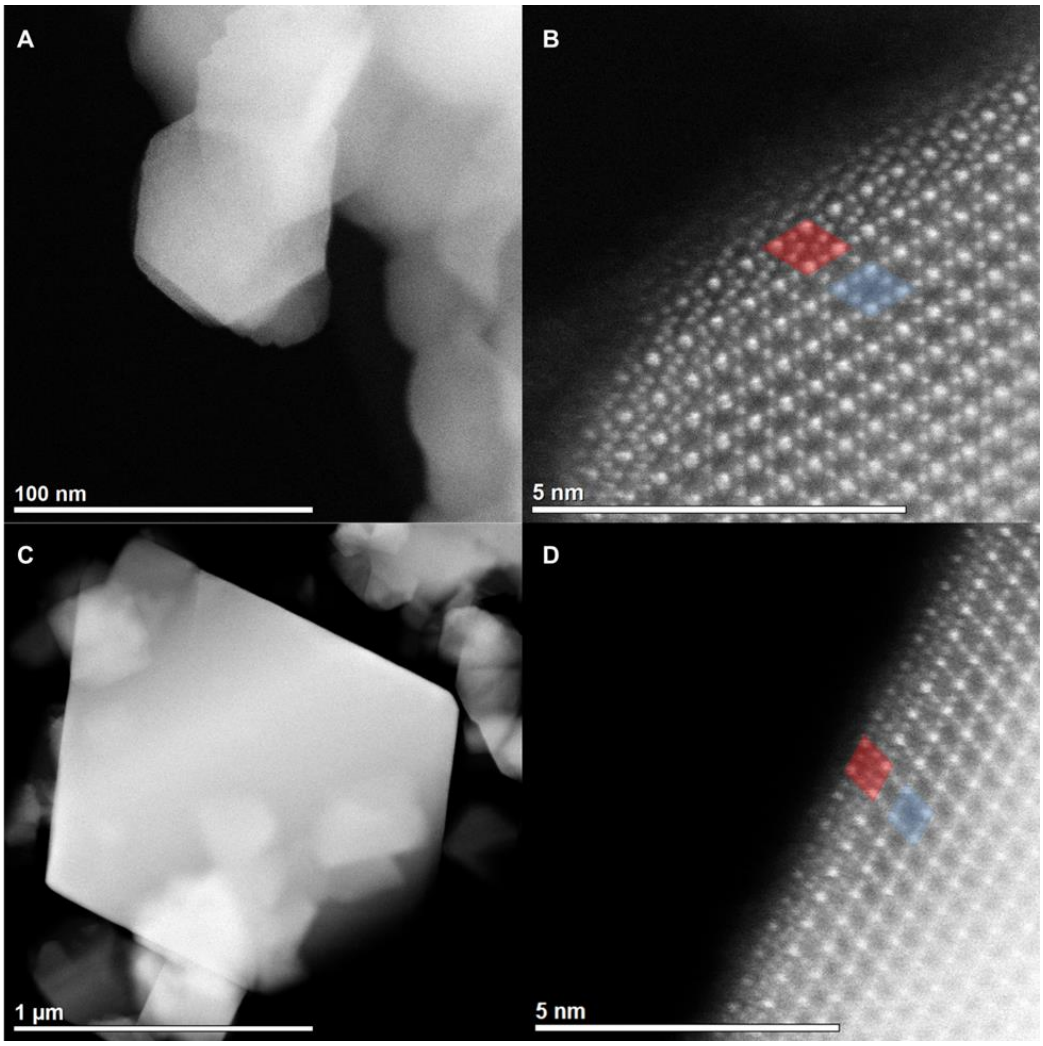

Figure 4-2: (A) Low-resolution HAADF STEM image of LMO indicating morphology of the untreated original powder (ARM200F, Dose Rate: 1.0 x 10^8 $e^-/Å^2 \cdot s$, Dose: 3.2 x 10^3 $e^-/Å^2$, GF: 1). Crystallites are on the order of ~10s of nm and no porosity exists. (B) High-resolution HAADF STEM image of the original LMO sample that shows the bulk spinel framework of LMO (blue) as well as the reconstructed surface of Mn_3O_4 (red) (ARM200F, Dose Rate: 1.0 x 10^8 $e^-/Å^2 \cdot s$, Dose: 5.5 x 10^5 $e^-/Å^2$, GF: 170). (C) Low-resolution HAADF STEM image of commercial LMO powder (ARM200F, Dose Rate: 1.8 x 10^8 $e^-/Å^2 \cdot s$, Dose: 5.7 x 10^3 $e^-/Å^2$, GF: 1). Crystallites are on the order of ~100s of nm to microns. The crystallites are characterized by well-defined crystal facets. (D) High-resolution HAADF STEM image of commercial LMO that shows a thin layer of Mn_3O_4 (red) at the surface of the bulk spinel structure (blue) (ARM200F, Dose Rate: 1.8 x 10^8 $e^-/Å^2 \cdot s$, Dose: 1.6 x 10^5 $e^-/Å^2$, GF: 27).

wt. % Mn at a final solution pH of 0.6. ICP-OES of acid-treated commercial LMO indicated a similar decrease in Li content; 0.875 wt. % Li and 59.8 wt. % Mn at a final solution pH of 0.3. XRD indicates that the unit-cell parameter of commercial LMO powder shrinks from 8.237 Å to 8.058 Å after acid treatment (Figure 4-3A). Similarly, the unit-cell parameter of synthesized LMO shrinks from 8.233 Å to 8.044 Å after acid treatment (Figure 4-3B). Synthesized LMO has a smaller crystallite size than commercial LMO as indicated by peak-broadening in the XRD spectra (Figure 4-3). Along with a reduction of Li, acid treatment changes the morphology of commercial and synthesized LMO, but in different ways (Figure 4-4). Compared to untreated synthesized LMO, there is a significant change in morphology of the acid-treated synthesized LMO sample (Figures 4-4A and 4-4B) as revealed with HAADF STEM. Individual nanoparticles of untreated synthesized LMO are transformed into porous crystallites after acid-treatment. On the other hand, commercial LMO powder, which is shown to contain larger crystallites, does not form a porous structure after acid treatment; HAADF STEM images show that the facets become irregular (Figure 4-4C) with thicker regions of cubic Mn_3O_4 at the surface and the original spinel framework in the bulk (Figure 4-4D). EELS of acid-treated synthesized LMO (Figure 4-5) reveals a uniform distribution of $Mn^{2+/3+}$ oxidation states consistent with the Mn_3O_4 phase with a small contribution of Mn^{4+} that could not be separated with independent component analysis. EELS of acid-treated commercial LMO (Figure 4-6) shows that the bulk of the material is Mn^{4+} with a more reduced surface containing $Mn^{2+/3+}$ indicating Mn_3O_4. Also, a color change is observed from black in the original LMO powder to rust brown in the acid-treated synthesized powder (Figure 4-7A and 4-7B, respectively). In contrast, the commercial LMO powder color changed from black to purple/dark-brown after acid treatment (Figure 4-7C and 4-7D, respectively).

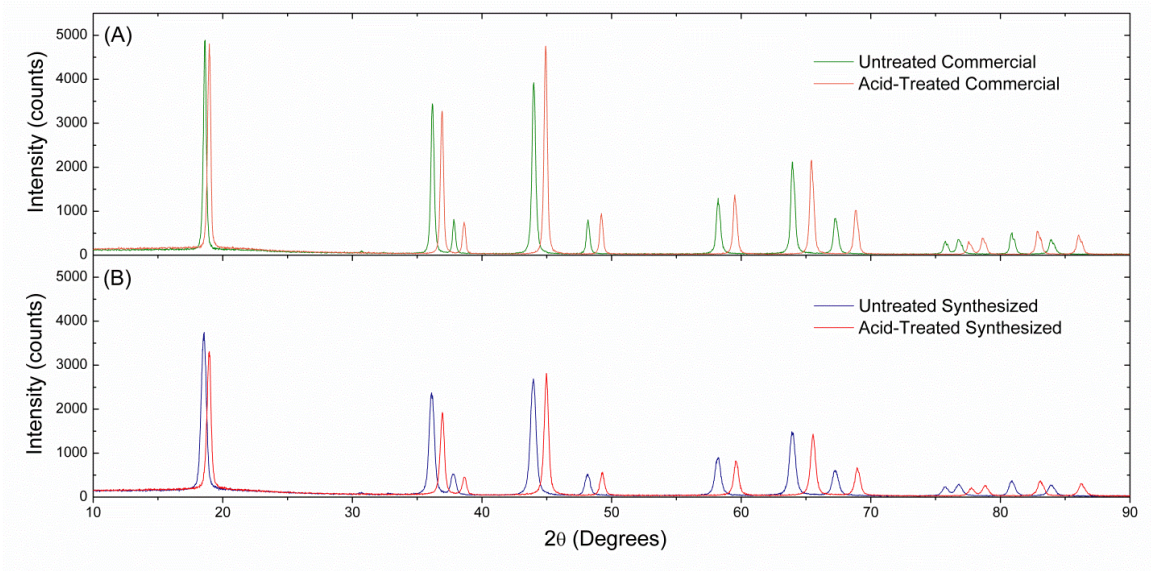

Figure 4-3: (A) XRD patterns comparing untreated commercial and acid-treated commercial LMO. Commercial LMO has a lattice parameter of 8.237 Å with sharp intensity peaks indicating large crystallites. After acid treatment, the lattice parameter of the commercial sample shrinks to 8.058 Å. (B) XRD patterns comparing untreated synthesized and acid-treated synthesized LMO. Synthesized LMO has a lattice parameter of 8.233 Å with broader intensity peaks that indicate smaller crystallite size. After acid treatment, the lattice parameter of the synthesized sample shrinks to 8.044 Å.

4.3.2 Chemical Delithiation Treatment

ICP-OES indicated that the chemically-delithiated LMO sample had 0.561 wt.% Li and 58.4 wt.% Mn, indicating a significant loss of Li from the spinel framework. Figure 4-8A shows the morphology of the chemically-delithiated LMO sample, which indicates significant porosity; however, the overall shape of the particles remains intact. The porosity does not hinder the ability to image chemically-delithiated LMO with HAADF STEM, unlike acid-treated synthesized LMO. Also, the sample is not as sensitive to defocus as was the case for acid-treated synthesized LMO, which indicates better retention of material and less porosity. A color change of the powder was not observed after chemical delithiation; the material retained the black color of the LMO

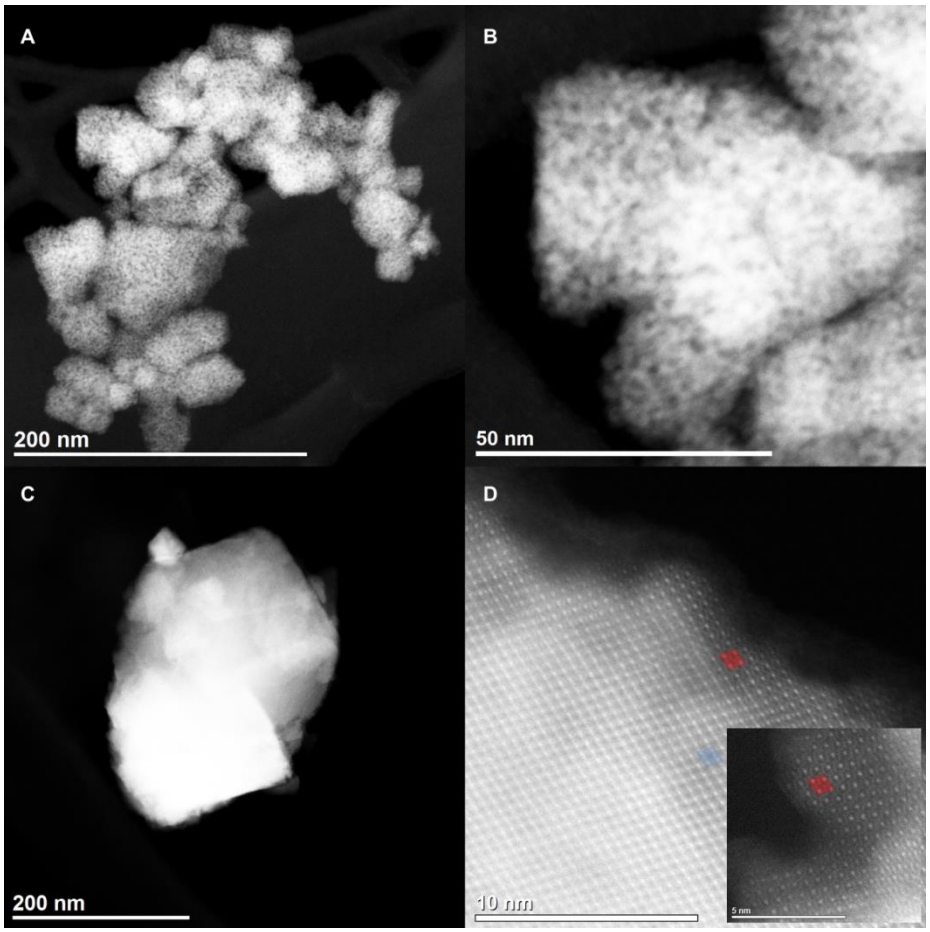

Figure 4-4: (A) Low-resolution HAADF STEM image of acid-treated synthesized LMO powder (Titan, Dose Rate: 4.0 x 10^8 $e^-/Å^2$·s, Dose: 8.7 x 10^3 $e^-/Å^2$, GF: 1). The sample exhibits significant porosity when compared to the original sample (Figure 4-2A). (B) Higher-resolution HAADF STEM image of acid-treated synthesized LMO showing the extent of the porosity (Titan, Dose Rate: 4.0 x 10^8 $e^-/Å^2$·s, Dose: 1.2 x 10^4 $e^-/Å^2$, GF: 1). Acid-treated synthesized LMO is very sensitive to defocus indicating a lack of well-defined surfaces, which presents as a "blurry" image. (C) Low-resolution HAADF STEM image of acid-treated commercial LMO powder (ARM200F, Dose Rate: 1.8 x 10^8 $e^-/Å^2$·s, Dose: 5.7 x 10^3 $e^-/Å_2$, GF: 1). The crystallite surfaces are rough and irregular. (D) High-resolution HAADF STEM image of acid-treated commercial LMO that indicates thick regions of Mn_3O_4 (red) at the surface of the bulk spinel structure (blue) (ARM200F, Dose Rate: 1.8 x 10^8 $e^-/Å^2$·s, Dose: 1.1 x 10^5 $e^-/Å^2$, GF: 20). Inset image of a different area of the particle better illustrates the increase in thickness of the Mn_3O_4 surface phase (red) (ARM200F, Dose Rate: 1.8 x 10^8 $e^-/Å^2$·s, Dose: 1.6 x 10^5 $e^-/Å^2$, GF: 27).

powder. HAADF STEM of chemically-delithiated LMO (Figure 4-8B) reveals the bulk spinel framework with a cubic Mn_3O_4 surface phase as was observed in the original LMO sample. However, there is an additional rock-salt phase observed in the chemically delithiated LMO sample that lies between the Mn_3O_4 surface phase and the bulk spinel framework. EELS of chemically-delithiated LMO (Figure 4-9) shows a uniform distribution of $Mn^{2+/3+}$ oxidation states consistent with the Mn_3O_4 phase, but with a significant contribution of Mn^{4+} that could not be separated with independent component analysis just as in the acid-treated synthesized LMO case. The contribution of Mn^{4+} to the EEL spectrum is more significant for chemically delithiated LMO than with acid-treated synthesized LMO.

4.3.3 Oxygen Plasma Treatment

HAADF STEM of an oxygen-plasma-treated LMO sample (Figure 4-10A) indicates that its morphology shows some porosity. When the oxygen-plasma-treated sample was viewed under high-magnification with HAADF STEM, it was observed that the portions of the surface that had been exposed to the oxygen plasma contained a thicker, tetragonal Mn_3O_4 phase (Figure 4-10B). XRD of the oxygen-plasma-treated LMO sample reveals a mixture of two phases consistent with $Li[Mn_2]O_4/\lambda\text{-}MnO_2$ and tetragonal Mn_3O_4 phases (Figure 4-11). The lattice parameter of the $Li[Mn_2]O_4/\lambda\text{-}MnO_2$ phase is 8.251 Å. The tetragonal Mn_3O_4 phase has a = 5.782 Å and c = 9.478 Å. EELS analysis of the oxygen-plasma-treated samples (Figure 4-12) indicated a Mn oxidation state of 4+ in the bulk, characteristic of $\lambda\text{-}MnO_2$, and mixed 2+/3+ at the surface indicative of Mn_3O_4. Also, a color change of the oxygen-plasma-treated LMO powder from black in the original LMO sample to a brown-colored powder was observed (Figure 4-13).

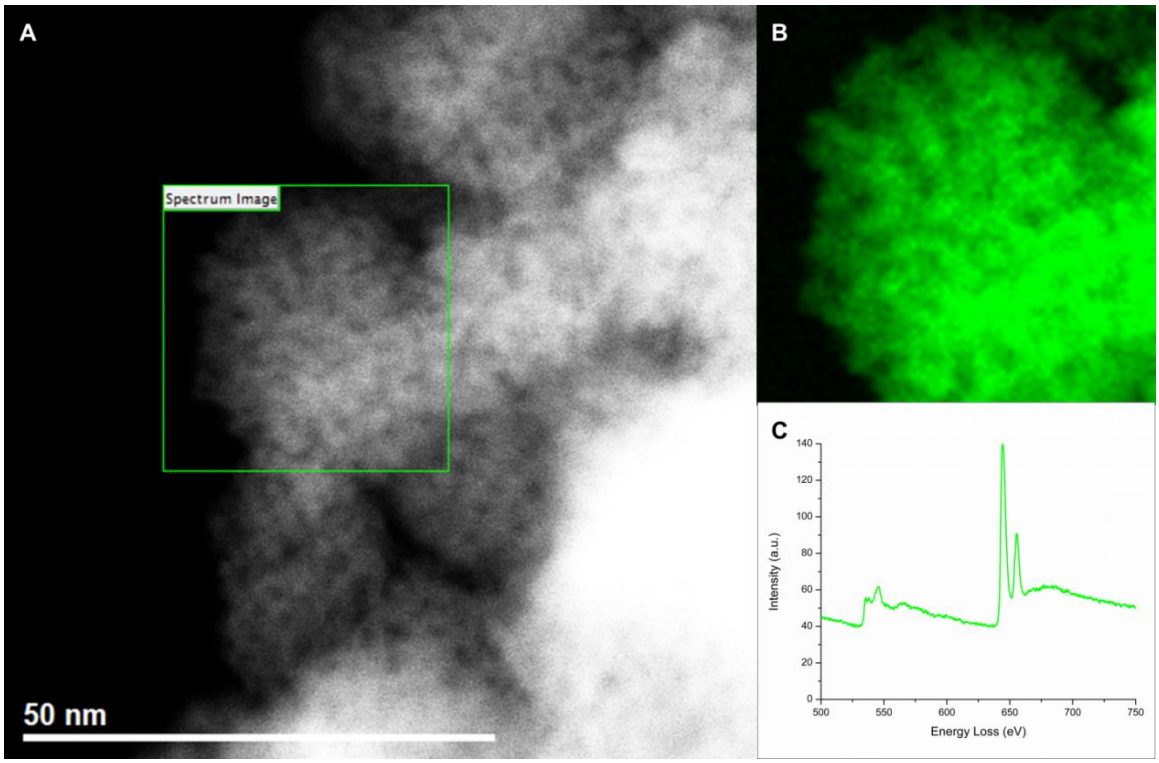

Figure 4-5: (A) Low-resolution HAADF STEM image of acid-treated synthesized LMO. The green square indicates the region of interest that was scanned with the EELS probe (Titan, Dose Rate: 1.2 x 10^9 $e^-/Å^2 \cdot s$, Dose: 6.2 x 10^7 $e^-/Å^2$, GF: 1). (B) EEL spectrum-image map comprised of (C) the only EEL spectrum found with independent component analysis. The EEL spectrum reveals a uniform distribution of $Mn^{2+/3+}$ oxidation states consistent with the Mn_3O_4 phase with a small contribution of Mn^{4+} that could not be separated with independent component analysis.

4.4 DISCUSSION

Thackeray et al. have described the mechanism observed by Hunter for the removal of Li^+ and Mn^{2+} from the LMO structure in an acidic environment[34]. That mechanism is described by the following surface reaction:

$$2Li[Mn_2]O_4 + 4H^+ (l) \rightarrow 2Li^+ (l) + Mn^{2+} (l) + 2H_2O (l) + 3\lambda\text{-}MnO_2$$

Room-temperature Li-ion mobility, surface disproportionation of Mn ($Mn_b^{3+} + Mn_s^{3+} \rightarrow Mn_b^{4+} + Mn_s^{2+}$, where b is bulk and s is surface), protons, and bound surface

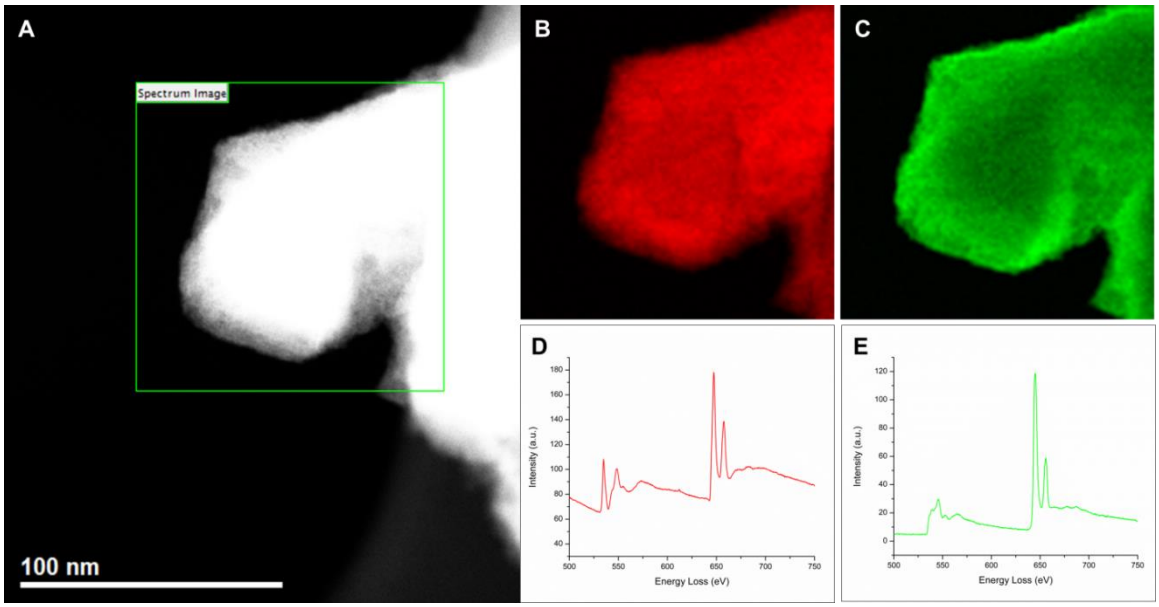

Figure 4-6: (A) Low-resolution HAADF STEM image of acid-treated commercial LMO. The green square indicates the region of interest that was scanned with an EELS probe (Titan, Dose Rate: 1.3 x 10^9 $e^-/Å^2$·s, Dose: 6.3 x 10^7 $e^-/Å^2$, GF: 1). (B) EEL spectrum-image map comprised of (D) the Mn^{4+} EEL spectrum found with independent component analysis. The bulk of the particle contains Mn^{4+} indicative of λ-MnO_2. (C) An EEL spectrum-image map comprised of (E) the only other phase found with independent component analysis; a $Mn^{2+/3+}$ EEL spectrum characteristic of Mn_3O_4.

water are all required for this reaction to proceed forward. Li^+, Mn^{2+}, and oxygen in the form of water are removed from LMO in order to produce λ-MnO_2. ICP-OES and lattice parameters confirm that the acid treatment does indeed remove a significant amount of Li from both synthesized and commercial samples and XRD of the powders shows that the $[Mn_2]O_4$ spinel framework remains intact (Figure 4-3) in both samples. Hunter indicated that complete conversion of LMO to λ-MnO_2 does not occur until the solution pH reaches a value below 2.5. In our observations, complete conversion of acid-treated synthesized LMO does not occur until the solution reaches a pH as low as 0.6. In comparison, acid-treated commercial LMO never achieves complete delithiation even at a lower pH value of 0.3, likely due to the lower available surface area for the above reaction to occur.

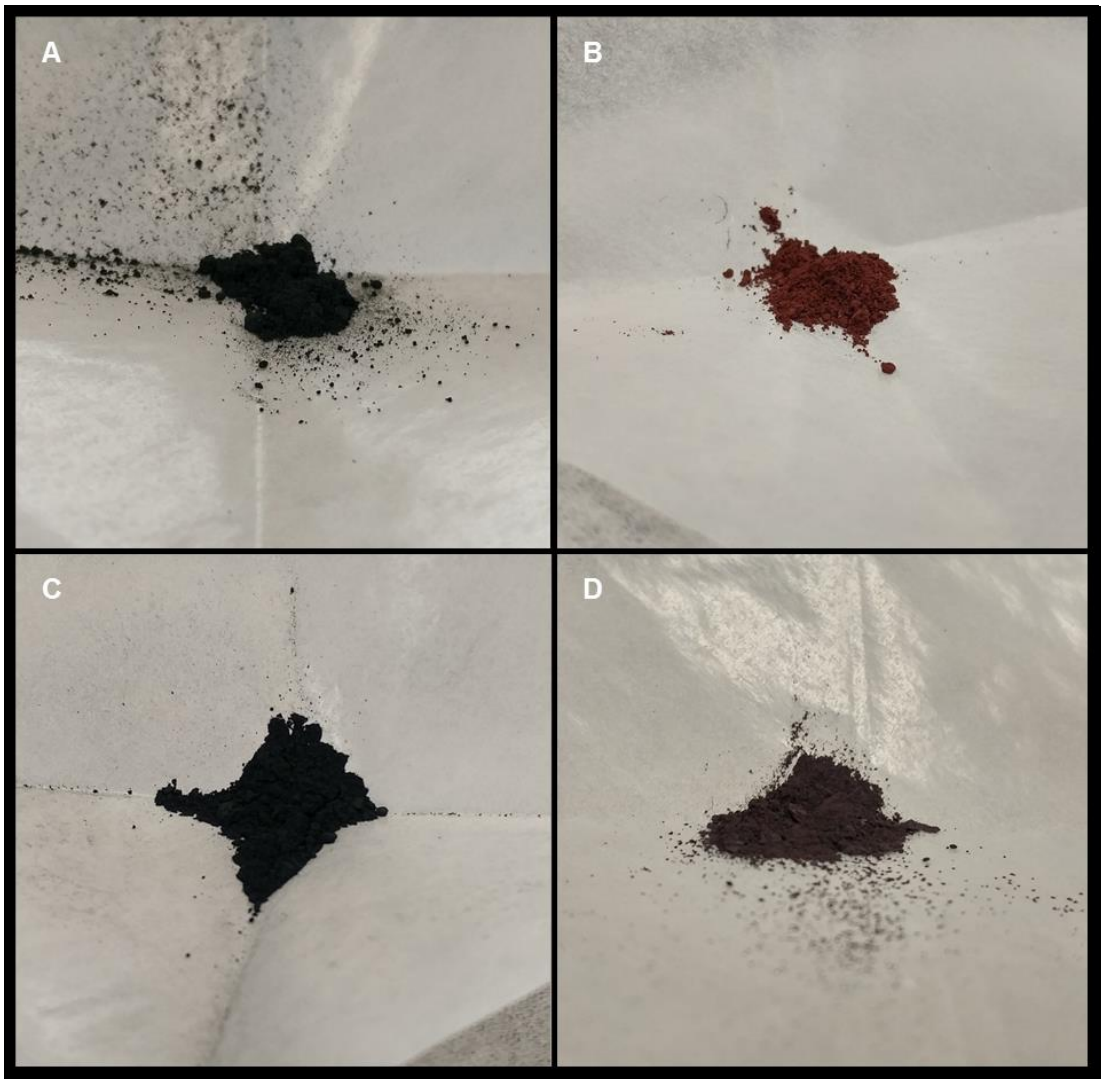

Figure 4-7: (A) Image of untreated synthesized LMO powder indicating a black color. (B) Image of acid-treated synthesized LMO powder indicating a rust-brown color, which is inconsistent with the black to blue-black color observed by Hunter[16]. (C) Image of untreated commercial LMO powder indicating a black color. (D) Image of acid-treated commercial LMO powder indicating a purple/dark brown color, which more closely approximates the observations of Hunter. The only difference between the two initial powders is the crystallite size. Acid treatment leads to high porosity and high surface area in the synthesized powder case and therefore a large amount of Mn_3O_4 surface phase consistent with the rust-brown color. Acid treatment leads to thicker Mn_3O_4 surface phases in the commercial powder case, but has little effect on the surface area leaving the material to retain most of its black color with some contribution from the thicker Mn_3O_4 surface phase.

The significant loss of material from LMO is evident after acid treatment (Figure 4-4) and in agreement with the observations made by Hunter, although the microstructure changes more drastically for the synthesized LMO sample than for the commercial LMO sample. Several attempts to image acid-treated synthesized LMO with HAADF STEM failed due to the severely porous nature of the crystallites. The larger crystallite size found in the commercial LMO powder allows for HAADF STEM characterization, which reveals large crystallites with well-defined surfaces at low magnification (Figure 4-2C) and thin layers of cubic Mn_3O_4 at the surface of the crystals at high magnification (Figure 4-2D) before acid treatment. After acid treatment, the commercial LMO crystallites gain an irregular surface characterized by thicker regions of cubic Mn_3O_4 (Figure 4-4C and 4-4D) with the preservation of the $[Mn_2]O_4$ spinel framework. EELS of acid-treated commercial LMO (Figure 4-6) shows that the bulk of the material contains Mn^{4+} with a more reduced surface containing $Mn^{2+/3+}$, which is consistent with Mn_3O_4. Surface reconstruction to a cubic Mn_3O_4 phase occurs in acid-treated commercial LMO despite the fact that a significant amount of Li and some Mn, including the initial cubic Mn_3O_4 surface layer, were removed from the spinel framework indicating the inherent stability of Mn_3O_4 as a surface layer in the $Li_{1-x}[Mn_2]O_4$ system. Acid-treated synthesized LMO exhibits a strikingly similar XRD pattern to that of its commercial analogue (Figure 4-3), but its morphology and color are quite different. Although the acid-treated commercial LMO sample loses some material, it maintains its general shape and displays a purple/dark-brown color (Figure 4-7D) similar to that observed by Hunter[16]. The acid-treated synthesized sample loses a significant amount bulk material relative to its nano size leading to its porosity. Since the only difference between the synthesized and commercial samples is the size of the crystallites, it is reasonable to expect that the same surface reconstruction to cubic Mn_3O_4 occurs along the significant surface of the acid-

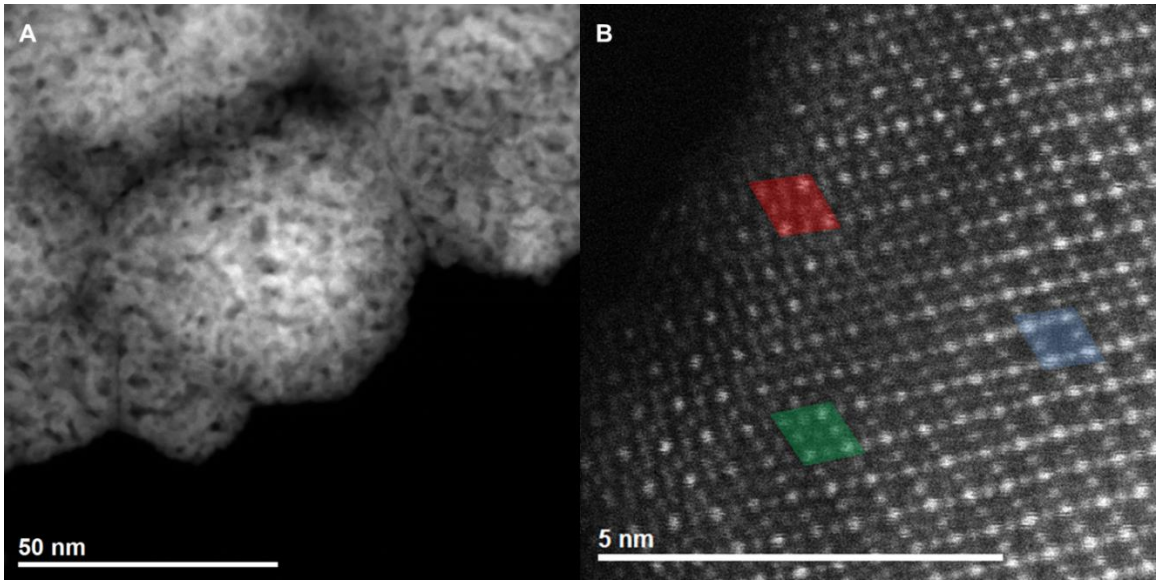

Figure 4-8: (A) Low-resolution HAADF STEM image of chemically-delithiated LMO powder indicating significant porosity (Titan, Dose Rate: 1.3 x 10^9 $e^-/Å^2$·s, Dose: 4.9 x 10^4 $e^-/Å^2$, GF: 1). (B) High-resolution HAADF STEM image of chemically delithiated LMO that confirms the bulk spinel structure (blue) as well as the surface Mn_3O_4 phase (red) (ARM200F, Dose Rate: 1.0 x 10^8 $e^-/Å^2$·s, Dose: 1.3 x 10^5 $e^-/Å^2$, GF:40). An additional rock-salt phase (green) is observed subsurface between the Mn_3O_4 and bulk spinel phases. Chemical delithiation creates significant porosity; however, the overall shape of the particles remains intact. The sample is not as sensitive to defocus as was the case for acid-treated synthesized LMO, which indicates better retention of material and less porosity.

treated synthesized LMO sample. The porosity with significant, reconstructed surface would explain the vibrant rust-brown color of the sample (Figure 4-7B) and the EELS spectra (Figure 4-5), which reveals a uniform distribution of $Mn^{2+/3+}$ oxidation states also consistent with the Mn_3O_4 phase, but with a small contribution of Mn^{4+}. The EEL spectrum in Figure 4-5 correlates well with established spectra of Mn_3O_4 found in previous studies[37,48]; however, the spectrum contains a higher, first prepeak of the O-K edge, which places it higher than the second prepeak. This increase in relative intensity is due to a Mn^{4+} contribution (Figure 4-1A) that could not be separated from the Mn_3O_4

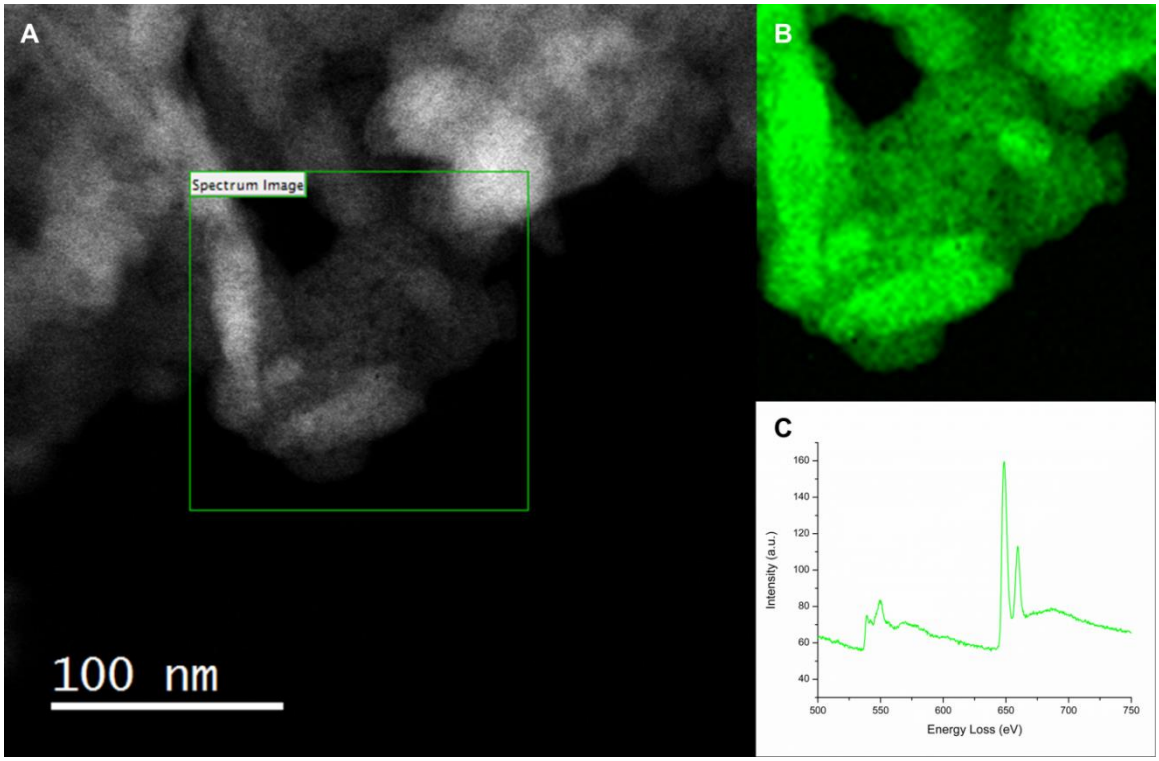

Figure 4-9: (A) Low-resolution HAADF STEM image of chemically-delithiated LMO. The green square indicates the region of interest that was scanned with an EELS probe (Titan, Dose Rate: 1.3 x 10^9 $e^-/Å^2$·s, Dose: 6.3 x 10^7 $e^-/Å^2$, GF: 1). (B) EEL spectrum-image map comprised of (C) the only EEL spectrum found with independent component analysis. EEL spectrum reveals a uniform distribution of $Mn^{2+/3+}$ oxidation states consistent with the Mn_3O_4 phase with a contribution of Mn^{4+} that could not be separated with independent component analysis. The contribution of Mn^{4+} to the EEL spectrum is more significant for chemically delithiated LMO than with acid-treated synthesized LMO. Mn^{4+} is consistent with the bulk spinel framework shown in Figure 4-8B and the loss of Li as indicated with ICP-OES.

spectrum with independent component analysis. Mn^{4+} is indicative of the underlying $[Mn_2]O_4$ spinel framework of λ-MnO_2, which is consistent with the results from XRD (Figure 4-3). Although a significant amount of the surface of acid-treated synthesized and acid-treated commercial LMO contain Mn_3O_4, no significant amount of Mn_3O_4 phase, cubic or tetragonal, is observed in either of their XRD spectra (Figure 4-3).

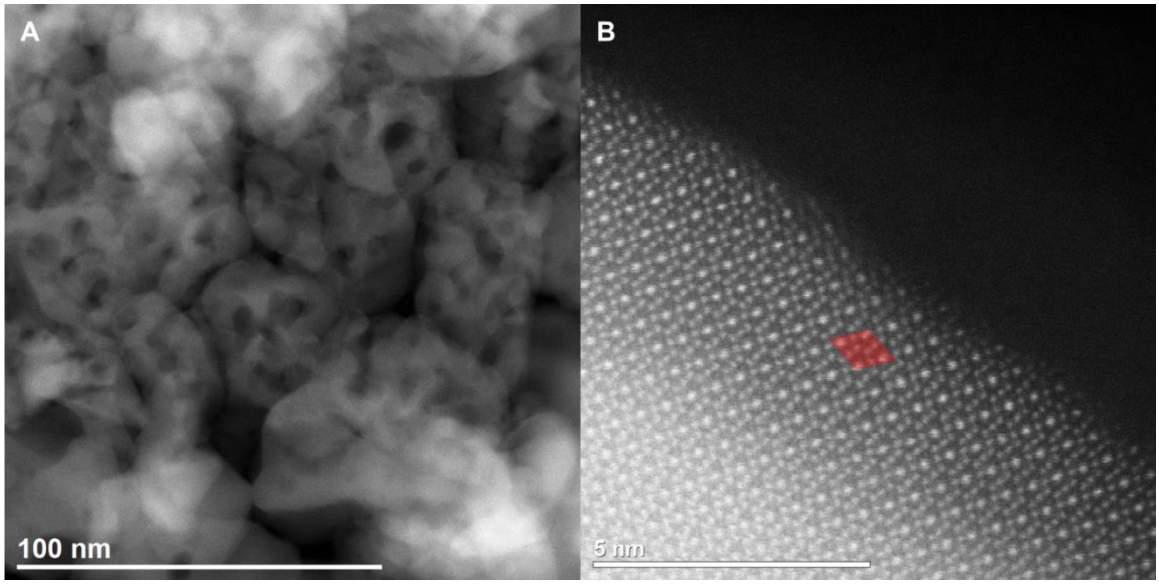

Figure 4-10: (A) Low-resolution HAADF STEM image of oxygen-plasma-treated LMO powder indicating a morphology similar to that of the original LMO sample with some porosity (Titan, Dose Rate: 4.0 x 10^8 $e^-/Å^2$·s, Dose: 8.7 x 10^3 $e^-/Å^2$, GF: 1). (B) High-resolution HAADF STEM image of oxygen-plasma-treated LMO showing a thick Mn_3O_4 surface phase (red), thicker than the one that occurs in untreated LMO (ARM200F, Dose Rate: 1.0 x 10^8 $e^-/Å^2$·s, Dose: 2.5 x 10^5 $e^-/Å^2$, GF: 79).

Chemical delithiation occurs in aprotic acetonitrile with NO_2BF_4 as an oxidizing agent according to the following reaction:

$$Li[Mn_2]O_4 + xNO_2BF_4 \rightarrow Li_{1-x}[Mn_2]O_4 + xNO_2 + xLiBF_4$$

This reaction achieves the removal of Li through a different mechanism than acid-treatment and it occurs in the absence of protons and water. Chemically-delithiated LMO has a Li:Mn ratio of 0.15:2.00 as compared to 1.05:2.00 in the original LMO sample indicating a significant loss of Li from the $[Mn_2]O_4$ spinel framework and therefore an average Mn oxidation state of 3.93+ within the bulk. HAADF STEM shows the bulk spinel framework and the Mn_3O_4 surface phase of the original sample remains intact, but it also reveals a subsurface rock-salt phase that is not present in untreated LMO samples

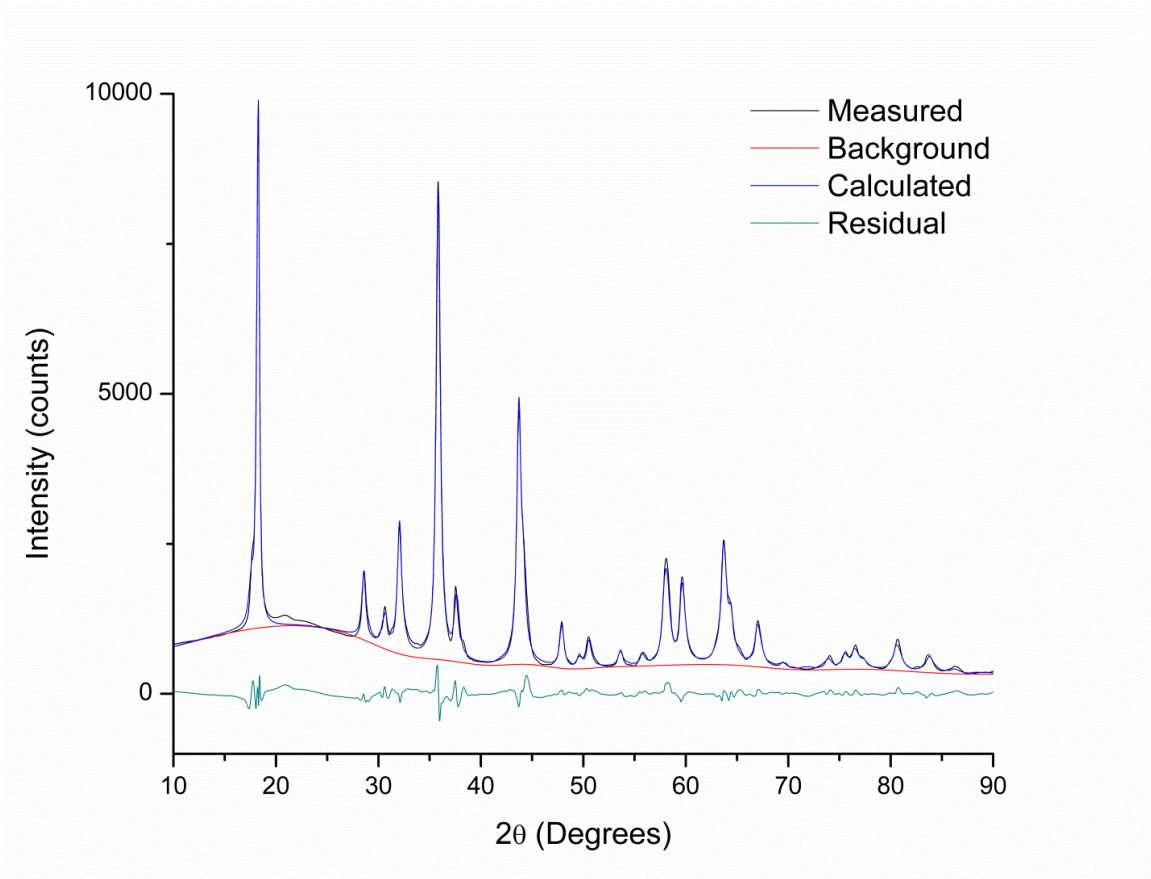

Figure 4-11: XRD pattern of oxygen-plasma-treated LMO. Two distinct phases are observed; cubic $Li[Mn_2]O_4/\lambda\text{-}MnO_2$ and tetragonal Mn_3O_4. The lattice parameter of the $Li[Mn_2]O_4/\lambda\text{-}MnO_2$ phase is 8.251 Å. The tetragonal Mn_3O_4 phase has a = 5.782 Å and c = 9.478 Å. Refinement: Rwp = 6.10 %, Rp = 4.85 %, Re = 3.21 %, S = 1.8959, $\chi 2$ = 3.5943.

(Figure 4-8B). HAADF STEM also indicates that porosity exists in the sample after chemical treatment (Figure 4-8A). The loss of material may be due to the high concentration gradients created when placing solid NO_2BF_4 into the LMO/acetonitrile solution leading to oxygen evolution from LMO due to strong local oxidative conditions or by contamination of the chemical treatment with water, which when reacted with NO_2BF_4, creates corrosive HF or HNO_3. EELS of chemically-delithiated LMO (Figure 4-9) shows a uniform distribution of $Mn^{2+/3+}$ oxidation states, which is consistent with

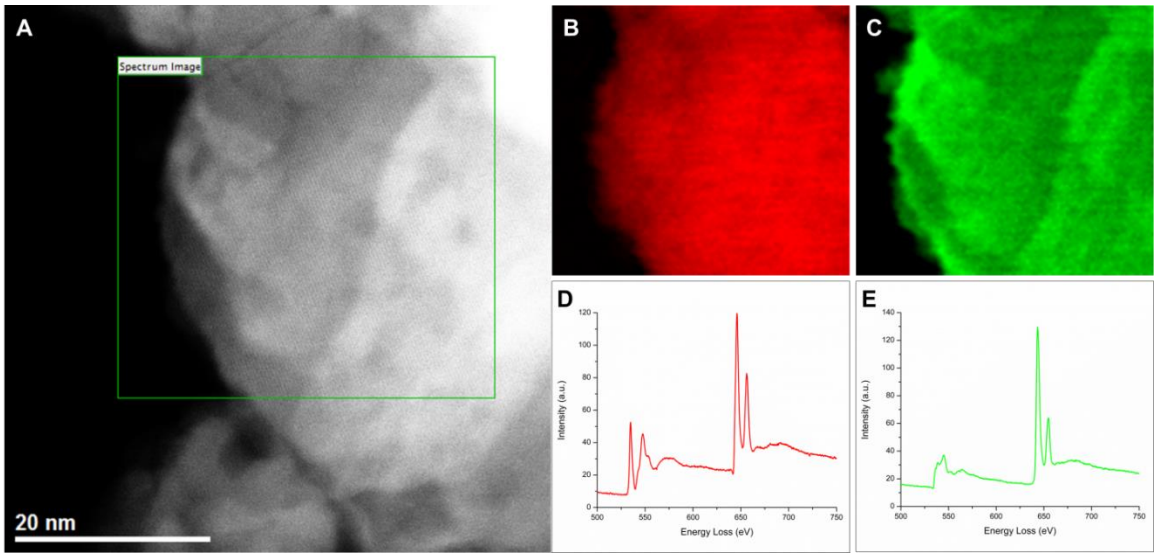

Figure 4-12: (A) Low-resolution HAADF STEM image of oxygen-plasma-treated LMO powder. The green square indicates the region of interest that was scanned with an EELS probe (Titan, Dose Rate: 8.8 x 10^8 $e^-/Å^2$·s, Dose: 4.4 x 10^7 $e^-/Å^2$, GF: 1). (B) EEL spectrum-image map comprised of (D) the Mn^{4+} EEL spectrum found with independent component analysis. This is the same spectrum observed in acid-treated commercial LMO (Figure 4-6B and 4-6D). The bulk of the particle contains Mn^{4+} indicative of λ-MnO_2. (C) An EEL spectrum-image map comprised of (E) the only other phase found with independent component analysis; a $Mn^{2+/3+}$ EEL spectrum characteristic of Mn_3O_4, which is consistent with a Mn_3O_4 surface phase as observed in Figure 10B. This is the same spectrum observed in acid-treated commercial LMO (Figure 4-6C and 4-6E).

established spectra of Mn_3O_4 found in previous studies[37,48] as well as with a Mn_3O_4 surface as shown with HAADF STEM (Figure 4-8B). A significant contribution of Mn^{4+} that could not be separated with independent component analysis is also observed in the EEL spectrum. This is similar to the acid-treated synthesized LMO case, except the contribution of Mn^{4+} to the EEL spectra is more significant. The EEL spectrum contains a high first prepeak of the O-K edge, higher than the second prepeak; much more so as compared to the acid-treated synthesized LMO case. This increase in relative intensity is due to a Mn^{4+} contribution (Figure 4-1A) that could not be separated from the Mn_3O_4

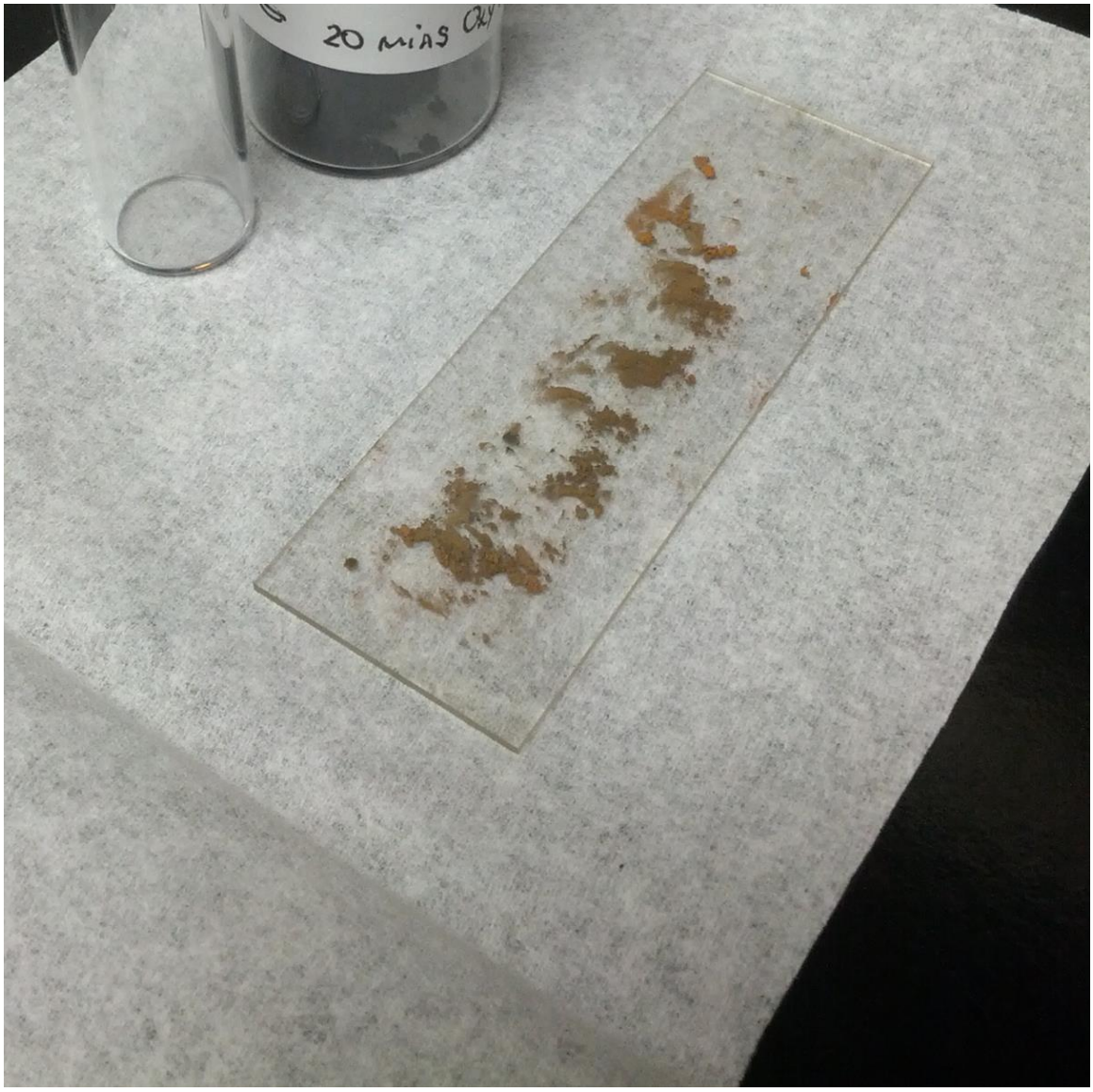

Figure 4-13: Image of oxygen-plasma-treated LMO showing a brown powder after oxygen plasma treatment. The original powder is black. The brown color is indicative of the creation of thick regions of Mn_3O_4 caused by the highly oxidizing nature of the oxygen plasma treatment removing Li from LMO and subsequently oxygen from the $[Mn_2]O_4$ spinel framework.

spectrum with independent component analysis. Mn^{4+} is indicative of a bulk $[Mn_2]O_4$ spinel framework without Li i.e. λ-MnO_2. The Mn_3O_4 surface phase has been proven to exist before chemical delithiation in our previous work[48], so its presence after delithiation

means that either the surface was shed during Li^+ removal and surface reconstruction occurs or that Li^+ diffused through the surface Mn_3O_4 layer. Considering the former case, the forceful removal of tetrahedral-site Mn^{2+} from Mn_3O_4 to the electrolyte would be required with or without accompanying oxygen in order for Li to diffuse through the surface from the bulk of LMO. This process would mean that active material is lost during each subsequent cycle of a Li-ion battery containing LMO as the cathode material. After the cathode is delithiated, the remaining $[Mn_2]O_4$ spinel framework would need to reconstruct to form a stable Mn_3O_4 surface layer. Considering the latter case, Thackeray et al. described how the insertion of Li into the Mn_3O_4 phase displaces the tetrahedral-site Mn^{2+} to an empty interstitial octahedral site of the spinel to form an ordered rock-salt structure $(Li_xMn_3O_4)$[3]. During charge, Li^+ from the bulk would induce a rock-salt transition of the surface Mn_3O_4 phase. Removal of the Li^+ from the surface rock-salt phase restores the Mn_3O_4 spinel phase with the return of the displaced Mn^{2+} to its tetrahedral site. In either case Mn_3O_4 is the resultant stable surface phase and perhaps a combination of both occur, but since the rock-salt phase is present subsurface to the stable Mn_3O_4 surface phase, it is reasonable to assume the latter case is more likely.

The oxygen plasma treatment employs the use of a non-equilibrium plasma, or cold plasma, that creates many reactive oxygen species that can oxidize samples without the need of high substrate temperatures[49,50]. Oxygen-plasma treatment of LMO allows oxidation of the LMO phase while keeping the Mn content relatively constant. In fact, oxygen plasma has been used to modify thin-film LMO cathodes, which resulted in better capacity retention during cycling, but the authors attributed the better cyclability to smoothing of the cathode surface rather than a structural or chemical modification of the surface[51]. Low-resolution HAADF STEM (Figure 4-10A) indicates that the morphology of the oxygen-plasma-treated sample does not change significantly from the original

LMO sample although some porosity exists, likely due to sputtering by the high-energy particles within the plasma. During oxidation of the LMO particles by the oxygen plasma, Li^+ is extracted to the surface along with electrons where they combine with freely available oxygen and is sputtered away from the material with the plasma. EELS analysis of the oxygen-plasma-treated samples (Figure 4-12) agrees with a Li-deficient bulk composed of Mn^{4+} (λ-MnO_2) and also reveals a surface of varying thickness composed of mixed $Mn^{2+/3+}$ indicative of Mn_3O_4. The distinct phases revealed with EELS are in direct agreement with the phases revealed during acid treatment of commercial LMO powder. High-resolution HAADF STEM shows that significant portions of the surface have been converted to tetragonal Mn_3O_4 (Figure 4-10B), which was confirmed with XRD (Figure 4-11). Rietveld refinement of the oxygen-plasma-treated LMO sample is consistent with a two-phase mixture of $Li[Mn_2]O_4/\lambda$-MnO_2 and tetragonal Mn_3O_4 (Figure 4-11). Thicker regions of Mn_3O_4 than are observed in the original LMO sample can only be due to an over-oxidation of the LMO particles. Once all of the Li^+ is extracted from LMO, the resultant λ-MnO_2 phase is subject to further oxidation, but since Mn^{4+} cannot be oxidized to Mn^{5+} in LMO, holes are introduced into the O-2p bands forming peroxide ions that condense at the surface and leave as oxygen molecules. The loss of oxygen leads to a reduction of λ-MnO_2 and the formation of thick regions of Mn_3O_4, which is consistent with the change in color of the powder from black to brown (Figure 4-13).

It is interesting that despite the widely varying chemical treatments, a stable layer of Mn_3O_4 is formed or maintained at the surface of each of these materials. Mn_3O_4 is stable at room-temperature as a normal spinel structure $Mn^{2+}[Mn_2^{3+}]O_4$ with a tetragonal distortion due to a cooperative Jahn-Teller effect of the Mn^{3+} ions, which does not disappear until it undergoes a reversible tetragonal-to-cubic transition at 1170°C[52]. It is

observed in this study that if the Mn_3O_4 layer is sufficiently thin, it is cubic. This effect has also been observed in another study[53]. As the Mn_3O_4 layer grows in thickness, as was the case for the oxygen-plasma-treated LMO sample, it gains sufficient Jahn-Teller cooperativity to undergo a cubic-to-tetragonal distortion. It is also interesting that the surface disproportionation of Mn ($Mn_b^{3+} + Mn_s^{3+} \rightarrow Mn_b^{4+} + Mn_s^{2+}$) occurs despite the different chemical environments or the amount of Li in the bulk. No matter the oxidation state of Mn in the bulk within the range 3.5+ to 4+ ($Mn^{3.5+}$ for LMO and Mn^{4+} for λ-MnO_2), the surface contains at least a thin, cubic Mn_3O_4 phase that will become tetragonal if the layer is thickened. The facile, reversible displacement of tetrahedral-site Mn^{2+} to an interstitial, octahedral site by Li^+ insertion/extraction allows bulk Li^+ ions to diffuse through a surface Mn_3O_4 layer. Retention of a surface Mn_3O_4 layer shows the stability of a surface Mn_3O_4 spinel phase and its presence indicates the disproportionation of Mn ($2Mn^{3+}$ to $Mn^{2+} + Mn^{4+}$) on the surface. Even the highly oxidizing nature of the oxygen plasma does not oxidize the native Mn_3O_4 surface layer to reduce the amount of Mn^{3+}, but rather causes the formation of more surface Mn_3O_4; an oxidation of LMO leads to a surface reduction through oxygen loss.

4.5 CONCLUSIONS

Mn_3O_4 is a robust surface phase in the $Li_{1-x}[Mn_2]O_4$ system regardless of the chemical treatment that is applied and the level of lithiation. The surface of $Li_{1-x}[Mn_2]O_4$ will contain at least a thin layer of Mn_3O_4 that is cubic due to a lack of Jahn-Teller cooperativity; but when the layer becomes thicker, it gains sufficient cooperativity to undergo a thermodynamically-favorable tetragonal distortion. Surface reconstruction to Mn_3O_4 occurs in untreated LMO and all of the chemically-treated samples indicating an unavoidable surface disproportionation of Mn ($Mn_b^{3+} + Mn_s^{3+} \rightarrow Mn_b^{4+} + Mn_s^{2+}$). Our

results indicate the inherent stability of Mn_3O_4 as a surface layer in the $Li_{1-x}[Mn_2]O_4$ ($0<x<1$) system; whether the Mn_3O_4 layer is cubic or tetragonal depends on its thickness.

Chapter 5: Surface Reconstruction of $LiNi_{0.5-x}Mn_{1.5+x}O_4$

We have studied the $LiNi_{0.5-x}Mn_{1.5+x}O_4$ system in order to understand how Ni doping affects the surface reconstruction of LMO[2]. We find that the surface of LNM reconstructs into a mixture of a Ni-rich rock-salt phase and a Mn_3O_4 phase, previously identified to be associated with LMO. Mn-rich LNM ($LiNi_{0.45}Mn_{1.55}O_4$) undergoes a similar surface reconstruction that displays noticeably more Mn_3O_4 surface phase. Annealing the samples does not completely remove the surface Ni-rich rock-salt phase.

5.1 INTRODUCTION

$LiNi_{0.5}Mn_{1.5}O_4$ and $LiMn_2O_4$ both possess high rate capability due to the three-dimensional diffusion of Li^+ through their cubic spinel crystal structures, but LNM has a higher energy density due to its higher operating voltage versus Li (~4.7 V vs Li^0)[7]. The higher voltage is due to the electrochemically active $Ni^{2+/3+}$ and $Ni^{3+/4+}$ redox couples of LNM, which are both pinned at the top of the O-2p bands at about 4.7 V versus metallic lithium (Li^0) as compared to only 4.1 V for LMO. The higher energy density that is a result of the higher operating voltage of LNM does not come without a penalty in the form of oxidation of the electrolyte, which occurs at a voltage >4.5 V versus metallic lithium[54]. Additionally, LNM is difficult to synthesize without a Ni-rich rock-salt phase ($Li_xNi_{1-x}O$) impurity, which may be reversibly desorbed/absorbed from the spinel phase during a heating cycle that crosses 600-700°C[7,35]. Both LNM and LMO possess cyclability problems associated with surface effects, but the nature of the surface electrochemistry differs greatly; surface disproportion of Mn leading to the loss of Mn^{2+}

---

[2] J. Song, D. W. Shin, Y. Lu, C. D. Amos, A. Manthiram, J. B. Goodenough, "Role of Oxygen Vacancies on the Performance of $Li[Ni_{0.5-x}Mn_{1.5+x}O_4$ (x=0, 0.05, and 0.08) Spinel Cathodes for Lithium-Ion Batteries," *Chemistry of Materials*, Vol. 24, Issue 15, pp. 3101−3109 (2012). Charles D. Amos performed the HAADF STEM characterization of the samples in the above work.

to the electrolyte for LMO and the high redox potential of $Ni^{2+/4+}$ oxidizing the electrolyte at the cathode/electrolyte interface for LNM. We have studied these differences in relation to surface chemistry and surface structure by examining two different chemistries; stoichiometric LNM which is nominally $LiNi_{0.5}Mn_{1.5}O_4$ and Mn-rich LNM, which is nominally $LiNi_{0.45}Mn_{1.55}O_4$.

5.2 EXPERIMENTAL METHODS

The samples analyzed in this work are those used in a previously published body of work[35]. The results, discussion, and conclusions presented here represent a composite of additional work carried out on the samples after publication and the results, discussion, and conclusions presented in that work.

5.2.1 Material Synthesis

All LNM and Mn-rich LNM samples were synthesized with a hydroxide coprecipitation method. See section 2.1 Material Synthesis for the synthesis procedure.

5.2.2 Heat Treatments

LNM and Mn-rich LNM samples were subjected to several different heat treatments. The mixed Li and transition metal hydroxide precursors in all samples were preheated as a pellet at 600°C for 6 hours, reground, and heated to 900°C for 12 hours. Individual samples were then cooled at different rates; slow-cooled (1°C/min), fast-cooled (10°C/min), or quenched in liquid nitrogen from the 900°C forming temperature. Certain samples were annealed at 700°C for 48 hours followed by slow cooling.

5.2.3 Materials Characterization

Samples were analyzed with high-angle annular dark-field (HAADF) scanning transmission electron microscopy (STEM). HAADF STEM images were taken on a

JEOL ARM200F TEM with 200 kV acceleration voltage and a convergence angle between 24 and 27 mrad. Each STEM image indicates the dose rate, the total dose for the image, and a geometric factor (GF). A probe diameter of ~1.0 Å is assumed in all calculations for dose rate and total dose. All STEM images were collected under high-vacuum conditions (< 1 x 10^{-7} Torr). STEM simulations (section 2.3.2.2 STEM Simulations) were used for phase identification.

5.3 RESULTS

5.3.1 Previously Published Results

The following is from a previously published body of work[35]. Thermogravimetric Analysis (TGA) revealed that quenched LNM gains weight in the form of oxygen upon heating between 250°C and 700°C. After the quenched LNM sample surpasses 700°C, it begins to lose weight. When the sample is slowly cooled from above 700°C, oxygen is reabsorbed by the material indicating reversible oxygen absorption/desorption when thermally cycling through 700°C. All samples displayed reversible oxygen absorption/desorption through 700°C.

XRD of slow-cooled LNM reveals the cubic spinel phase with $Fd\bar{3}m$ space group and a small amount of cation-rich rock-salt phase with $Fm\bar{3}m$ symmetry. XRD of slow-cooled Mn-rich LNM is fitted with the same space groups as slow-cooled LNM, but with a significantly reduced amount of rock-salt phase. Fast-cooled LNM is fitted well with $Fd\bar{3}m$ and $Fm\bar{3}m$ space groups and contains more rock-salt phase than its slow-cooled counterpart. Fast-cooled Mn-rich LNM is also fit well with $Fd\bar{3}m$ and $Fm\bar{3}m$ space groups, but with significantly less rock-salt phase as compared with fast-cooled LNM. There is no rock-salt phase present in any of the annealed samples. Both annealed LNM and annealed Mn-rich LNM are fitted with $P4_332$ symmetry to account for additional

superlattice peaks, indicative of Ni/Mn long-range ordering on the octahedral sites. XRD of the quenched LNM sample is well-refined with $Fd\bar{3}m$ and $Fm\bar{3}m$ symmetries and displays a substantial amount of rock-salt phase.

LNM and Mn-rich LNM samples show no differences in cycling at room temperature regardless of the heat treatment that is applied. Mn-rich LNM samples exhibit superior capacity retention during high temperature cycling (55°C) as compared with LNM samples regardless of the heat treatment. No significant changes in structure are revealed with XRD of LNM samples taken before and after 100 cycles at 55 °C. This indicates that high-temperature cycling performance is related to a surface reaction with the electrolyte and not to bulk properties.

A time-of-flight secondary ion mass spectrometry (ToF-SIMS) depth profile of slow-cooled LNM showed a higher concentration of Ni near its surface as compared with its bulk. Slow-cooled Mn-rich LNM displayed a lower concentration of Ni at its surface as compared with its bulk.

5.3.2 Unpublished Results

HAADF STEM of slow-cooled LNM (Figure 5-1) reveals a surface composed of a mixture of rock-salt and Mn_3O_4 phases. The rock-salt and Mn_3O_4 phases do not exist as a uniform mixture throughout the material's surface. Surface regions composed exclusively of Mn_3O_4 are seen over a relatively large area in some instances (Figure 5-2). Quenching LNM in liquid nitrogen from 900°C results in a phase composed entirely (bulk and surface) of a rock-salt phase (Figure 5-3). HAADF STEM of slow-cooled Mn-rich LNM (Figure 5-4) reveals a surface composed of a mixture of rock-salt phase and Mn_3O_4 phase. Just as with slow-cooled LNM, slow-cooled Mn-rich LNM's surface does

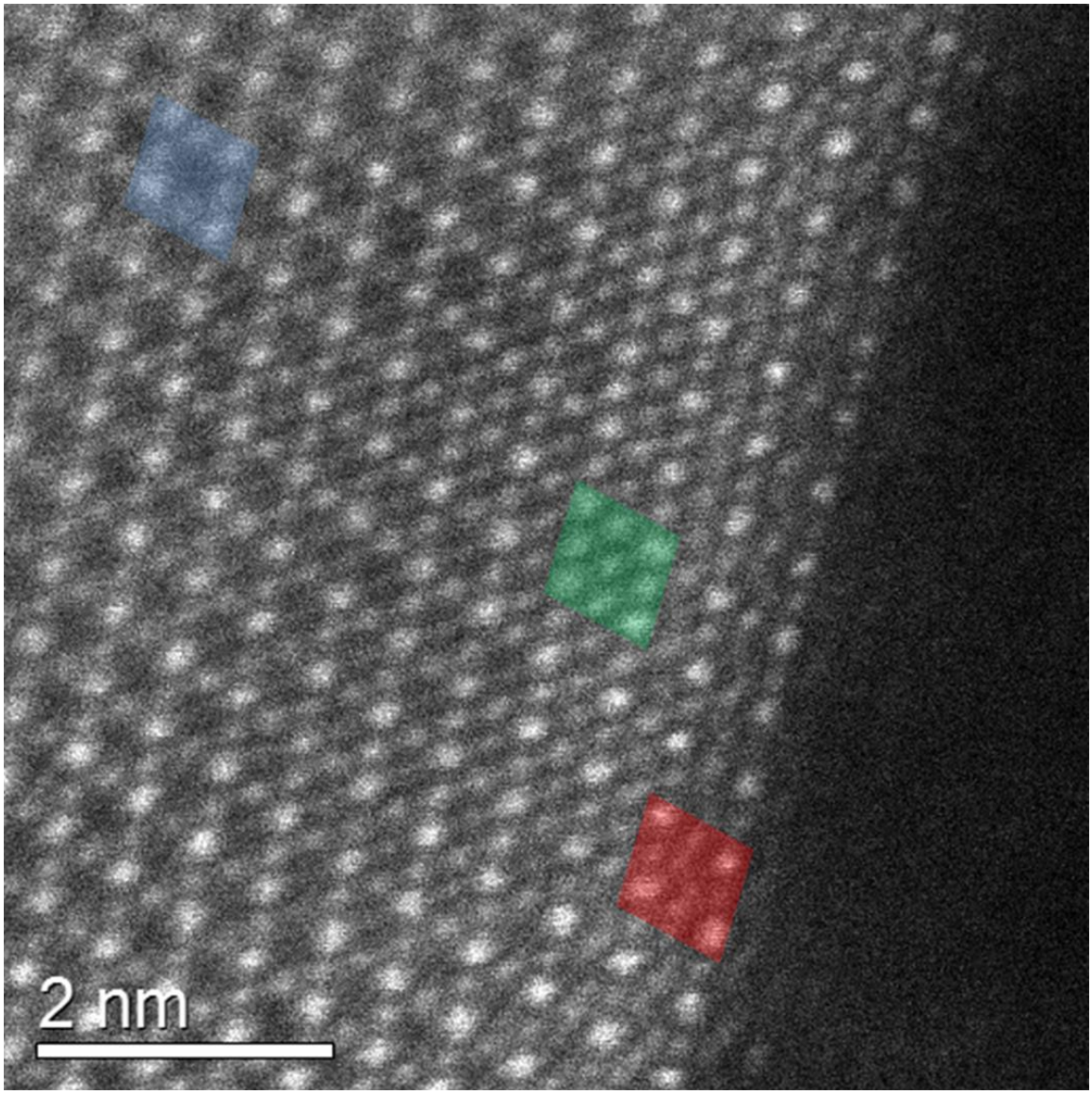

Figure 5-1: HAADF STEM image of slow-cooled LNM. Observed in the image is the bulk spinel LNM framework (blue), the Mn_3O_4 phase (red), and a rock-salt phase (green). Although all three are observed in this image, there are regions of slow-cooled LNM that contain only the regular spinel structure and Mn_3O_4 (Figure 5-2). (ARM200F, Dose Rate: 1.0 x 10^8 $e^-/Å^2 \cdot s$, Dose: 1.5 x 10^5 $e^-/Å^2$, GF: 40).

not contain a uniform mixture of rock-salt and Mn_3O_4 phases. Surface regions composed exclusively of Mn_3O_4 are seen over relatively large areas (Figure 5-5 and 5-6). There are

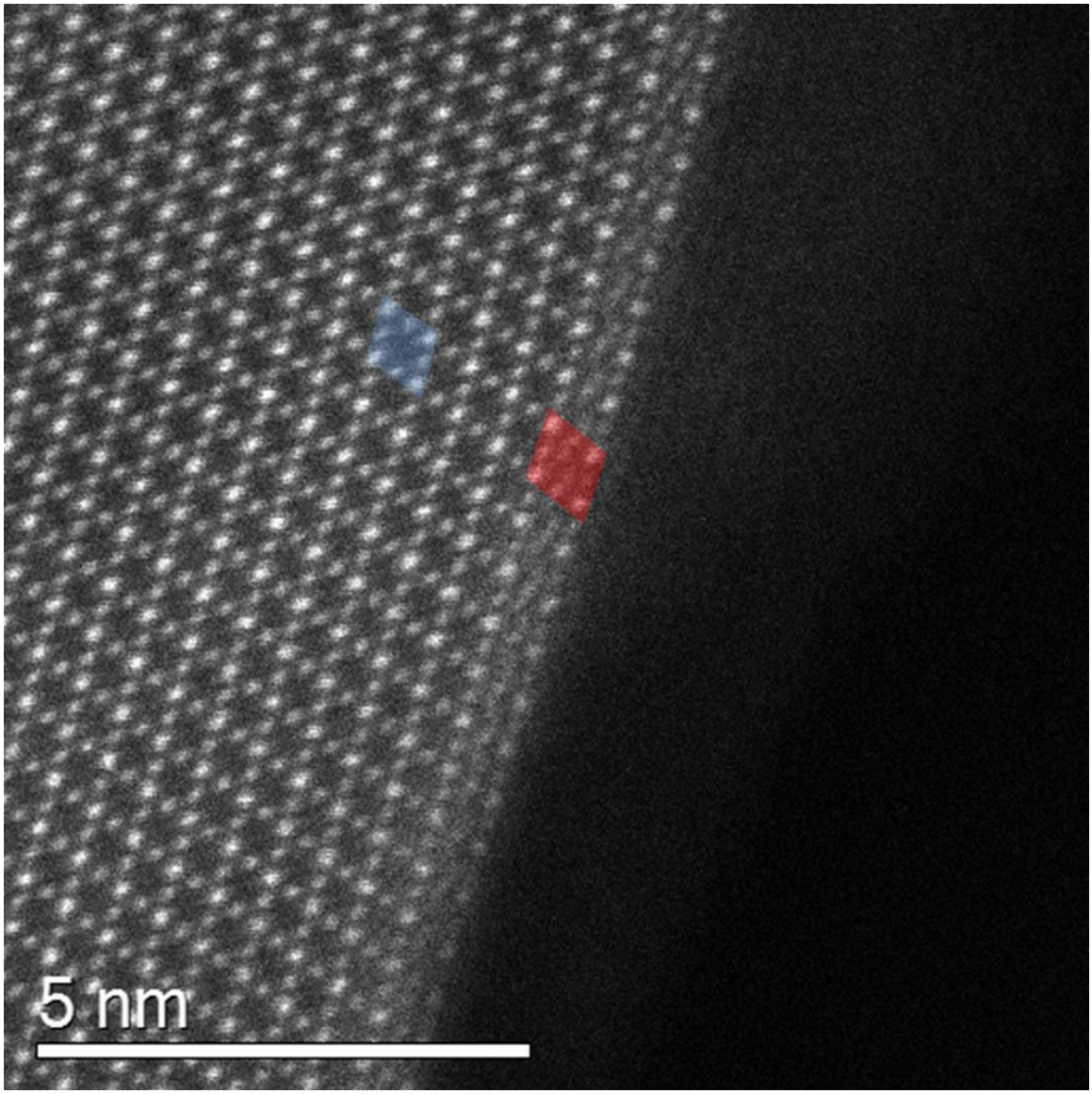

Figure 5-2: HAADF STEM image of slow-cooled LNM in a region of a particle that contains only a thin Mn_3O_4 surface phase (red) and the bulk spinel LNM framework (blue) without a rock-salt phase. (ARM200F, Dose Rate: 1.0 x 10^8 $e^-/Å^2 \cdot s$, Dose: 6.0 x 10^4 $e^-/Å^2$, GF: 16).

significantly more Mn_3O_4 surfaces with the slow-cooled Mn-rich sample. It is found with HAADF STEM that annealed Mn-rich LNM contains both rock-salt and Mn_3O_4 surface

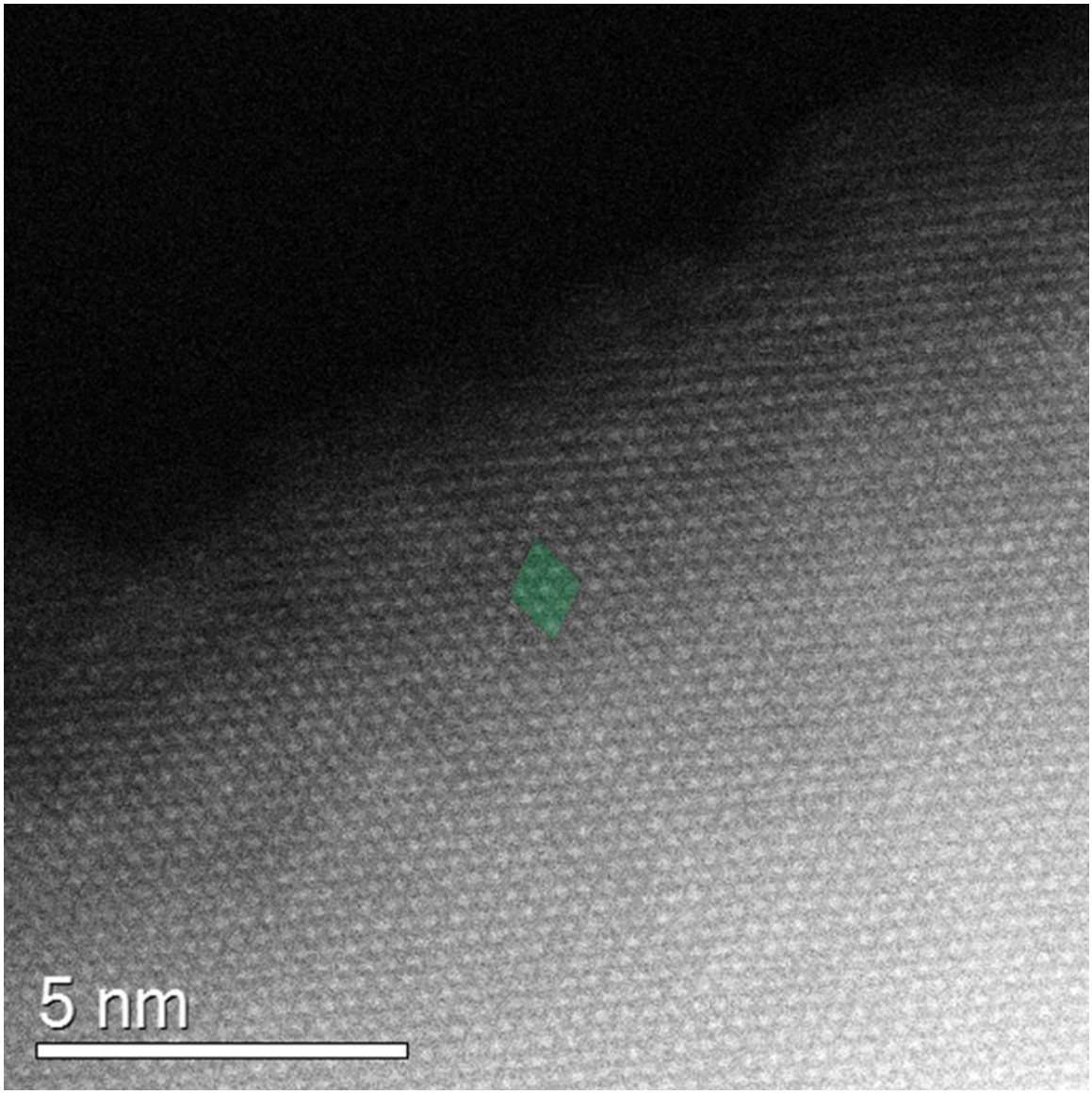

Figure 5-3: HAADF STEM image of quenched LNM revealing a bulk and surface made entirely of the rock-salt phase (green). (ARM200F, Dose Rate: 1.0 x 10^8 e^-/Å^2·s, Dose: 2.8 x 10^4 e^-/Å^2, GF: 9).

phases (Figure 5-7), even though it is the least likely sample to contain the rock-salt phase according to XRD and ToF-SIMS. Annealed Mn-rich LNM, as with the other samples, has an inhomogeneous mixture of rock-salt phase and Mn_3O_4 phase mixing and

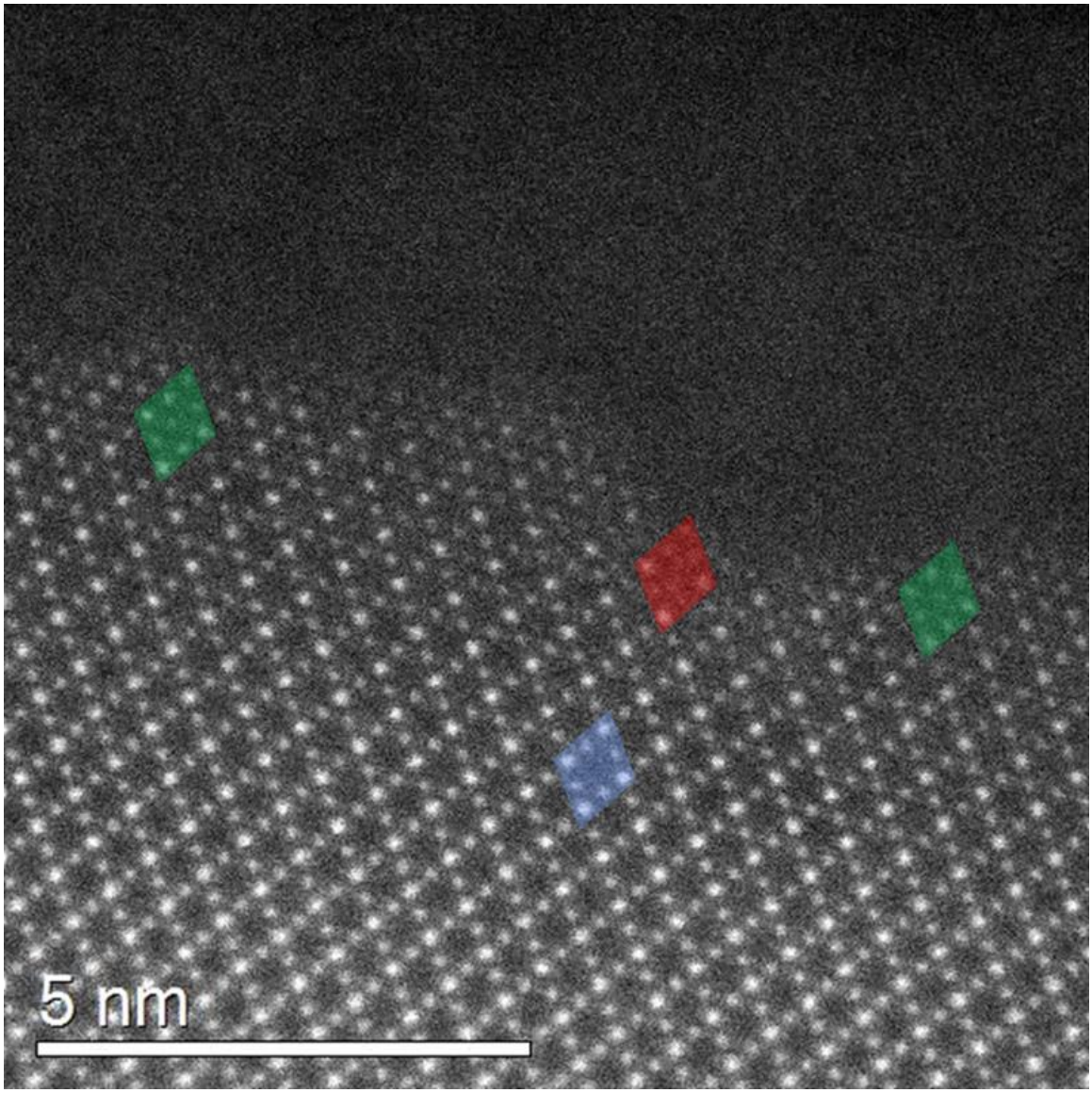

Figure 5-4: HAADF STEM image of slow-cooled Mn-rich LNM. The surface is composed of a mixture of Mn_3O_4 (red) and rock-salt (green). The bulk of the sample contains the Mn-rich LNM spinel framework (blue). (ARM200F, Dose Rate: 1.0 x 10^8 $e^-/Å^2 \cdot s$, Dose: 2.8 x 10^4 $e^-/Å^2$, GF: 9).

therefore contains surface regions that are exclusively rocksalt (Figure 5-8) or Mn_3O_4 (Figure 5-9).

5.4 DISCUSSION

Heating $LiNi_{0.5}Mn_{1.5}O_4$ beyond approximately 600-700°C produces a Ni-rich rock-salt impurity phase that is reversibly desorbed/absorbed from/to the spinel framework upon sufficiently-slow cooling[7,35]. Zhong et al. proposed the following disproportionation reaction above the temperature to induce weight loss[7]:

$$LiNi_{0.5}Mn_{1.5}O_4 = qLi_xNi_{1-x}O + rLiNi_{0.5-y}Mn_{1.5+y}O_4 + sO_2$$

which produces a Ni-rich rock-salt phase and a Mn-rich spinel phase upon loss of oxygen. Indeed, it is observed in Figure 5-3 that quenching LNM in liquid nitrogen from 900°C freezes a significant amount of rock-salt phase due to insufficient oxygen uptake upon cooling. We have shown previously that surface disproportionation of Mn and oxygen deficiency lead to a surface reconstruction of LMO into a Mn-rich Mn_3O_4 surface phase and a Li-rich $Li_{1+x}Mn_2O_4$ subsurface phase with preservation of the bulk $LiMn_2O_4$ spinel framework. Assuming a uniform distribution of Ni, a deficiency of oxygen at the surface of LNM would lead to the formation of segregated Ni-rich rock-salt and Mn_3O_4 surface phases, which is consistent with the phases observed in Figure 5-1 and the disproportionation reaction asserted by Zhong. It was also observed in the LNM system that several regions of the surface contain only Mn_3O_4 (Figure 5-2). This observation may be explained by the fact that perfect mixing of Ni and Mn is difficult to achieve in practice. Inhomogeneous Mn and Ni mixing would lead to areas rich in Mn and areas rich in Ni. Mn-rich areas would produce LMO, which is coherent with LNM phase and which undergoes a surface reconstruction to Mn_3O_4. Ni-rich areas would produce the Ni-rich rock-salt phase. The observation of surfaces containing only Mn_3O_4 may also be explained by a surface-plane-dependent surface reconstruction of LNM. Figure 5-2 shows a surface that contains only Mn_3O_4 along a (111) surface. Even though homogenous mixing of Mn and Ni may occur, a thin layer of Mn_3O_4 may preferentially

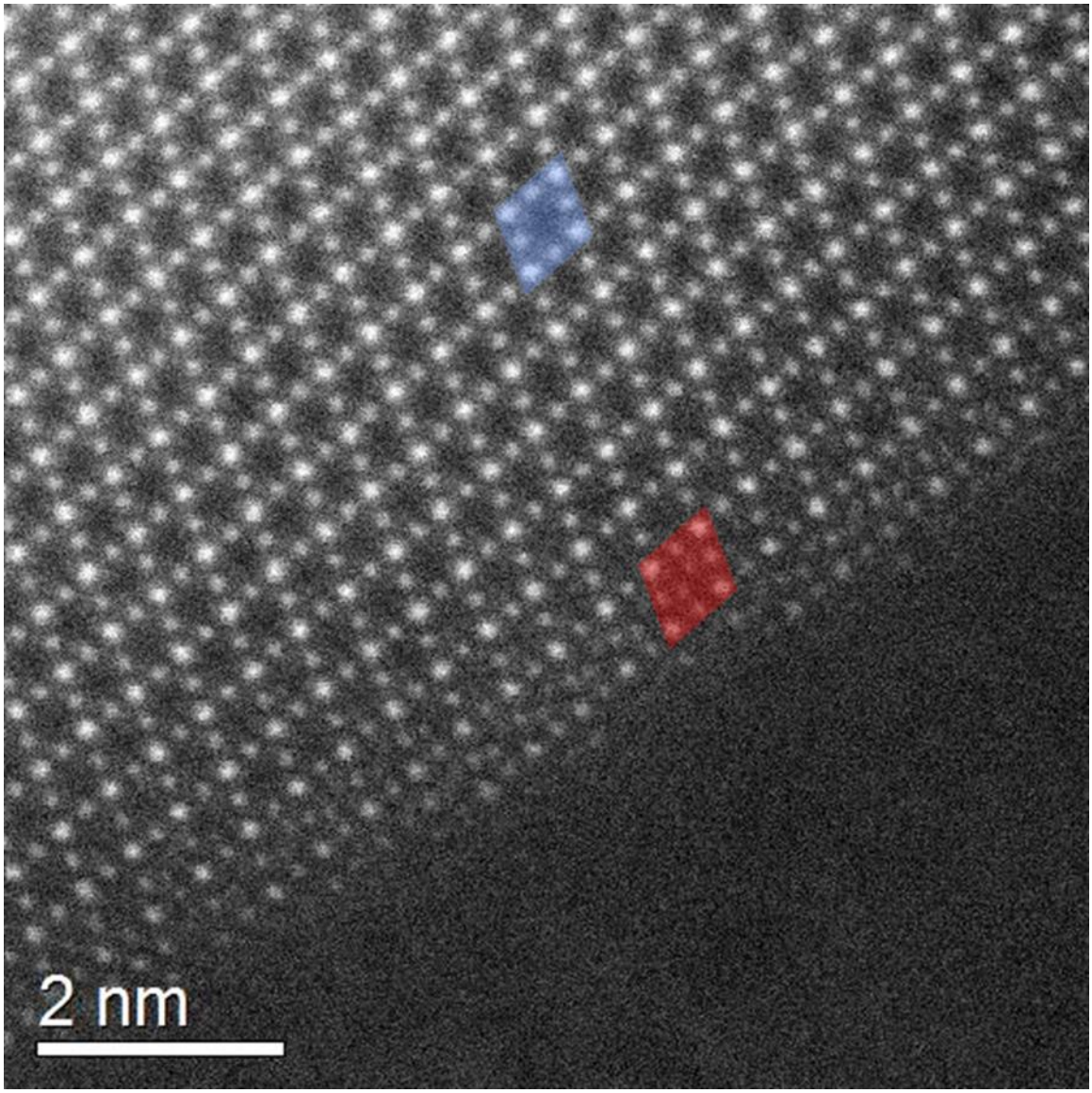

Figure 5-5: HAADF STEM image of slow-cooled Mn-rich LNM. The surface is composed exclusively of Mn_3O_4 (red) with retention of the bulk spinel framework of Mn-rich LNM (blue). (ARM200F, Dose Rate: 1.0 x 10^8 $e^-/Å^2 \cdot s$, Dose: 8.4 x 10^4 $e^-/Å^2$, GF: 27).

occur along {111} as a result of a greater availability of tetrahedral sites. LNM surfaces differ in stability, which may dictate the extent of oxygen loss, the driving force for the surface reconstruction. Surface disproportionation of Mn may still occur, which produces

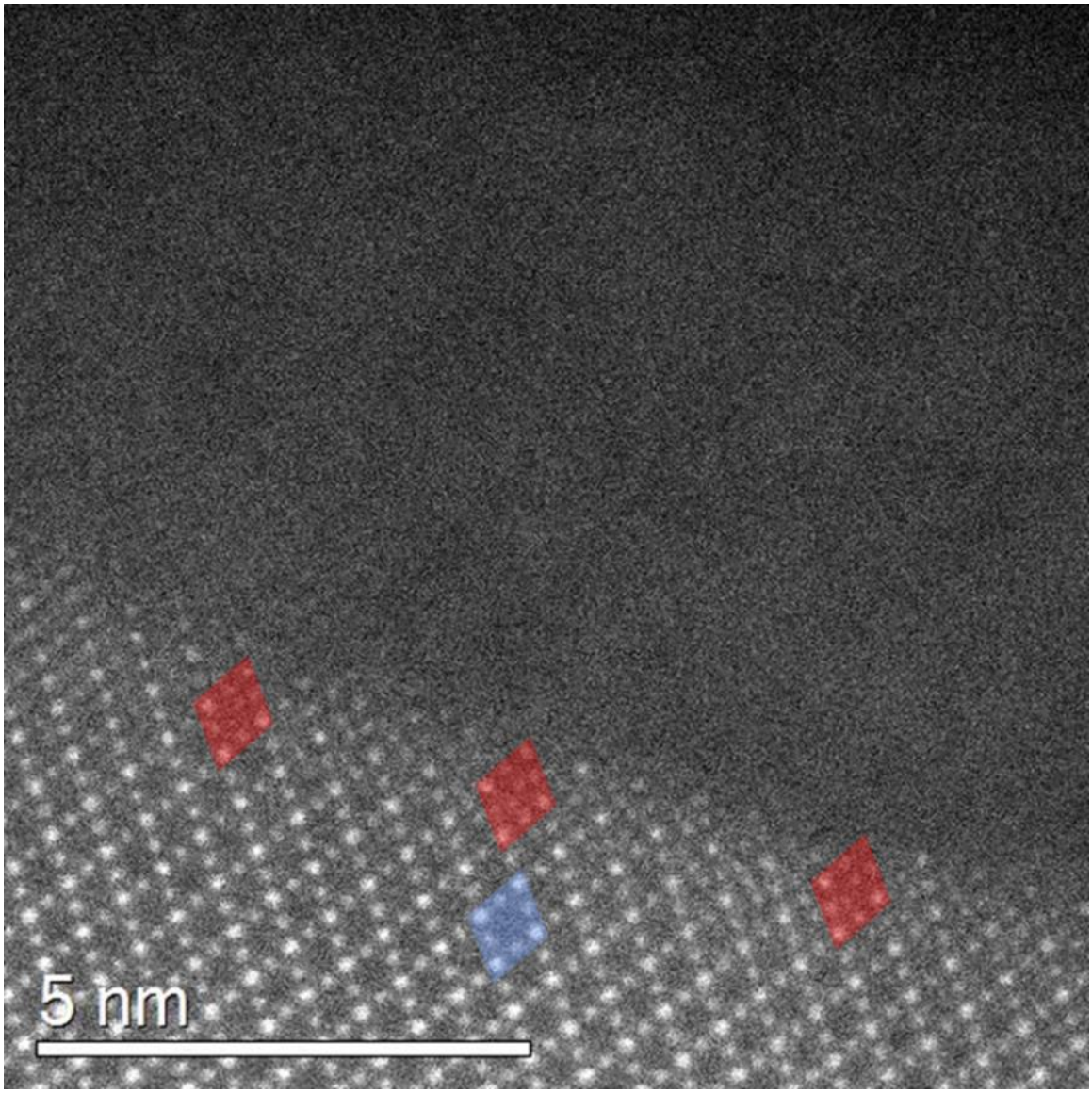

Figure 5-6: HAADF STEM image of slow-cooled Mn-rich LNM. The surface is composed exclusively of Mn_3O_4 (red) with retention of the bulk spinel framework of Mn-rich LNM (blue). (ARM200F, Dose Rate: 1.0 x 10^8 e^-/Å^2·s, Dose: 5.0 x 10^4 e^-/Å^2, GF: 16).

tetrahedrally-coordinated Mn^{2+}, but the disproportionation of the LNM spinel phase into a Ni-rich rock-salt phase and Mn-rich spinel phase may not.

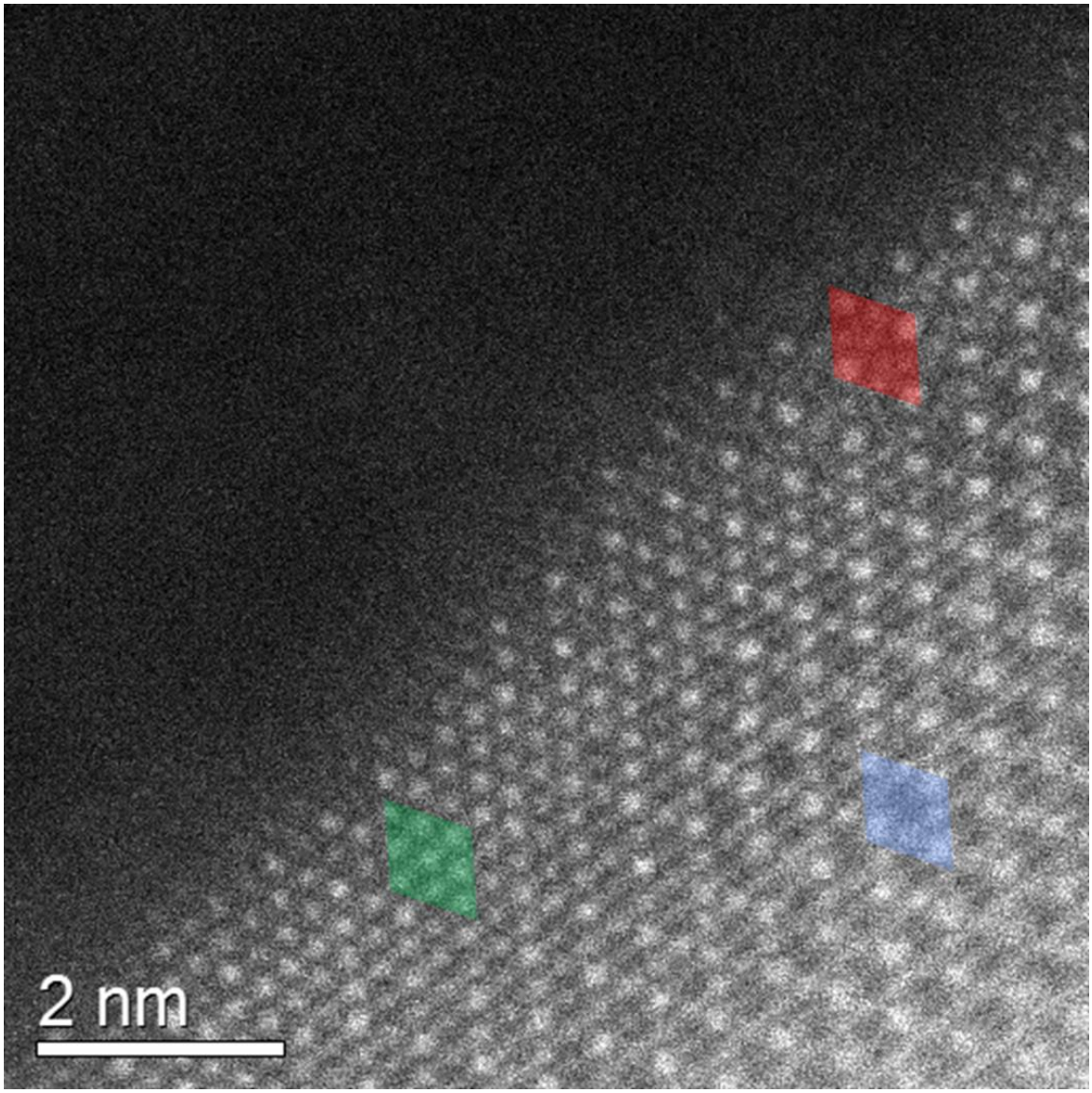

Figure 5-7: HAADF STEM image of annealed Mn-rich LNM. The surface is composed of a mixture of Mn_3O_4 (red) and rock-salt (green). The bulk of the sample contains the Mn-rich LNM spinel framework (blue). (ARM200F, Dose Rate: 1.0 x 10^8 $e^-/Å^2 \cdot s$, Dose: 1.0 x 10^5 $e^-/Å^2$, GF: 27).

Mn-rich LNM, like stoichiometric LNM, contains a surface composed of mixed Ni-rich rock-salt phase and Mn_3O_4 as seen in Figure 5-4, but there are more surfaces that

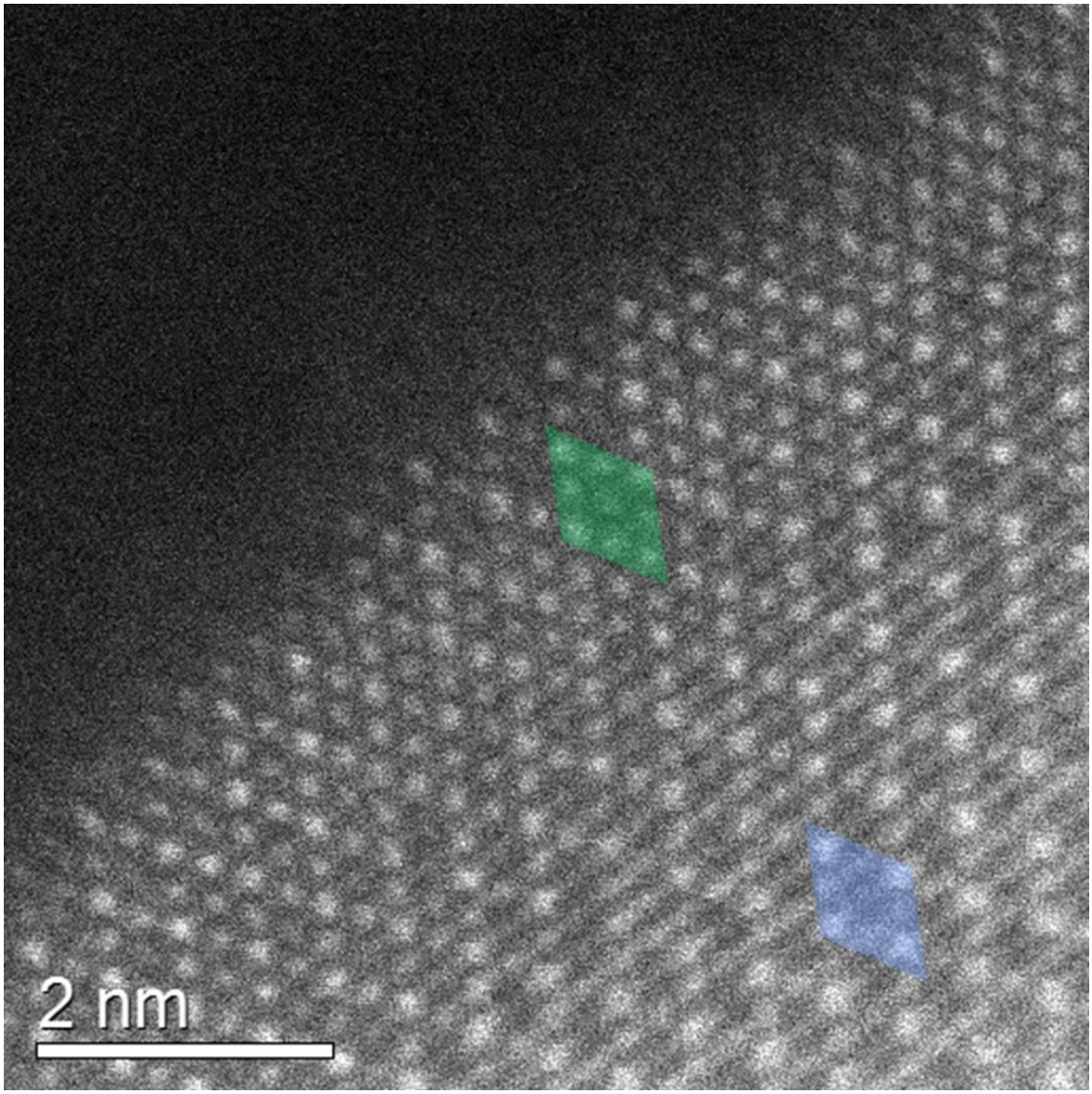

Figure 5-8: HAADF STEM image of annealed Mn-rich LNM. The surface is composed exclusively of rock-salt phase (green) with retention of the bulk spinel framework of Mn-rich LNM (blue). (ARM200F, Dose Rate: 1.0 x 10^8 $e^-/Å^2 \cdot s$, Dose: 1.5 x 10^5 $e^-/Å^2$, GF: 40).

contain Mn_3O_4 (Figure 5-5 and 5-6). This is expected due to the higher content of Mn in the Mn-rich LNM sample as compared with stoichiometric LNM; however the amount of surface Mn_3O_4 seems to be more than an effect of increased Mn content. ToF-SIMS

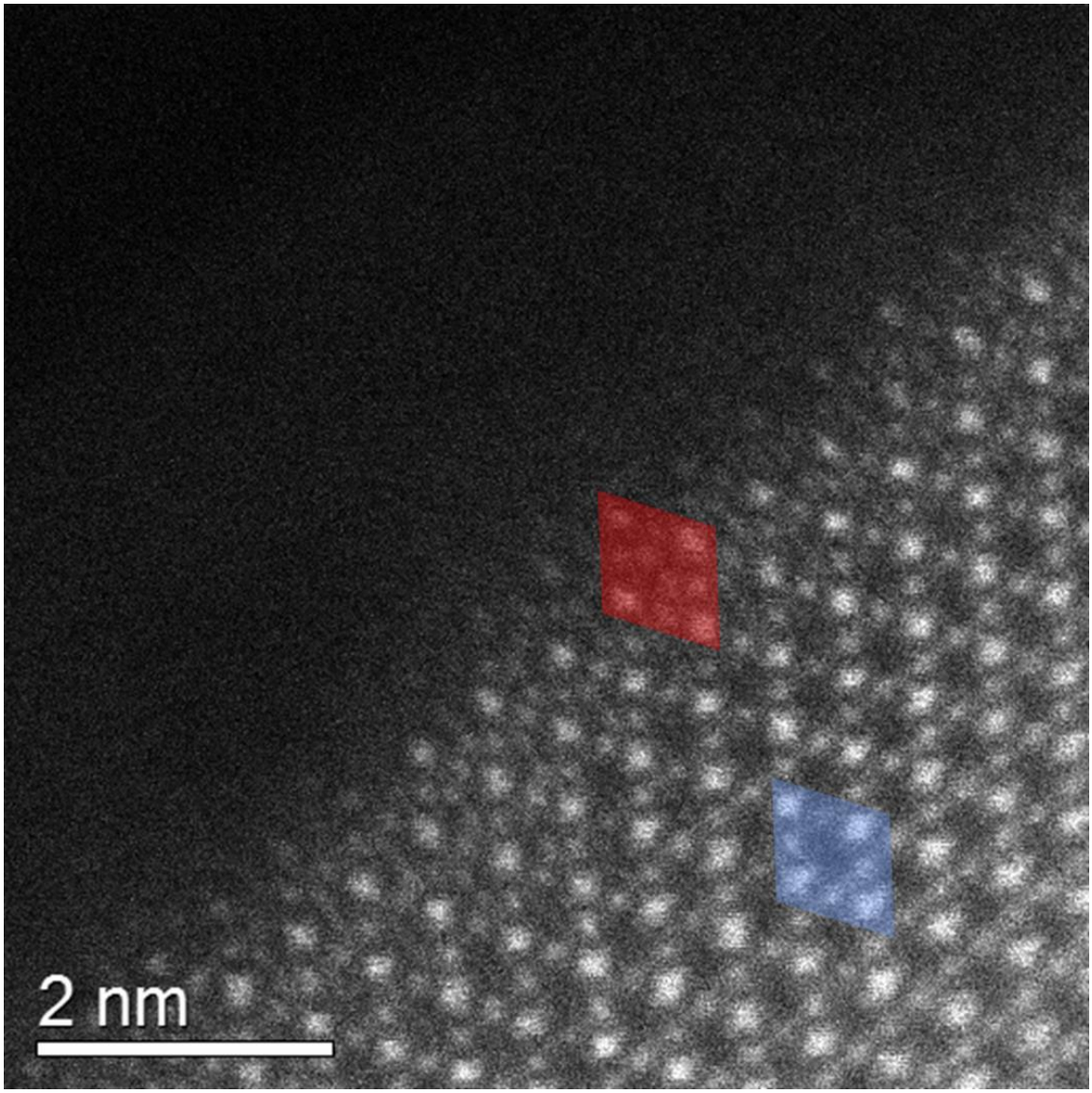

Figure 5-9: HAADF STEM image of annealed Mn-rich LNM. The surface is composed exclusively of Mn_3O_4 (red) with retention of the bulk spinel framework of Mn-rich LNM. (ARM200F, Dose Rate: 1.0 x 10^8 $e^-/Å^2$·s, Dose: 1.3 x 10^5 $e^-/Å^2$, GF: 40).

reveals that the concentration of Ni at the surface of LNM is higher than its bulk concentration and the concentration of Ni at the surface of Mn-rich LNM is lower than its bulk concentration. Stoichiometric LNM will contain a maximum amount of rock-salt

phase, which contains a higher concentration of Ni than bulk LNM leading to the aforementioned increase in surface Ni content. As more Mn is added to LNM, surfaces will contain less rock-salt phase and the amount of LMO phase will increase. Since LMO has a larger lattice parameter than LNM (8.237 Å from commercial LMO as compared to 8.179 Å from slow-cooled LNM) the LMO phases can preferentially segregate to the surface of LNM in order to minimize the strain difference (0.71%) between the phases. This may explain the drastic overall difference in surface Ni content of the LNM and Mn-rich LNM samples.

In our previously published work we observed that Mn-rich LNM cycles better than stoichiometric LNM at elevated temperatures, likely due to the reduction of surface rock-salt phase and elimination of Ni from the surface of the material[35]. It appears that increased Mn content, and therefore increased Mn_3O_4 surface phase, is advantageous from a cycling standpoint, but increased Mn content leads to a lowering of overall energy density due to a lower operating voltage of the $Mn^{3+/4+}$ redox couple. If LNM did in fact undergo a surface-plane-dependent surface reconstruction that produced Mn_3O_4-specific surfaces, then the energy density of LNM may be preserved while maintaining the superior cycling characteristics of a Mn_3O_4-rich surface. Indeed, it has been shown that morphology-controlled LNM does produce differences in cycling characteristics[55]. Octahedral and cubic LNM particles exhibit superior cycling as compared with truncated or spherical LNM particles. The superior cycling performance of octahedral {111} and cubic LNM particles ({111} and $\{11\bar{2}\}$) may be explained by a surface-plane-dependent surface reconstruction of LNM that produces Mn_3O_4 surfaces along specific facets.

5.5 CONCLUSIONS

We find that $LiNi_{0.5}Mn_{1.5}O_4$ and $LiNi_{0.45}Mn_{1.55}O_4$ both undergo a surface reconstruction to a mixture of rock-salt and Mn_3O_4 phases. Mn-rich LNM contains more Mn_3O_4 surface phases than LNM due to higher Mn content and lower surface Ni content. Annealing samples does not completely remove the surface rock-salt phase predicted to be eliminated by TGA.

Chapter 6: Effect of Trivalent Doping on Surface Reconstruction of $LiNi_{0.5}Mn_{1.5}O_4$

We have studied the $LiNi_{0.45}Cr_{0.1}Mn_{1.45}O_4$ system in order to understand how doping LNM with trivalent Cr affects the surface reconstruction of LNM. We find that the surface of Cr-doped LNM reconstructs into an ordered-spinel/rock-salt structure.

6.1 INTRODUCTION

As mentioned previously, $LiNi_{0.5}Mn_{1.5}O_4$ possesses a high rate capability due to the three-dimensional diffusion of Li^+ through its cubic spinel crystal structures and it has a high energy density due to its higher operating voltage versus Li (~4.7 V vs Li^0)[7]. However, the operating voltage of LNM lies beneath the HOMO of the liquid organic electrolyte, which is oxidized at a voltage greater than 4.5V versus metallic lithium[54]. In order to take advantage of the enticing properties of LNM, improvements in cycling must be made. One route toward this goal is doping. Doping LNM with trivalent cations such as Cr, Fe, Ga, and Al can lead to enhanced cyclability[54,56,57,58]. Since the concentration of dopants is low and since they do not alter the operating voltage appreciably, the effect of the dopant must be a surface effect. We have shown that LNM undergoes a surface reconstruction to create Ni-rich rock-salt and Mn_3O_4 surface phases. The surface layer thickens with increasing cooling rate; insufficient oxygen uptake during the cooling process restricts the transformation of the rock-salt phase back to the spinel phase near the surface, which results in a thicker layer of the mixed phases. In order to study additional effects on the surface reconstruction of LNM, we have studied Cr-doped LNM ($LiNi_{0.45}Cr_{0.1}Mn_{1.45}O_4$), which represents doping of LNM with a trivalent cation having a strong octahedral site preference.

6.2 EXPERIMENTAL METHODS

6.2.1 Material Synthesis

$LiNi_{0.45}Cr_{0.1}Mn_{1.45}O_4$ was synthesized with a hydroxide coprecipitation method. See section 2.1 Material Synthesis for the synthesis procedure. The sample was cooled to room temperature with a cooling rate of 1°C/min.

6.2.2 Materials Characterization

$LiNi_{0.45}Cr_{0.1}Mn_{1.45}O_4$ was analyzed with high-angle annular dark-field (HAADF) scanning transmission electron microscopy (STEM). HAADF STEM images were taken on a JEOL ARM200F TEM with 200 kV acceleration voltage and a convergence angle between 24 and 27 mrad. Each STEM image indicates the dose rate, the total dose for the image, and a geometric factor (GF). A probe diameter of ~1.0 Å is assumed in all calculations for dose rate and total dose. All STEM images were collected under high-vacuum conditions (< 1 x 10^{-7} Torr). STEM simulations (section 2.3.2.2 STEM Simulations) were used for phase identification.

6.3 RESULTS

An XRD of $LiNi_{0.45}Cr_{0.1}Mn_{1.45}O_4$ fits well with the $Fd\bar{3}m$ space group with no evidence of rock-salt impurity phase (Figure 6-1). HAADF STEM of Cr-doped LNM (Figure 6-2) reveals a surface and bulk composed of an ordered-spinel/rock-salt phase. The phase extends from the bulk to the surface. Increasingly higher magnifications are shown of the ordered phase, Figure 6-3 and Figure 6-4, respectively. The only other phase seen is a pure rock-salt phase without ordering that only occurs under damaging beam conditions (Figure 6-5).

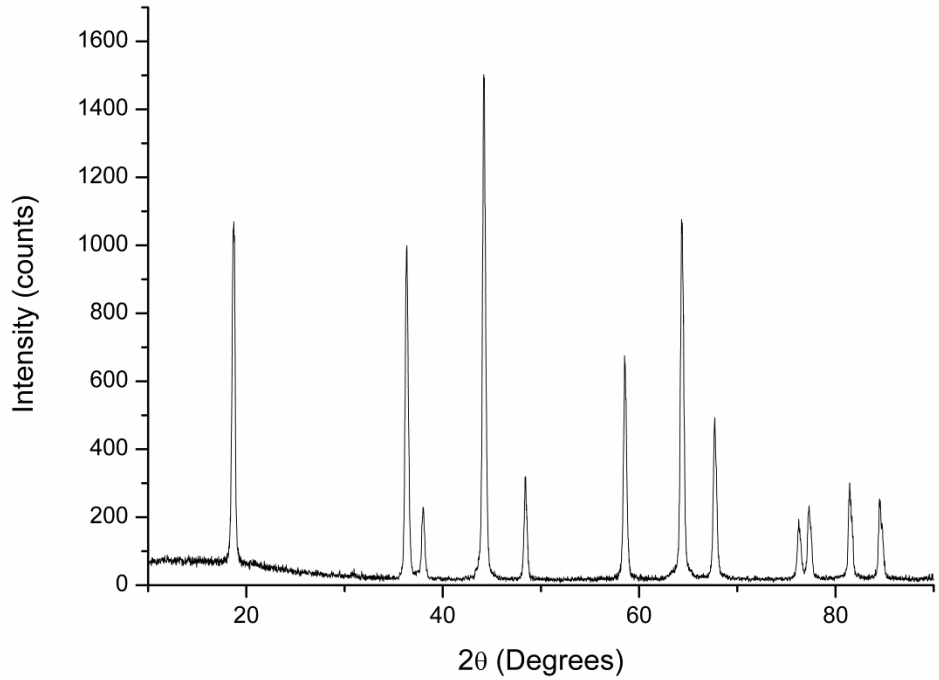

Figure 6-1: XRD pattern of Cr-doped LNM. The pattern is consistent with the $Fd\bar{3}m$ space group with no evidence of $P4_332$ superlattice peaks or rock-salt impurity phase.

6.4 DISCUSSION

XRD of Cr-doped LNM (Figure 6-1) fits well with the $Fd\bar{3}m$ space group indicating no transition metal ordering on the 16d octahedral sites, which is consistent with another study[58]. Trivalent doping of LNM with Cr substitutes a Ni^{2+} and a Mn^{4+} with two Cr^{3+} cations. Since Cr^{3+} has a strong preference for octahedral sites, the substitution for Ni and Mn is straightforward in terms of replacing Ni and Mn on the 16d cubic spinel sites. Since Cr^{3+} possesses a larger ionic radius than either Mn^{4+} or Ni^{2+}, it is reasonable that Cr^{3+} segregates to the surface of LNM during synthesis as the surface layer can accommodate more easily a local lattice expansion than the bulk crystal, which is

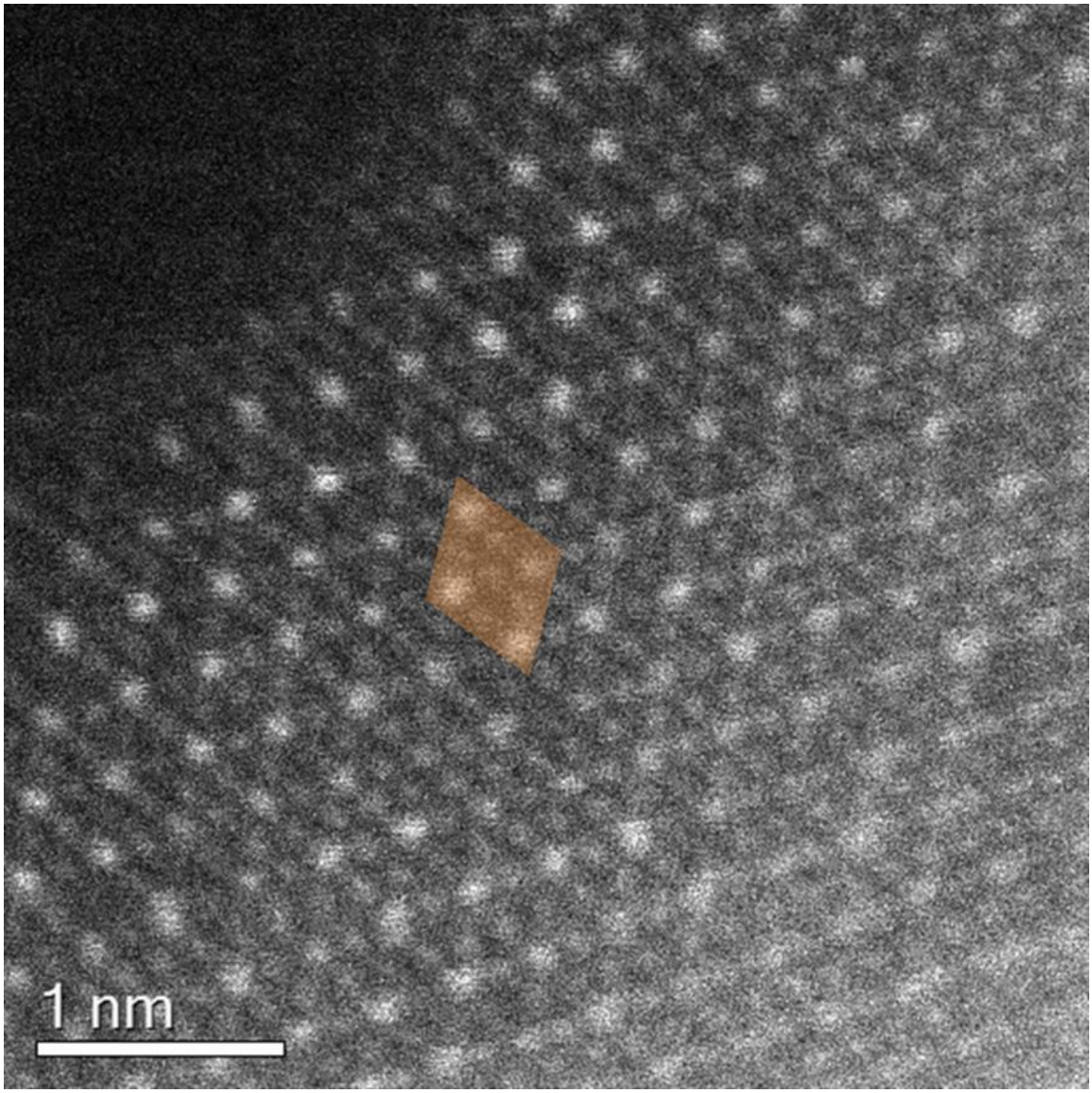

Figure 6-2: HAADF STEM image of Cr-doped LNM including the surface. Shown in the image is the only phase identified; an ordered spinel/rock-salt phase (orange). It is a unique phase, unseen in either the LMO or LNM system. It has the characteristic outline of the LNM spinel structure with bright corners, but a spot lies in the center of the diamond like the rock-salt phase. (ARM200F, Dose Rate: 1.0 x 10^8 $e^-/Å^2 \cdot s$, Dose: 2.1 x 10^5 $e^-/Å^2$, GF: 106).

consistent with the results of another study[58]. When LNM is doped with a small amount of Cr and it preferentially segregates to the surface, one of two mechanisms may

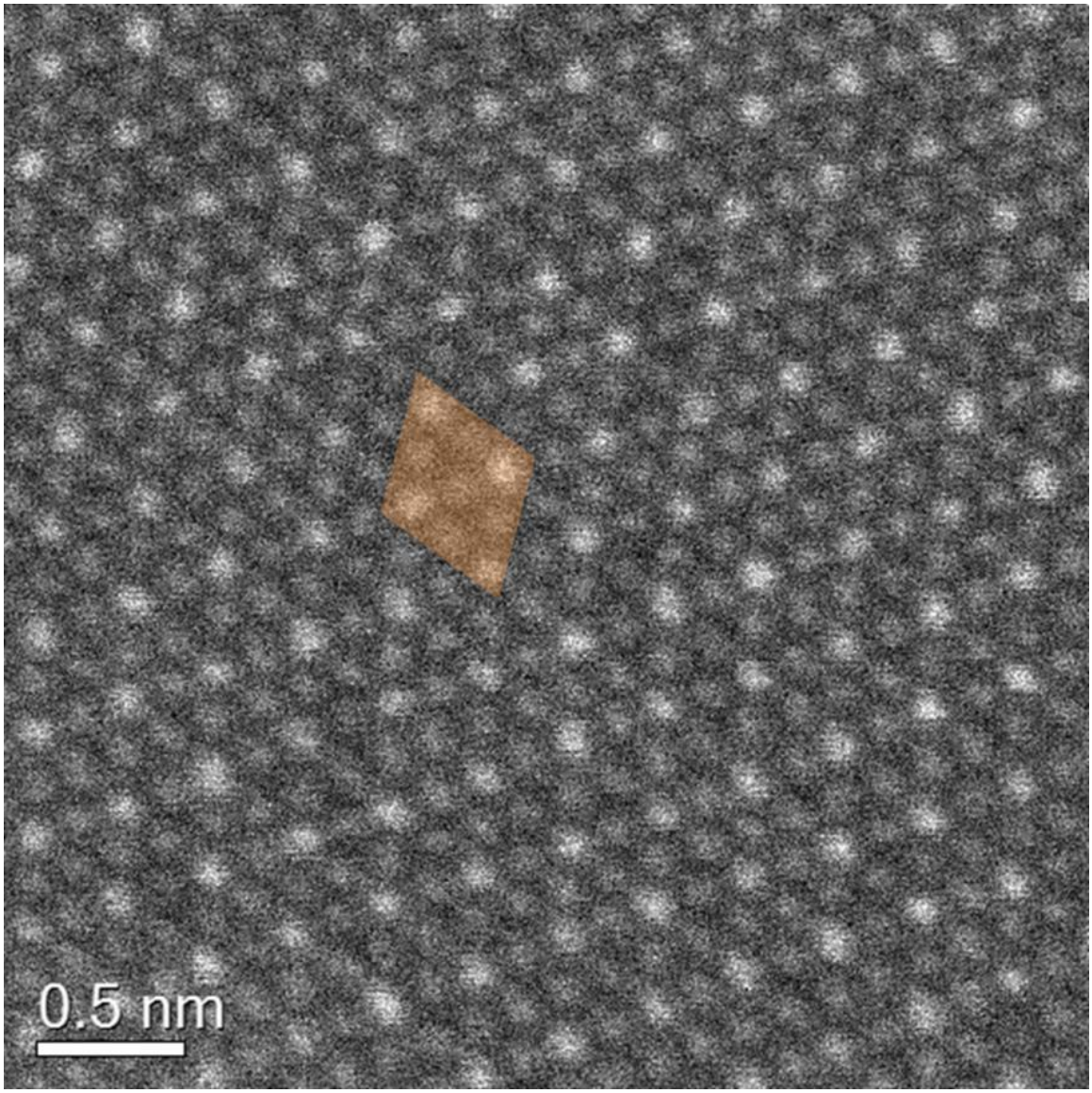

Figure 6-3: Higher resolution HAADF STEM image of Cr-doped LNM. The ordered spinel/rock-salt phase is shown in the image (orange). (ARM200F, Dose Rate: 1.0 x 10^8 $e^-/Å^2 \cdot s$, Dose: 3.0 x 10^5 $e^-/Å^2$, GF: 152).

occur to explain the ordered-spinel/rock-salt phase. The first involves the creation of a simple Cr-rich rock-salt phase at the surface of LNM. Since Cr is concentrated at the surface, oxygen deficiency, which appears to be the driving force for surface segregation in LMO and LNM, would force surface Cr into a thin surface layer of Cr-rich rock-salt

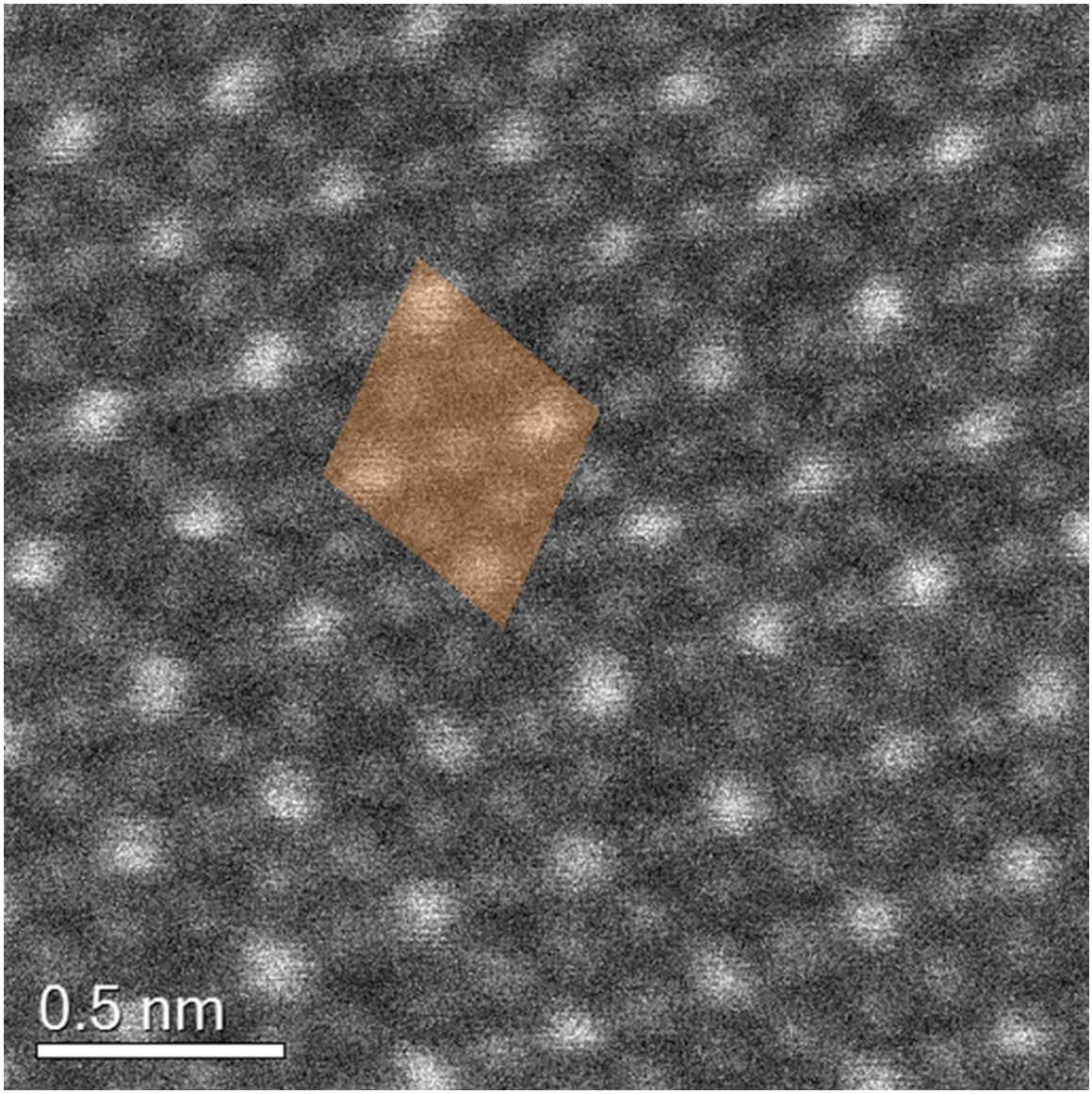

Figure 6-4: High-resolution HAADF STEM image of Cr-doped LNM. The ordered spinel/rock-salt phase is shown in the image (orange). It is easier to understand the interesting spinel/rock-salt ordering with the high resolution. The corners of the diamond are bright as can be expected with the spinel structure of LNM, but there also exists equal brightness of the inter-border spots and the center spot as would be expected with rock-salt. (ARM200F, Dose Rate: 1.0×10^8 $e^-/Å^2 \cdot s$, Dose: 8.5×10^5 $e^-/Å^2$, GF: 425).

phase. The apparent ordered-spinel/rock-salt phase would then simply be a projection of a thin Cr-rich rock-salt phase and the underlying LNM spinel phase. The second mechanism would involve the creation of an ordered-spinel/rock-salt phase, which would be the result of Cr ordering with Mn and/or Ni on both 16d and 16c octahedral sites. Since the spinel framework is still visible and distinguishable from a simple rock-salt phase, the ordering brought about by Cr would necessitate the formation of an ordered-spinel/rock-salt phase that contained transition metals on only octahedral sites and that contained less than a 1:1 cation to anion ratio as would be expected with a simple rock-salt phase.

It is interesting that there is no evidence of Mn_3O_4 surface phases, which would indicate the surface disproportionation of Mn and therefore the presence of surface Mn^{3+}. The segregation of Cr appears to either suppress the presence of Mn at the surface or to stabilize Mn^{4+} at the surface, the former being more likely due to ToF-SIMS evidence in a previous study[58]. Application of an intense electron beam damages the ordered spinel/rock-salt phase and converts it into a simple rock-salt phase. This phenomenon has been observed before in the LMO system where an intense beam at the surface of LMO turned the Mn_3O_4 and surface LMO spinel phase into a rock-salt phase by displacing O_2 from the solid. Under an intense enough electron beam, transition metal oxides are reduced with a loss of oxygen[25]. The conversion of the ordered-spinel/rock-salt phase to a pure rock-salt phase gives evidence that the ordered-spinel/rock-salt phase is the result of a surface reconstruction in Cr-doped LNM and not damage caused by observation under HAADF STEM imaging conditions.

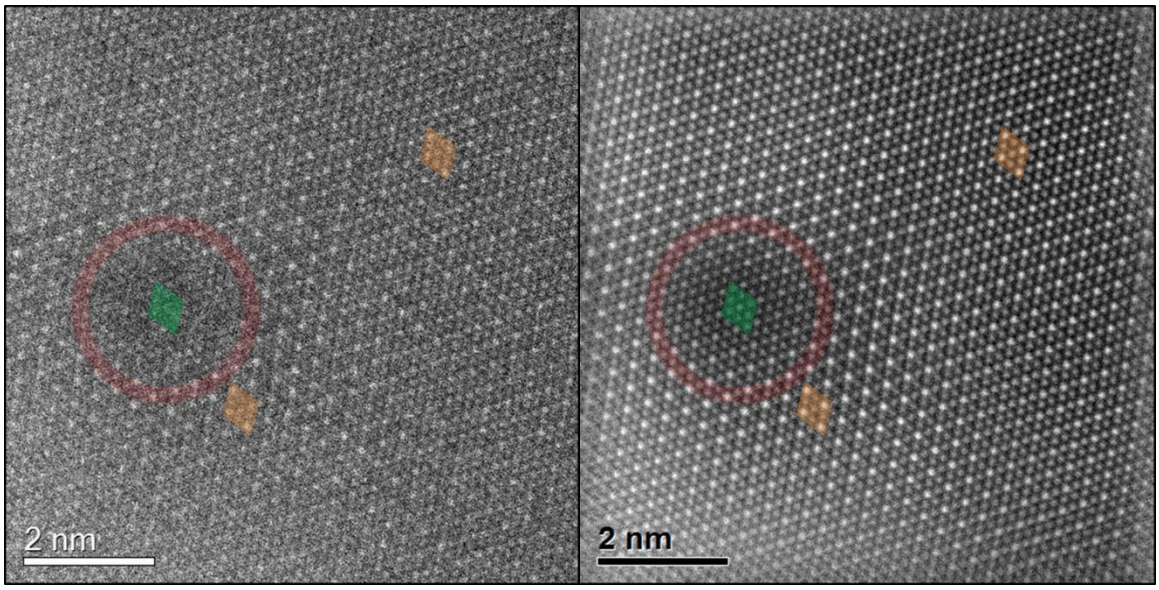

Figure 6-5: HAADF STEM image (ARM200F, Dose Rate: 1.0 x 10^8 $e^-/Å^2$·s, Dose: 5.4 x 10^4 $e^-/Å^2$, GF: 27) of Cr-doped LNM (left) showing the bulk with an area damaged by an intense electron beam (ARM200F, Dose Rate: 1.0 x 10^8 $e^-/Å^2$·s, Dose: > 1.4 x 10^{10} $e^-/Å^2$, GF: 27) (outlined in red). The orange diamonds indicate the ordered spinel/rock-salt phase and the green indicates the rock-salt phase only. The right image is a fourier-filtered image of the left image. It clarifies the phases identified and clearly demarcates the area of beam damage that is reconstructed to rock-salt phase.

6.5 CONCLUSIONS

The $LiNi_{0.45}Cr_{0.1}Mn_{1.45}O_4$ system undergoes a surface reconstruction into an ordered-spinel/rock-salt structure with no evidence of surface Mn_3O_4, which is observed in the LMO and LNM systems. Pure rock-salt phase is observed in Cr-doped LNM only under intense beam conditions that cause damage, similar to the LMO system where intense beam conditions created a rock-salt phase from the Mn_3O_4 and LMO spinel phases.

Chapter 7: Summary

$Li[Mn_2]O_4$ undergoes a surface reconstruction, which results in the production of a thin, stable surface layer of Mn_3O_4 and a subsurface region of $Li_{1+x}[Mn_2]O_4$ with retention of bulk $Li[Mn_2]O_4$. This observation is compatible with the surface disproportionation of Mn coupled with oxygen deficiency and a displacement of surface Li^+ from the Mn_3O_4 surface phase to a subsurface layer. An aqueous acid treatment, a non-aqueous chemical delithiation, and an oxygen plasma treatment were applied to $Li[Mn_2]O_4$. It was found that Mn_3O_4 is a robust surface phase in the $Li_{1-x}[Mn_2]O_4$ system regardless of the chemical treatment and level of lithiation. The surface Mn_3O_4 phase is cubic whereas bulk Mn_3O_4 undergoes a cooperative Jahn-Teller distortion to tetragonal symmetry. Thicker Mn_3O_4 surface layers are tetragonal. $LiNi_{0.5}Mn_{1.5}O_4$ undergoes a surface reconstruction into a mixture of Mn_3O_4 and a Ni-rich rock-salt phase that is known to occur in the $LiNi_{0.5}Mn_{1.5}O_4$ system. Mn-rich LNM contains more Mn_3O_4 surface phases than LNM due to higher Mn content and lower surface Ni content. Annealing samples does not completely remove the surface rock-salt phase predicted to be eliminated by TGA. Cr-doped $LiNi_{0.5}Mn_{1.5}O_4$ undergoes a surface reconstruction into an ordered-spinel/rock-salt phase that has not been previously observed in either the $LiNi_{0.5}Mn_{1.5}O_4$ or $LiMn_2O_4$ systems. Cr doping suppresses the formation of Mn_3O_4 and segregates a Cr-containing rock-salt phase.

Appendix A: List of Publications Related to This Work

1. J. Song, D. W. Shin, Y. Lu, C. D. Amos, A. Manthiram, J. B. Goodenough. Role of Oxygen Vacancies on the Performance of $Li[Ni_{0.5-x}Mn_{1.5+x}]O_4$ (x = 0, 0.05, and 0.08) Spinel Cathodes for Lithium-Ion Batteries. Chemistry of Materials 24, 3101-3109 (2012).

2. C. D. Amos, M. A. Roldan, M. Varela, J. B. Goodenough, P. J. Ferreira. Revealing the Reconstructed Surface of $Li[Mn_2]O_4$. Nano Letters 16, 2899-2906 (2016).

References

[1] J. E. Post, "Manganese Oxide minerals: Crystal Structures and Economic and Environmental Significance," *Proceedings of the National Academy of Sciences*, Vol. 96, pp. 3447-3454 (1999).

[2] U.S. Pat. 2,960,558 (1957).

[3] M. M. Thackeray, W. I. F. David, P. G. Bruce, J. B. Goodenough, "Lithium Insertion into Manganese Spinels," *Materials Research Bulletin*, Vol. 18, Issue 4, pp. 461-472 (1983).

[4] J. M. Tarascon, E. Wang, F. K. Shokoohi, W. R. McKinnon, S. Colson, "The Spinel Phase of $LiMn_2O_4$ as a Cathode in Secondary Lithium Cells," *Journal of the Electrochemical Society*, Vol. 138, Issue 10, pp. 2859-2864 (1991).

[5] L. Guohua, H. Ikuta, T. Uchida, M. Wakihara, "The Spinel Phases $LiM_yMn_{2-y}O_4$ (M = Co, Cr, Ni) as the Cathode for Rechargeable Lithium Batteries," *Journal of the Electrochemical Society*, Vol. 143, Issue 1, pp. 178-182 (1996).

[6] C. Sigala, D. Guyomard, A. Verbaere, Y. Piffard, M. Tournoux, "Positive Electrode Materials with High Operating Voltage for Lithium Batteries: $LiCr_yMn_{2-y}O_4$ ($0 \leq y \leq 1$)," *Solid State Ionics*, Vol. 81, pp. 167-170 (1995).

[7] Q. Zhong, A. Bonakdarpour, M. Zhang, Y. Gao, J. R. Dahn, "Synthesis and Electrochemistry of $LiNi_xMn_{2-x}O_4$," *Journal of the Electrochemical Society*, Vol. 144, Issue 1, pp. 205-213 (1997).

[8] B. L. Cushing, V. L. Kolesnichenko, C. J. O'Connor, "Recent Advances in the Liquid-Phase Syntheses of Inorganic Nanoparticles," *Chemical Reviews*, Vol. 104, Issue 9, pp. 3893-3946 (2004).

[9] J. Livage, M. Henry, C. Sanchez, "Sol-Gel Chemistry of Transition Metal Oxides," *Progress in Solid State Chemistry*, Vol. 18, Issue 4, pp. 259-341 (1988).

[10] A. E. Danks, S. R. Hall, Z. Schnepp, "The Evolution of 'Sol-Gel' Chemistry as a Technique for Materials Synthesis," *Materials Horizons*, Vol. 3, 91-112 (2016).

[11] M. S. Whittingham, "Hydrothermal Synthesis of Transition Metal Oxides under Mild Conditions," *Current Opinion in Solid State and Materials Science*, Vol. 1, Issue 2, pp. 227-232 (1996).

[12] G. Demazeau, J. M. Millet, C. Cros, A. Largeteau, "Solvothermal Synthesis of Microcrystallites of Transition Metal Oxides," *Journal of Alloys and Compounds*, Vol. 262-263, pp. 271-274 (1997).

[13] U.S. Pat. 3,330,697 (1967).

[14] W. Liu, G. C. Farrington, F. Chaput, B. Dunn, "Synthesis and Electrochemical Studies of Spinel Phase $LiMn_2O_4$ Cathode Materials Prepared by the Pechini Process," *Journal of the Electrochemical Society*, Vol. 143, Issue 3, pp. 879-884 (1996).

[15] Y. Gao, J. R. Dahn, "Thermogravimetric Analysis to Determine the Lithium to Manganese Atomic Ratio in $Li_{1+x}Mn_{2-x}O_4$," *Applied Physics Letters*, Vol. 66, Issue 19, pp. 2487 (1995).

[16] J. C. Hunter, "Preparation of a New Crystal Form of Manganese Dioxide: λ-MnO_2," *Journal of Solid State Chemistry*, Vol. 39, Issue 2, pp. 142–147 (1981).

[17] J. Choi, E. Alvarez, T. A. Arunkumar, A. Manthiram, "Proton Insertion into Oxide Cathodes during Chemical Delithiation," *Electrochemical and Solid-State Letters*, Vol. 9, Issue 5, pp. A241–A244 (2006).

[18] P. D. Nellist, M. F. Chisholm, N. Dellby, O. L. Krivanek, M. F. Murfitt, Z. S. Szilagyi, A. R. Lupini, A. Borisevich, W. H. Sides Jr., S. J. Pennycook, "Direct Sub-Angstrom Imaging of a Crystal Lattice," *Science*, Vol. 305, Issue 5691, pp. 1741 (2004).

[19] E. Abe, "Electron Microscopy of Quasicrystals – *Where are the Atoms?*" *Chemical Society Reviews*, Vol. 41, pp. 6787–6798 (2012).

[20] K. Momma, F. Izumi, "VESTA: A Three-Dimensional Visualization System for Electronic and Structural Analysis," *Journal of Applied Crystallography*, Vol. 41, pp. 653-658 (2008).

[21] K. Ishizuka, "A Practical Approach for STEM Image Simulation Based on the FFT Multislice Method," *Ultramicroscopy*, Vol. 90, Issue 2-3, pp. 71-83 (2002).

[22] A. Weickenmeier, H. Kohl, "Computation of Absorptive Form Factors for High-Energy Electron Diffraction," *Acta Crystallographica*, Vol. A47, pp. 590-597 (1991).

[23] C. Dinges, A. Berger, H. Rose, "Simulation of TEM Images Considering Phonon and Electronic Excitations," *Ultramicroscopy*, Vol. 60, Issue 1, pp. 49-70 (1995).

[24] C. Dinges, H. Rose, "Simulation of Transmission and Scanning Transmission Electron Microscopic Images Considering Elastic and Thermal Diffuse Scattering," *Scanning Microscopy*, Vol. 11, pp. 277-286 (1997).

[25] D. J. Smith, M. R. McCartney, L. A. Bursill, "The Electron-Beam-Induced Reduction of Transition Metal Oxide Surfaces to Metallic Lower Oxides," *Ultramicroscopy*, Vol. 23, Issue 3-4, pp. 299-303 (1987).

[26] J. P. Buban, Q. Ramasse, B. Gipson, N. D. Browning, H. Stahlberg, "High-Resolution Low-Dose Scanning Transmission Electron Microscopy," Journal of Electron Microscopy, Vol. 59, Issue 2, pp. 103-112 (2010).

[27] C. Mitterbauer, G. Kothleitner, W. Grogger, H. Zandbergen, B. Freitag, P. Tiemeijer, F. Hofer, "Electron Energy-Loss Near-Edge Structures of 3d Transition Metal Oxides Recorded at High-Energy Resolution," *Ultramicroscopy*, Vol. 96, Issue 3-4, pp. 469-480 (2003).

[28] O. L. Krivanek, J. P. Ursin, N. J. Bacon, G. J. Corbin, N. Dellby, P. Hrncirik, M. F. Murfitt, C. S. Own, Z. S. Szilagyi, "High-Energy-Resolution Monochromator for Aberration-Corrected Scanning Transmission Electron Microscopy/Electron Energy-Loss Spectroscopy," *Philosophical Transactions of the Royal Society A*, Vol. 367, Issue 1903, pp. 3683-3697 (2009).

[29] R. S. Rai, S. Subramanian, "Role of Transmission Electron Microscopy in the Semiconductor Industry for Process Development and Failure Analysis," *Progress in Crystal Growth and Characterization of Materials*, Vol. 55, Issue 3-4, pp. 63-97 (2009).

[30] P. Trebbia, N. Bonnet, "EELS Elemental Mapping with Unconventional Methods I. Theoretical Basis: Image Analysis with Multivariate Statistics and Entropy Concepts," *Ultramicroscopy*, Vol. 34, Issue 3, pp. 165-178 (1990).

[31] N. Bonnet, D. Nuzillard, "Independent Component Analysis: A New Possibility for Analysing Series of Electron Energy Loss Spectra," *Ultramicroscopy*, Vol. 102, Issue 4, pp. 327–337 (2005).

[32] N. Dobigeon, N. Brun, "Spectral Mixture Analysis of EELS Spectrum-Images," *Ultramicroscopy*, Vol. 120, pp. 25-34 (2012).

[33] de la Peña, F., Ostasevicius, T., Fauske, V. T., Burdet, P., Jokubauskas, P., Nord, M., Prestat, E., Sarahan, M., MacArthur, K. E., Johnstone, D. N., Taillon, J., Caron, J., Furnival, T., Eljarrat, A., Mazzucco, S., Migunov, V., Aarholt, T., Walls, M., Winkler, F., Martineau, B., Donval, G., Hoglund, E. R., Alxneit, I., Hjorth, I., Zagonel, L. F.,

Garmannslund, A., Gohlke, C., Iyengar, I., Chang, H., (2017, May 27). hyperspy/hyperspy: HyperSpy 1.3. Zenodo. http://doi.org/10.5281/zenodo.583693

[34] M. M. Thackeray, P. J. Johnson, L. A. de Picciotto, P. G. Bruce, J. B. Goodenough, "Electrochemical Extraction of Lithium from $LiMn_2O_4$," *Materials Research Bulletin*, Vol. 19, Issue 2, pp. 179−187 (1984).

[35] J. Song, D. W. Shin, Y. Lu, C. D. Amos, A. Manthiram, J. B. Goodenough, "Role of Oxygen Vacancies on the Performance of $Li[Ni_{0.5-x}Mn_{1.5+x}O_4$ (x=0, 0.05, and 0.08) Spinel Cathodes for Lithium-Ion Batteries," *Chemistry of Materials*, Vol. 24, Issue 15, pp. 3101−3109 (2012).

[36] M. M. Thackeray, Manganese Oxides for Lithium Batteries," *Progress in Solid State Chemistry*, Vol. 25, Issue 1-2, pp. 1-71 (1997).

[37] H. Kurata, C. Colliex, "Electron-Energy-Loss Core-Edge Structures in Manganese Oxides*," Physical Review B: Condensed Matter and Materials Physics*, Vol. 48, Issue 4, pp. 2102-2108 (1993).

[38] R. Benedek, M. M. Thackeray, "Simulation of the Surface Structure of Lithium Manganese Oxide Spinel," *Physical Review B: Condensed Matter and Materials Physics*, Vol. 83. Issue 19, pp. 195439 (2011).

[39] M. N. Richard, E. W. Fuller, J. R. Dahn, "The Effect of Ammonia Reduction on the Spinel Electrode Materials, $LiMn_2O_4$ and $Li(Li_{13}Mn_{53})O_4$," *Solid State Ionics*, Vol. 73, Issue 1-2, pp. 81-91 (1994).

[40] M. Gu, I. Belharouak, J. Zheng, H. Wu, J. Xiao, A. Genc, K. Amine, S. Thevuthasan, D. R. Baer, J. Zhang, N. D. Browning, J. Liu, C. Wang, "Formation of the Spinel Phase in the Layered Composite Cathode Used in Li-Ion Batteries," *ACS Nano*, Vol. 7, Issue 1, pp. 760−767 (2013).

[41] P. Yan, A. Nie, J. Zheng, Y. Zhou, D. Lu, X. Zhang, R. Xu, I. Belharouak, X. Zu, J. Xiao, K. Amine, J. Liu, F. Gao, R. Shahbazian-Yassar, J. Zhang, C. Wang, "Evolution of Lattice Structure and Chemical Composition of the Surface Reconstruction Layer in $Li_{1.2}Ni_{0.2}Mn_{0.6}O_2$ Cathode Material for Lithium Ion Batteries," *Nano Letters*, Vol. 15, Issue 1, pp. 514-522 (2015).

[42] D. Tang, Y. Sun, Z. Yang, L. Ben, L. Gu, X. Huang, "Surface Structure Evolution of $LiMn_2O_4$ Cathode Material upon Charge/Discharge," *Chemistry of Materials*, Vol. 26, Issue 11, pp. 3535−3543 (2014).

[43] D. Tang, L. Ben, Y. Sun, B. Chen, Z. Yang, L. Gu, X. Huang, "Electrochemical Behavior and Surface Structural Change of $LiMn_2O_4$ Charged to 5.1 V," *Journal of Materials Chemistry A*, Vol. 2, pp. 14519−14527 (2014).

[44] Y. Xia, Y. Zhou, M. Yoshio, "Capacity Fading on Cycling of 4 V Li/$LiMn_2O_4$ Cells," *Journal of the Electrochemical Society*, Vol. 144, Issue 8, pp. 2593-2600 (1997).

[45] D. H. Jang, Y. J. Shin, S. M. Oh, "Dissolution of Spinel Oxides and Capacity Losses in 4 V Li/$Li_xMn_2O_4$ Cells," *Journal of the Electrochemical Society*, Vol. 143, Issue 7, 2204-2211 (1996).

[46] S. Kim, M. Aykol, C. Wolverton, "Surface Phase Diagram and Stability of (001) and (111) $LiMn_2O_4$ Spinel Oxides," *Physical Review B: Condensed Matter and Materials Physics*, Vol. 92, Issue 11, pp. 115411 (2015).

[47] A. Karim, S. Fosse, K. A. Persson, "Surface Structure and Equilibrium Particle Shape of the $LiMn_2O_4$ Spinel from First-Principles Calculations," *Physical Review B: Condensed Matter and Materials Physics*, Vol. 87, Issue 7, pp. 075322 (2013).

[48] C. D. Amos, M. A. Roldan, M. Varela, J. B. Goodenough, P. J. Ferreira, "Revealing the Reconstructed Surface of $Li[Mn_2]O_4$," *Nano Letters*, Vol. 16, Issue 5, pp. 2899-2906 (2016).

[49] J. R. Ligenza, "Silicon Oxidation in an Oxygen Plasma Excited by Microwaves," *Journal of Applied Physics*, Vol. 36, Issue 9, pp. 2703-2707 (1965).

[50] S. Kimura, E. Murakami, K. Miyake, T. Warabisako, H. Sunami, T. Tokuyama, "Low Temperature Oxidation of Silicon in a Microwave-Discharged Oxygen Plasma," *Journal of the Electrochemical Society*, Vol. 132, Issue 6, pp. 1460-1466 (1985).

[51] C. C. Chen, K. Chiu, K. M. Lin, H. C. Lin, C. Yang, F. M. Wang, "Improved Electrochemical Performances of Oxygen Plasma Treated $LiMn_2O_4$ Thin Films," *Physica Scripta*, Vol. 74, pp. T129 (2007).

[52] H. F. McMurdie, E. Golovato, "Study of the Modifications of Manganese Dioxide," *Journal of Research of the National Bureau of Standards*, Vol. 41, pp. 589-600 (1948).

[53] O. Y. Gorbenko, I. E. Graboy, V. A. Amelichev, A. A. Bosak, A. R. Kaul, B. Guttler, V. L. Svetchnikov, H. W. Zandbergen, "The Structure and Properties of Mn_3O_4 Thin Films Grown by MOCVD," *Solid State Communications*, Vol. 124, Issue 1-2, pp. 15-20 (2002).

[54] J. B. Goodenough, Y. Kim, "Challenges for Rechargeable Li Batteries," *Chemistry of Materials*, Vol. 22, Issue 3, pp. 587-603 (2010).

[55] K. R. Chemelewski, E. Lee, W. Li, A. Manthiram, "Factors Influencing the Electrochemical Properties of High-Voltage Spinel Cathodes: Relative Impact of Morphology and Cation Ordering," *Chemistry of Materials*, Vol. 25, Issue 14, pp. 2890-2897 (2013).

[56] D. W. Shin, A. Manthiram, "Surface-Segregated, High-Voltage Spinel $LiMn_{1.5}Ni_{0.42}Ga_{0.08}O_4$ Cathodes with Superior High-Temperature Cyclability for Lithium-ion Batteries," *Electrochemistry Communications*, Vol. 13, Issue 11, pp. 1213-1216 (2011).

[57] G. B. Zhong, Y. Y. Wang, Z. C. Zhang, C. H. Chen, "Effects of Al Substitution for Ni and Mn on the Electrochemical Properties of $LiNi_{0.5}Mn_{1.5}O_4$," *Electrochimica Acta*, Vol. 56, Issue 18, pp. 6554-6561 (2011).

[58] D. W. Shin, C. A. Bridges, A. Huq, M. P. Paranthaman, A. Manthiram, "Role of Cation Ordering and Surface Segregation in High-Voltage Spinel $LiMn_{1.5}Ni_{0.5-x}M_xO_4$ (M=Cr, Fe, and Ga) Cathodes for Lithium-Ion Batteries," *Chemistry of Materials*, Vol. 24, Issue 19, pp. 3720-3731 (2012).